



«The Paton Welding Journal» is a journal for a wide range of experts from around the world in the field of welding and related technologies.

**EDITORIAL BOARD**

E.O. Paton Electric Welding Institute, Kyiv, Ukraine:

**I.V. Krivtsun** (*Editor-in-Chief*),**S.V. Akhonin** (*Deputy Editor-in-Chief*),**L.M. Lobanov** (*Deputy Editor-in-Chief*),**O.M. Berdnikova**, **V.V. Knysh**, **V.M. Korzhyk**,**Yu.M. Lankin**, **S.Yu. Maksimov**, **M.O. Pashchin**,**V.D. Poznyakov**, **I.O. Ryabtsev**;**V.V. Dmitrik**, NTUU

«Kharkiv Polytechnic Institute», Kharkiv, Ukraine;

**V.V. Kvasnitsky**, NTUU

«Igor Sikorsky Kyiv Polytechnic Institute»,

Kyiv, Ukraine;

**V.M. Uchanin**, Karpenko physico-mechanical institute,

Lviv, Ukraine;

**A. Gumenyuk**, Bundesanstalt für Materialforschung

und –prüfung (BAM), Berlin, Germany;

**U. Reisgen**, Welding and Joining Institute,

Aachen, Germany

**Founders**

E.O. Paton Electric Welding Institute

International Association «Welding»

**Publisher**

International Association «Welding»

*Translator*: A.O. Fomin*Editor*: N.G. Khomenko*Electron galley*: D.I. Sereda, T.Yu. Snegiryova**Address**

E.O. Paton Electric Welding Institute,

International Association «Welding»

11 Kazymyr Malevykh Str. (former Bozhenko),

03150, Kyiv, Ukraine

Tel./Fax: (38044) 200 82 77

E-mail: journal@paton.kiev.ua

www://patonpublishinghouse.com/eng/journals/tpwj

State Registration Certificate

KV 4790 of 09.01.2001

ISSN 0957-798X

DOI: <http://dx.doi.org/10.37434/tpwj>**Subscriptions**

12 issues per year, back issues available.

\$384, subscriptions for the printed (hard copy) version, air postage and packaging included.

\$312, subscriptions for the electronic version (sending issues of Journal in pdf format or providing access to IP addresses).

Institutions with current subscriptions on printed version can purchase online access to the electronic versions of any back issues that they have not subscribed to.

Issues of the Journal (more than two years old) are available at a substantially reduced price.

All rights reserved.

This publication and each of the articles contained herein are protected by copyright.

Permission to reproduce material contained in this journal must be obtained in writing from the Publisher.

© E.O. Paton Electric Welding Institute of NASU, International Association «Welding», 2021

**CONTENTS****METALLURGY AND TECHNOLOGY OF WELDING AND SURFACING**

- Knysh V.V., Solovej S.O., Ryabtsev I.O. and Babinets A.A.* Fatigue life of specimens from 40Kh steel after wear-resistant surfacing with a low-alloy steel sublayer ..... 2
- Leshchynskyi L.K., Ivanov V.P., Matviienko V.M., Stepanov K.K. and Vozyanov E.I.* Development of technology for surfacing working layer of variable composition on crimping rolls ..... 8
- Stefaniv B.V.* Development of technology of manufacture of drill bits with protective coating of working bodies ..... 11

**BRAZING PROCESSES**

- Maksymova S.V., Zvolinskyy I.V. and Ivanchenko E.V.* Influence of alloying elements on solidus and liquidus temperatures of alloys of Cu–Mn–Ni–Si system ..... 17

**3D PRINTING**

- Senchenkov I.K., Iurzhenko M.V., Chervinko O.P., Masiuchok O.P. and Korab M.G.* Numerical modeling of stress-strain state of elements manufactured by 3D printing ..... 21

**SOLID PHASE WELDING**

- Kuchuk-Yatsenko S.I., Hushchyn K.V., Ziakhor I.V., Samotryasov S.M., Zavertannyi M.S. and Levchuk A.M.* Structure and mechanical properties of 2219-T87 aluminium alloy joints produced by flash butt welding ..... 27

**WELDING CONSUMABLES**

- Kostin O.M., Yaros O.O., Yaros Y.O. and Savenko O.V.* UPE-500 complex for determining welding and technological characteristics of coated electrodes ..... 33

**ELECTRON BEAM PROCESSES**

- Akhonin S.V., Berezos V.O., Bondar O.I., Glukhenkyi O.I., Goryslavets Yu.M. and Severin A.Yu.* Mathematical modeling of hydrodynamic and thermal processes at crystallization of titanium ingots produced by EBM ..... 38

**NONDESTRUCTIVE TESTING**

- Uchanin V.M., Ostash O.P., Bychkov S.A., Semenets O.I. and Derecha V.Ya.* Eddy current monitoring of aluminium alloy degradation during long-term operation of aircraft ..... 45

The content of the journal includes articles received from authors from around the world and selectively includes translations into English of articles from the following journals, published by PWI in Ukrainian:

- Automatic Welding (<https://patonpublishinghouse.com/eng/journals/as>);
- Technical Diagnostics & Nondestructive Testing (<https://patonpublishinghouse.com/eng/journals/tdnk>);
- Electrometallurgy Today (<https://patonpublishinghouse.com/eng/journals/sem>).

## FATIGUE LIFE OF SPECIMENS FROM 40Kh STEEL AFTER WEAR-RESISTANT SURFACING WITH A LOW-ALLOY STEEL SUBLAYER

V.V. Knysh, S.O. Solovej, I.O. Ryabtsev and A.A. Babinets

E.O. Paton Electric Welding Institute of the NAS of Ukraine

11 Kazymyr Malevych Str., 03150, Kyiv, Ukraine. E-mail: [office@paton.kiev.ua](mailto:office@paton.kiev.ua)

Studied was the resistance of a multilayer material to fatigue fracture, in which wear-resistant layer was deposited with the PP-Np-25Kh5FMS flux-cored wire with a sublayer from a low-alloy material, deposited with the PP-Np-12Kh1MF wire. The design of surfaced specimens and their test procedure simulated the operating conditions of steel mill rolls. The integrated procedure of evaluation of fatigue fracture resistance of multilayer surfaced specimens to included three stages: determination of cyclic fatigue life of specimens after fabrication surfacing; studying the cyclic crack resistance of different deposited layers; determination of fatigue life of specimens, having fatigue cracks in the deposited layer during previous testing, after their repair surfacing. It was found that the cyclic fatigue life of specimens from 40Kh carbon steel, deposited with the PP-Np-25Kh5FMS flux-cored wire with a sublayer of 12Kh1MF low-alloy steel is in the range of 346–716 thou cycles at maximum stress level of 500 MPa. Features of fatigue fracture kinetics of the studied multilayer material were determined. It was established that the fatigue crack propagates in the deposited metal in an unstable manner (in the wear-resistant layer and in a low-alloy steel sublayer), constantly changing its rate and direction. It is shown that cutting out fatigue cracks and subsequent surfacing of their removal areas allows restoring the cyclic fatigue life of the specimen to the initial level, i.e. twice increasing the overall life. 16 Ref., 4 Tables, 7 Figures.

*Key words:* arc surfacing, repair surfacing, sublayer, fatigue life, fatigue cracks, stress intensity factor

It is widely known that in metallurgical and machine-building industries, a large number of parts and tools are operated in the conditions of cyclic mechanical loads [1]. Such complex operating conditions lead, in particular, to the appearance of fatigue cracks on the surface of parts, which, on the example of mill rolls, can lead to a rejection of metal-rolling products, failure of equipment and, as a consequence, significant material losses [1–6].

In order to increase the life of such parts, produced of medium-carbon steel of type 35KhM, 45, 50, 40Kh, 50Kh, etc., a production or repair-restoration surfacing of external wear-resistant layer of metal are often used. Most often, for this purpose electrode materials are used that provide a deposited metal of type of medium- or high-alloy semi-heat-resistant or heat-resistant tool steels 25Kh5FMS, 30Kh4V2M2FS, 35V9Kh3SF, etc. [7, 8].

It is widely known that to improve weldability of the base and deposited metal, especially if they relate to dissimilar classes of metals, surfacing of the intermediate ductile layer of metal (sublayer) is used. Also, with the use of a substrate material with an intermediate value of the temperature expansion coefficient, residual surfacing stresses can be slightly reduced, which can positively affect the overall fatigue life of

a deposited specimen or part [7, 8]. From practical experience it is known that as a sublayer materials low-carbon, low-alloyed materials are used, that provide a ductile metal of type of steels 08kp(rimmed), 08G2S, etc. [8].

Therefore, in [9], it was shown that the use of ductile metal of type 08kp as a sublayer provided a 1.4 times increase in the fatigue life of experimental specimens at a cyclic mechanical load as compared to similar specimens without a sublayer. In the works [10, 11], as a result of an integrated evaluation of fatigue life of specimens with the same sublayer material, but deposited by another technology, it was found that during production surfacing using the wire Sv-08A on a steel 40Kh with a subsequent surfacing of a wear-resistant and heat-resistant layer of steel of type 25Kh5FMS, fatigue life of the specimens is 2 times higher as compared to the specimens, deposited without a sublayer.

The aim of the work is an experimental comparative study of the influence of low-alloy metal sublayer on the fatigue life of a multilayer material in the production and repair (restorative) wear-resistant surfacing.

**Procedures, technologies and research materials.** In order to compare the influence of the sublayer material on the fatigue life of the deposited speci-

V.V. Knysh — <https://orsid.org/0000-0003-1289-4462>, S.O. Solovej — <https://orsid.org/0000-0002-1126-5536>,

I.O. Ryabtsev — <https://orsid.org/0000-0001-7180-7782>, A. Babinets — <https://orsid.org/0000-0003-4432-8879>

**Table 1.** Mechanical properties of base and deposited metals

Grade of material	Mechanical properties (after normalization)					
	Conventional yield strength $\sigma_{0.2}$ , MPa	Tensile strength $\sigma_t$ , MPa	Relative elongation $\delta$ , %	Reduction in area $\psi$ , %	Impact toughness $KCU$ , J/cm <sup>2</sup>	Hardness $HB$
40Kh	345	590	12.5	52	7.5	174–217
08kp*	196	320	33	60	–	≤131
12Kh1MF	255	470	21	55	98	≤217
4Kh5MFS*	1570	1710	12	54	51	444–478

\*In the literature there are no data on mechanical properties of the metal, deposited by the wires Sv-08A and PP-Np-25Kh5FMS. Therefore, the data for their analogues (the most close as to chemical composition and mechanical properties), respectively, steels 08kp and 4Kh5MFS are given.

**Table 2.** Chemical composition of base and deposited metals [12]

Grade of material	Mass fraction of elements, %							
	C	Mn	Si	Cr	V	Mo	S	P
40Kh	0.36–0.40	0.5–0.8	0.17–0.37	0.8–1.1	–	–	≤0.035	≤0.035
Sv-08A**	0.05–0.12	0.2–0.4	0.1–0.3	–	–	–	≤0.04	≤0.04
08kp	0.05–0.12	0.25–0.5	≤0.3	≤0.10	–	–	≤0.035	≤0.04
12Kh1MF	0.10–0.15	0.4–0.7	0.17–0.37	0.9–1.2	0.15–0.3	0.25–0.35	≤0.025	≤0.035
PP-Np-25Kh5FMS**	0.20–0.32	0.5–1.0	0.80–1.30	4.6–5.8	0.2–0.6	0.9–1.5	≤0.04	≤0.04
4Kh5MFS**	0.32–0.40	0.2–0.5	0.90–1.20	4.5–5.5	0.3–0.5	1.2–1.5	≤0.04	≤0.04

\*\*Mass fraction of elements in the deposited metal is given.

mens, in this work, a sublayer of a low-alloy steel of type 12Kh1MF was used. The steel of this grade was chosen based on its higher mechanical properties as compared to steel 08kp (Table 1).

In order to establish the rationality of using low-alloy steel sublayers with the aim of increasing the fatigue life of multilayer deposited specimens, the previously developed surfacing technology was used, described in detail in [10, 11]. In order to obtain reliable results of studies of the steel grade of the base metal and a deposited wear-resistant metal layer (steel 40Kh and 25Kh5FMS, respectively) during surfacing without a sublayer and with a sublayer of different types were the same. For surfacing of the intermediate layer, an experimental flux-cored wire of grade PP-Np-12Kh1MF of 1.8 mm diameter was used. The chemical composition and mechanical properties of materials used in the work are given in Tables 1, 2 [12].

The studies were performed in three stages and for each one 3–5 prismatic specimens with the sizes of 350×40×20 mm were manufactured, which subsequently were tested using a developed integrated procedure for evaluating the resistance of a multilayer material to fatigue fracture [10, 11]. This procedure includes the following stages: establishment of cyclic life of specimens after a fabrication surfacing; study of cyclic crack resistance of different layers of metal; determination of fatigue life of specimens, which had fatigue cracks in a deposited layer in the process of preliminary tests and after repair surfacing. In more

details, surfacing modes and technologies, as well as research procedures are described in [10, 11].

### Results of experiments and their discussion.

*Specimens of the first series.* Initially, three specimens of the first series of carbon steel 40Kh, deposited using the flux-cored wire PP-Np-25Kh5FMS with a low-alloy steel 12Kh1MF were tested at the levels of maximum stresses of 600 MPa, characteristic of specimens manufactured with low-carbon steel sublayers [11]. Due to the presence of inner defects in the deposited layer, it was failed to obtain reliable results of fatigue life. Therefore additional specimens were manufactured and it was decided to perform tests at the levels of maximum stresses of 500 MPa, characteristic to the specimens produced without a sublayer [10]. The results of studies of fatigue life of specimens, deposited by the wire PP-Np-25Kh5FMS with a sublayer of low-alloy steel 12Kh1MF, are shown in Table 3.

During fatigue tests of the first series of specimens, deposited with the wire PP-Np-25Kh5FMS with a low-alloy steel substrate, it was found that their cyclic life before fracture at maximum applied stresses of 500 MPa is in the range of 346000–716800 cycles.

It should be noted that fracture of the specimens without a sublayer at the levels of maximum stresses of 500 MPa occurred in the range from 560800 to 1420100 cycles of stress changes [10], and the specimens with low-carbon steel sublayers withstood more than 20000000 cycles of stress changes [11].

On the specimens of the second series from a sharp notch in the wear-resistant layer of metal, an initial crack

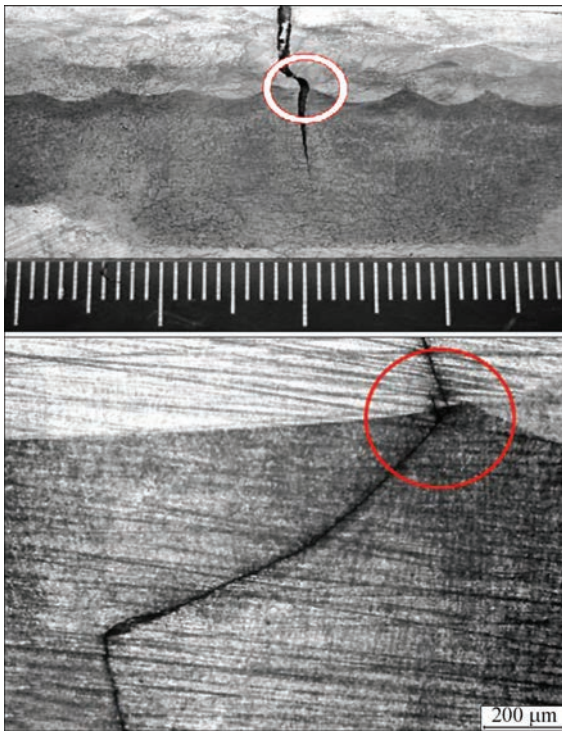


**Figure 1.** Nature of fatigue crack propagation in the specimens of 40Kh steel, deposited with the wire PP-Np-25Kh5FMS with a sublayer of a low-alloy 12Kh1MF steel

with a depth of 1 mm at the levels of maximum stresses of 400 MPa was grown. During further tests of the specimen at the levels of maximum stresses of 400 MPa, the length of the fatigue crack and the corresponding number of variable load cycles  $N$  were recorded.

Experimental studies of the features of fatigue crack propagation in these specimens were confirmed by the previously obtained data that the fusion zone of individual beads and layers plays an important role in the process of fatigue fracture of deposited parts, because the cracks are mostly propagating either on the fusion boundary of the individual beads, or close to this boundary (Figure 1).

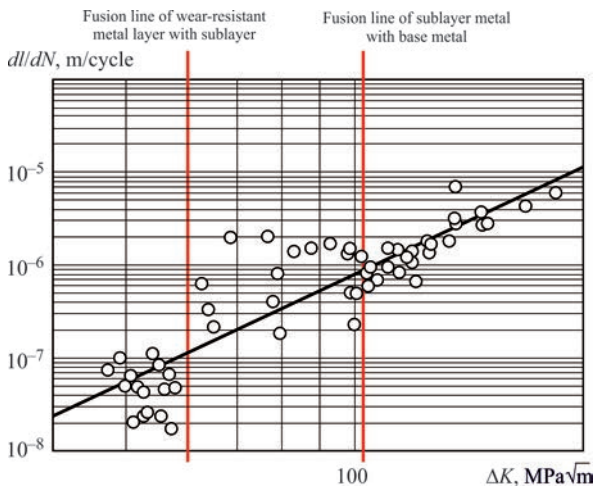


**Figure 2.** Kinetic diagram of fatigue fracture of multilayer material formed by wear resistant surfacing with the use of a sublayer of a low-alloy steel

**Table 3.** Results of fatigue tests of specimens of the first series

Number of specimen	Maximum cycle stresses, MPa	Cyclic life before fracture, cycles
1	600	18.000*
2	Same	72.400*
3	»	261.000
4	500	716.800
5	Same	381.800
6	»	528.700
7	»	346.000

\*In the specimens defects were found formed during surfacing.

To construct kinetic diagrams of fatigue fracture (KDFE), the calculation of values of the stress intensity factor (CIF) for a prismatic specimen with a transverse edge crack at a three-point bending was made according to the expressions given in [13]. Experimental dependence of the growth rate of the fatigue crack from the range of CIF in different layers of the multilayer specimen metal is presented as a corresponding KDFE obtained by the results of testing three specimens (Figure 2). Separately, Figure 3 shows a kinetic diagram of the fatigue fracture of the base metal of 40Kh steel.

In a deposited metal (in a wear-resistant layer and in a low-alloy steel sublayer), a fatigue crack propagates in an unstable way. Therefore, in the range of CIF being 45–60 MPa√m, when a crack propagated in the metal of a wear-resistant layer, its rate constantly changed in the range of values  $10^{-8}$ – $10^{-7}$  m/cycle. At a further propagation in the metal of the sublayer, the growth rate of the fatigue crack increases by an order to  $2 \cdot 10^{-7}$ – $2 \cdot 10^{-6}$  m/cycle in the range of CIF being 60–100 MPa√m. In the base metal, a crack was steadily propagated at an ever-increasing rate from  $6 \cdot 10^{-7}$  to  $7 \cdot 10^{-6}$  m/cycle until fracture of the specimen at the values of CIF being 160–180 MPa√m, which corresponds to the established KDFE of 40Kh steel.

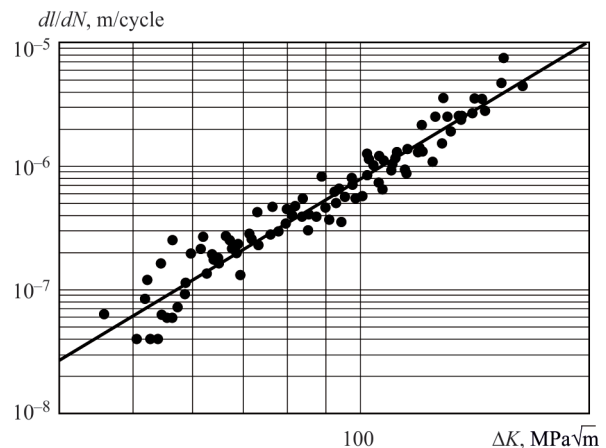


**Figure 3.** Kinetic diagram of fatigue fracture of base metal of 40Kh steel

On the specimens of the third series, the initiation and propagation of fatigue cracks from possible defects in a deposited wear-resistant layer of metal was originally modeled. Therefore, the specimens were tested at a cyclic load to till formation of fatigue cracks at a depth of 10–12 mm, which subsequently were subjected to elimination by repair surfacing. After performing repair surfacing, measurements of residual stresses by nondestructive ultrasonic method were carried out [14]. This method does not allow measuring residual stresses in the cast metal, so the measurement of residual stresses oriented along and across the specimen was carried out at a distance from the low-carbon fusion line with the base metal (determined by the macrostructure) deep into the metal. The values of residual stresses, given on the diagrams are averaged over the thickness of the specimen. The schematic representation of the measurement places of residual stresses is shown in Figure 4, and the diagrams of distribution of residual stresses in the initial state and after repair surfacing are in Figures 5, 6.

Data of measurements of residual stresses in the specimen of 40Kh steel with a surfacing of a wear-resistant layer with a sublayer of 12Kh1MF steel given in Figure 5, show that the maximum tensile stresses  $\sigma_x$ , which are oriented along the specimen (coincided

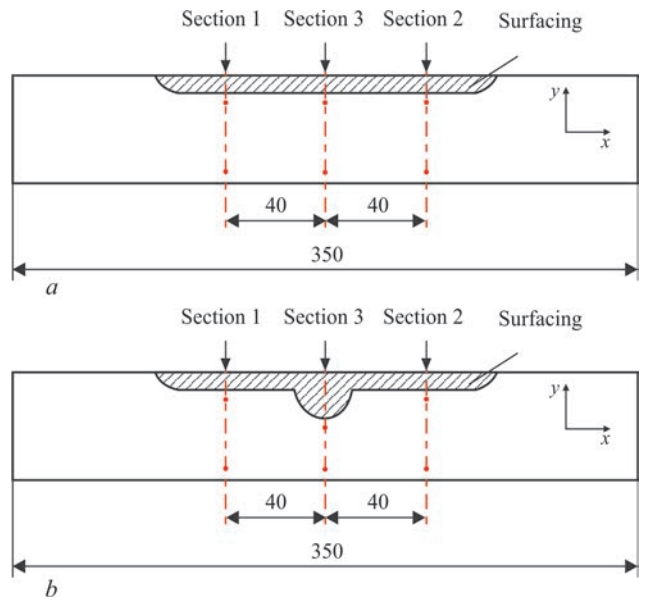


**Figure 4.** Schematic representation of places of measurement of residual stresses in the specimen before (a) and after (b) repair surfacing

by the direction with applied working stresses during fatigue tests of specimens) are by 20 % higher as compared to the maximum levels of tensile stresses  $\sigma_y$ , formed in a multilayer material with a sublayer of steel 08kp [11].

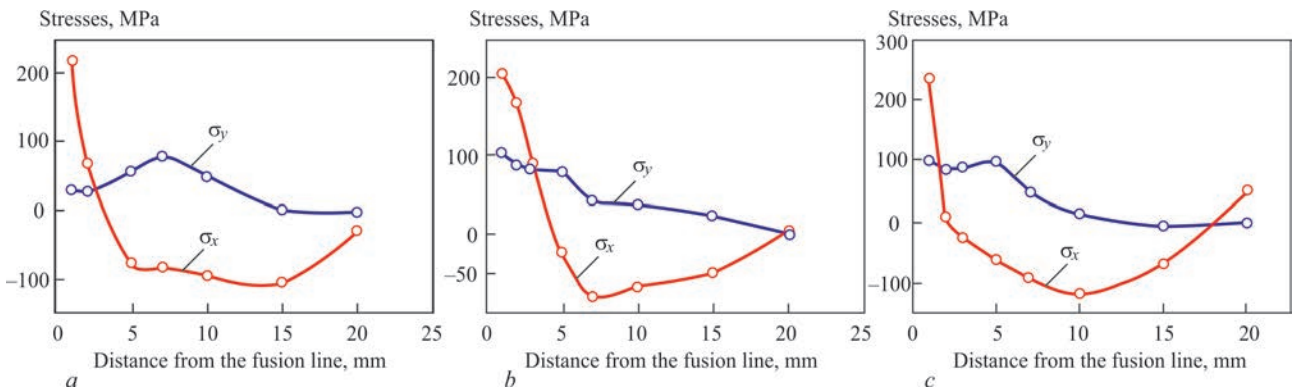


**Figure 5.** Distribution of residual stresses, oriented along  $\sigma_x$  and across  $\sigma_y$  of the specimen before repair surfacing, in the section 1 (a), section 2 (b) and section 3 (c) according to Figure 4, a

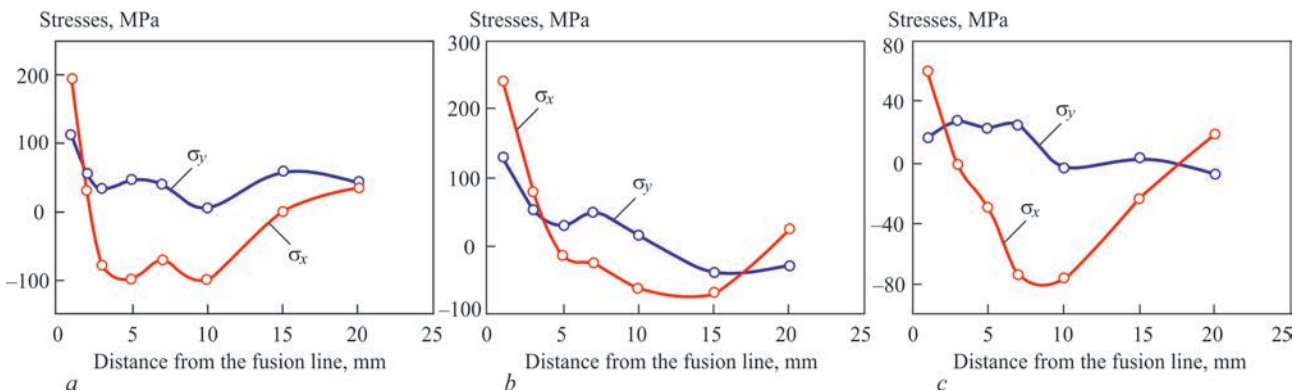


**Figure 6.** Distribution of residual stresses, oriented along  $\sigma_x$  and across  $\sigma_y$  of the specimen before repair surfacing, in the section 1 (a), 2 (b) and 3 (c) according to Figure 4, b

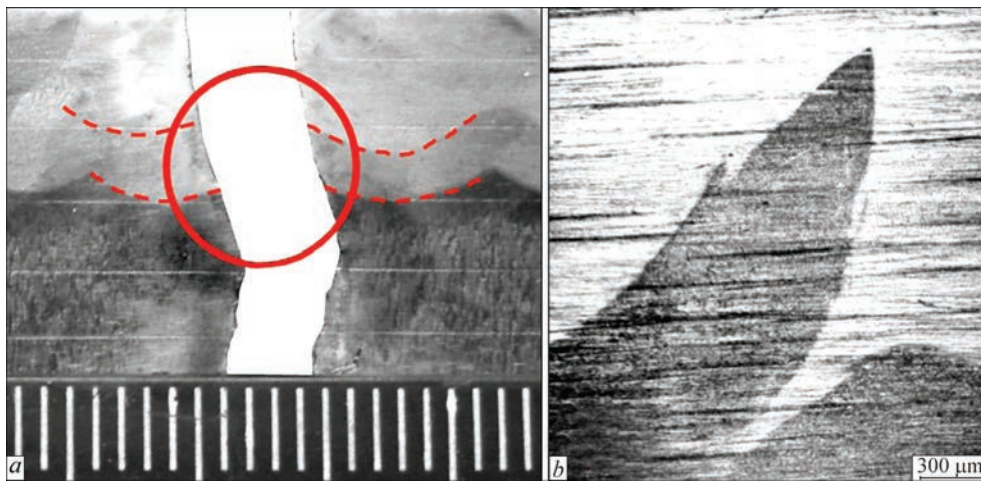


**Figure 7.** Appearance of the specimen area after repair surfacing with a fatigue crack, that passes on the boundary between the adjacent deposited beads (a) and the zone of macroheterogeneity — the boundary between the «old» deposited metal, and the metal, deposited in the course of repair (b)

After repair surfacing, the maximum of specimen residual tensile stresses  $\sigma_x$ , in intersections 1 and 2 are almost remained unchanged, while in the intersection 3 they significantly decrease to 60 MPa (Figure 6).

After measurements of residual stresses, the specimens of the third series were tested on fatigue at a three-point zero-to-tension cyclic bending. Cyclic life of specimens before and after repair surfacing is given in Table 4. Moreover, it should be noted that all the specimens after repair during fatigue tests were fractured at more than 20 mm from the cross-section 3, i.e., in the places with higher residual tensile stresses  $\sigma_x$ .

After performing repair surfacing, as in the case of fabrication surfacing, the initiation and propagation of fatigue cracks in all the specimens of the third series occurred either on the fusion boundary of individual beads, or directly near this boundary, obviously, as a result of chemical and structural heterogeneity in the mentioned area (Figure 7, a.). Summary, the specimens deposited with a low-alloy steel sublayer, after a premature wear until the initiation of a crack, repair surfacing and the next cyclic load withstood in average about ~ 600 thou cycles. Therefore, the life of specimens after production and repair surfacing is approximately the same and amounts to ~ 300 thou cycles.

A particular attention should be paid also to the technology of repair surfacing, because while performing preparation in accordance with the parameters determined previously and during its subsequent

filling, the unfavorable zones of macroheterogeneity may be formed on the boundary between the new and «old» deposited metal (Figure 7, b), which also can influence the fatigue life of a specimen.

**Generalization of results.** Comparison of the data obtained for the specimens of 40Kh steel, deposited without a sublayer [10], with sublayers of a low-carbon steel 08kp [11] and a low-alloy 12Kh1MF steel, indicates that the specimens, deposited with a sublayer with a more ductile low-carbon steel 08kp, have the longest life both before as well as after repair surfacing. This can be explained by several factors. First, this is associated with a higher ultimate and yield strength of 12Kh1MF steel as compared to steel 08kp and, at the same time, a lower relative elongation (see Table 1), which led to the formation of higher levels of residual tensile stresses in the deposited metal (see Figures 5, 6). Secondly, the reason for the negative impact on the fatigue life of 12Kh1MF material may be chemical or structural heterogeneities, formed in the transition zones base–sublayer–working layer [5, 15, 16].

It is obvious that during repair surfacing, when only a metal area around the fatigue crack is removed, the difficulties in providing a uniform chemical and macrostructural state are added as a result of violation of the initial order of deposition and the structure of deposited beads. In addition, in multilayer surfacing with the use of medium- and high-carbon electrode materials, because of the repeated heatings, in the zones of adjacent beads overlapping, an additional formation of carbides may occur, which depletes the surrounding matrix and leads to the formation of chemical and structural heterogeneity. These areas may become the sources of crack initiation in the conditions of mechanical cyclic load, and therefore, the abovementioned factors need to be taken into account when developing techniques and technology of both production and especially repair surfacing.

**Table 4.** Results of fatigue tests of specimens of the third series

Number of specimen	Maximum cycle stresses, MPa	Cyclic life before the initiation of a 10–12 mm crack, cycles	Cyclic life after repair surfacing, cycles	Total cyclic life, cycles
11	500	285600	256400	542000
12	500	333300	144900	478200
13	500	283100	448200	731300

## Conclusions

1. The technology of production and repair surfacing of specimens from carbon 40Kh steel were developed, which are deposited by the flux-cored wire PP-Np-25Kh5FMS with a sublayer of a low-alloy 12Kh1MF steel. It was found by nondestructive ultrasonic method of stress measurements, that the maximum longitudinal residual tensile stresses reach the values of 220–240 MPa. After performing the repair surfacing, the maximum residual tensile stresses  $\sigma_x$  are decreased to 60 MPa. At the same time in other sections of the specimen, the levels of residual tensile stresses remain almost unchanged.

2. In the deposited metal (in a wear-resistant layer and in a low-alloy steel sublayer), a fatigue crack propagates unstable. Thus, in the range of CIF being 45–60 MPa $\sqrt{m}$ , when a crack propagated in the metal of a wear-resistant layer, its rate constantly changed in the range of  $10^{-8}$ – $10^{-7}$  m/cycle. With the further propagation in the metal of the sublayer, the growth rate of a fatigue crack rises by an order to  $2 \cdot 10^{-7}$ – $2 \cdot 10^{-6}$  m/cycle in the range of CIF being 60–100 MPa $\sqrt{m}$ . In the base metal, a crack steadily propagated with an ever-increasing rate of  $6 \cdot 10^{-7}$  to  $7 \cdot 10^{-6}$  m/cycle until the fracture of the specimen at the values of CIF being 160–180 MPa $\sqrt{m}$ , which corresponds to the established KDFF of 40Kh steel.

3. It was found that the cyclic life of the specimens from carbon 40Kh steel, deposited with a flux-cored wire PP-Np-25Kh5FMS with a low-alloy 12Kh1MF steel sublayer is 2–3 times lower than the cyclic life of the specimens, deposited without a sublayer. Thus, the cyclic life of the specimens without a sublayer at the levels of maximum stresses of 500 MPa, is in the range of 561–1420 thou cycles of stress changes, and the cyclic life of defect-free specimens with a sublayer of 12Kh1MF is 346–716 thou cycles.

4. It is shown that realization of repair surfacing according to the scheme of removal and a subsequent surfacing of only areas of metal with fatigue cracks allow restoring cyclic life to the level of the initial state, i.e., increase the overall life twice. In this case, the fracture of restored specimens occurred far from the place of repair surfacing.

1. Du Toit, M., Van Niekerk, J. (2010) Improving the life of continuous casting rolls through submerged arc cladding with

- nitrogen-alloyed martensitic stainless steel. *Welding in the World*, 54(11–12), 342–349. DOI:10.1007/bf03266748
2. Jhavar, S., Paul, C.P., Jain, N.K. (2013) Causes of failure and repairing options for dies and molds: A Review. *Engineering Failure Analysis*, 34, 519–535. DOI: <https://doi.org/10.1016/j.engfailanal.2013.09.006>
3. Ahn, D.-G. (2013) Hardfacing technologies for improvement of wear characteristics of hot working tools: A Review. *Int. J. of Precision Engineering and Manufacturing*, 14(7), 1271–1283. DOI:10.1007/s12541-013-0174-z
4. Zhang, J., Zhou, J., Tao, Y. et al. (2015) The microstructure and properties change of dies manufactured by bimetal-gradient-layer surfacing technology. *The Int. J. Adv. Manuf. Technol.*, 80, 1807–1814 (2015). DOI: <https://doi.org/10.1007/s00170-015-7170-7>
5. Gao, F., Zhou, J., Zhou, J. et al. (2017) Microstructure and properties of surfacing layers of dies manufactured by bimetal-gradient-layer surfacing technology before and after service. *The Int. J. Adv. Manuf. Technol.*, 88, 1289–1297. DOI: <https://doi.org/10.1007/s00170-016-8679-0>
6. Vundru, C., Paul, S., Singh, R., Yan, W. (2018) Numerical analysis of multi-layered laser cladding for die repair applications to determine residual stresses and hardness. *Procedia Manufacturing*, 26, 952–961. DOI: <https://doi.org/10.1016/j.promfg.2018.07.122>
7. Ryabtsev, I.A., Senchenkov, I.K. (2013) *Theory and practice of surfacing works*. Kiev, Ekotekhnologiya [in Russian].
8. Rjabcev, I.A., Senchenkov, I.K., Turyk, Je.V. (2015) *Surfacing. Materials, technologies, mathematical modeling*. Gliwice, Wydawnictwo politechniki slaskiej [in Russian].
9. Babinets, A.A., Ryabtsev, I.A. (2016) Fatigue life of multilayer hard-faced specimens. *Welding Int.*, 30(4), 305–309. DOI: <https://doi.org/10.1080/01431161.2015.1058004>
10. Ryabtsev, I.O., Knysh, V.V., Babinets, A.A. et al. (2020) Fatigue life of specimens after wear-resistant, manufacturing and repair surfacing. *The Paton Welding J.*, 9, 19–25. DOI: <https://doi.org/10.37434/tpwj2020.09.03>
11. Ryabtsev, I.O., Knysh, V.V., Babinets, A.A., Solovej, S.O. (2021) Fatigue life of steel 40Kh specimens after wear-resistant surfacing with a sublayer of low-carbon steel. *Ibid.*, 3, 2–8. DOI: <https://doi.org/10.37434/tpwj2021.03.01>
12. Oberg, E. et al. (1996) *Machinery's Handbook* (25<sup>th</sup> Ed.), Industrial Press Inc.
13. Murakami, Yu. (1990) *Reference book on stress intensity coefficients*. In: 2 Vol. Moscow, Mir [in Russian].
14. (2004) *Device for control of mechanical stresses and strains in solid media*. Pat. UA 71637 C2 [in Ukrainian].
15. Kaierle, S., Overmeyer, L., Alfred, I. et al. (2017) Single-crystal turbine blade tip repair by laser cladding and remelting. *CIRP J. Manuf. Sci. and Technol.*, 19, 196–199. DOI: <https://doi.org/10.1016/j.cirpj.2017.04.001>
16. Kim, D.-Y., Kim, D., Kang, M., Kim, Y.-M. (2017) Improvement of fatigue strength of lap fillet joints by using tandem MAG welding in a 590-MPa-grade galvanized steel sheet. *The Int. J. Adv. Manuf. Technol.*, 93(9–12), 4379–4387. DOI: <https://doi.org/10.1007/s00170-017-0828-6>.

Received 09.06.2021

**SEPTEMBER 1, 1939** Beginning of the Second World War. Preparation to it significantly effected application of electric welding in production of all types of arms. Germany in order to circumvent peace agreement started using welded joints in the defense industry. Series of technologies, such as underwater welding, received a large development in this time. During the first years of the war volume of welding engineering in America increased more than three times due to manual electric arc welding and submerged arc welding.



## DEVELOPMENT OF TECHNOLOGY FOR SURFACING WORKING LAYER OF VARIABLE COMPOSITION ON CRIMPING ROLLS

L.K. Leshchynskiy, V.P. Ivanov, V.M. Matviienko, K.K. Stepnov and E.I. Vozyanov

State Higher Education Institute «Pryazovskyi State Technical University»

7 Universytetska Str., 87555, Mariupol, Ukraine. E-mail:

It is shown that development of the technology for surfacing crimping rolls with the working layer of variable composition and mechanical properties along the body length makes it possible to minimize the unevenness of wear, especially in the area with its greatest depth. Application of this technology involves the use of a control system that provides separate control of the feed drive for each of the electrodes. It is shown that during surfacing of the crimping rolls with a layer of variable composition of the C–Cr–Mo–V alloying system, it is advisable to limit the content of elements within the ranges of 15Kh3GSMF – 24Kh4MFBS. It was demonstrated that the technology of surfacing crimping rolls with the working layer of variable composition is realized by feeding two strip electrodes LN-15Kh3GSMF and LN-24Kh4MFBS into the common weld pool. It was found that to obtain the required law of the change of the layer composition along the body length, the ratio of feed rates of the strip electrodes is changed in accordance with the carbon equivalent value of the metal of strip electrodes. It is shown that during operation of horizontal rolls of the slabbing mill, surfaced with a layer of variable composition, the unevenness of body wear decreases, and the operating time of rolls per 1 mm of wear of the working layer also increases. 9 Ref., 3 Tables, 2 Figures.

*Keywords:* surfacing, working layer, variable chemical composition, carbon equivalent, strip electrodes, crimping roll, uneven wear, law of hardness change

Improvement of the technology for surfacing crimping rolls is caused by the need in reducing the intensity and unevenness of the wear of the working layer, increasing in its resistance to wear and cyclic heating changes [1, 2]. The depth of the wear is uneven along the length of the body of the horizontal slabbing mill roll [3] and grows while moving further from the edge of the body, reaching the maximum value in the zone of slab edges location (30–450 mm from its edges), after which slightly decreases (Figure 1). Uneven wear leads to a change in the shape and sizes of the slab, causing a need in frequent roll changing and remachining. It is possible to minimize unevenness of the wear of a body by using the technology of electric

arc surfacing of the layer of a variable chemical composition [4]. This is carried out by feeding two electrodes, differing in the content of alloying elements evaluated by carbon equivalent and hardness, at a programmable rate into a common welding pool. Thus, in accordance with the profile of the wear of the roll, the dependence of the change in the deposited metal and its properties is provided.

Changing the content of alloying elements in the deposited working layer and its mechanical and operational properties not only reduces the unevenness of the wear to the minimum, but is also accompanied by the formation of areas on the surface of a body, that differ in composition and hardness from surrounding metal. This allows improving clamping of a billet by rolls. The technology of surfacing crimping rolls by the layer of variable chemical composition, which fully meets these requirements, involves the creation of a control system [4], which provides a separate control of drives for electrode feeding, and therefore, the necessary change in the composition and hardness of the deposited layer. The system also provides a trajectory of movement of the surfacing apparatus relative to the surface of the roll.

Based on the operating conditions, the working layer of the crimping rolls of steel of type 60KhN

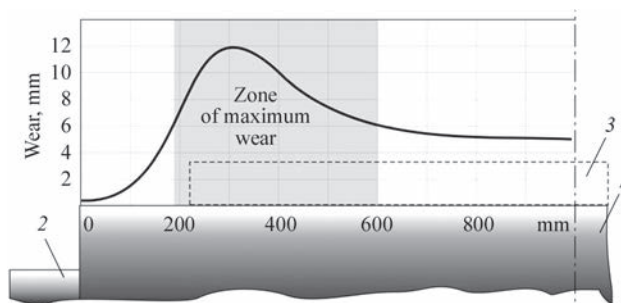


**Figure 1.** Nature of wear of a horizontal slabbing mill roll: 1 — body of a roll; 2 — neck; 3 — slab

L.K. Leshchynskiy — <https://orcid.org/0000-0002-7473-7510>, V.P. Ivanov — <https://orcid.org/0000-0003-3339-7633>, V.M. Matviienko — <https://orcid.org/0000-0002-8713-1630>, E.I. Vozyanov — <http://orcid.org/0000-0002-2034-1270>

© L.K. Leshchynskiy, V.P. Ivanov, V.M. Matviienko, K.K. Stepnov and E.I. Vozyanov, 2021

is characterized by hardness  $HV$  270–290, strength  $\sigma_{0.2} = 520\text{--}540$  MPa, ductility  $\psi = 30\text{--}35$  % and impact toughness of 0.20–0.25 MPa [5]. Higher requirements to the properties of the deposited layer provide a combination of optimal hardness values ( $HV \leq 400$ ), technological strength ( $A_{cr} \geq 10\text{--}12$  mm/min), ductility ( $\psi \geq 40\text{--}45$  %), dynamic crack resistance (impact toughness  $KC \geq 0.30\text{--}0.33$  MJ/m<sup>2</sup> and coefficient of stress intensity  $K_{ID} \geq 26.0\text{--}28.0$  MPa·m<sup>1/2</sup>). These properties are characteristic for steels 15Kh3M1F, 20Kh2M2FN, 25Kh5FMS, which are deposited by corresponding electrode materials [6]. At the same time, producing the layer of variable chemical composition with a continuous change in the content of alloying elements, it is advisable to use surfacing materials of the alloying system C–Cr–Mo–V, limiting the content of chromium (2.5–5.0 %), carbon (0.15–0.25 %), molybdenum (0.6–1.3 %), vanadium (0.15–0.40 %) and niobium (0.15–0.25 %). In [7], as a lower limit of this area, the composition 16Kh4GMFS (carbon equivalent  $C_e = 1.273^*$ , hardness  $HV$  345) is proposed. At the same time, the upper limit is the composition 25Kh5FMS ( $C_e = 1.707$ ;  $HV$  420), which is characterized by a high wear resistance in combination with a sufficient ductility.

However, taking into account the variable high intensity thermal power loads that affect the crimping roll, for surfacing of the working layer, it is advisable to use materials with a higher ductility and crack resistance. Therefore, for the lower limit of the area of alloying, a deposited metal 15Kh3GMFS ( $C_e = 1.066$ , hardness  $HV$  305) was selected. At the same time, for the upper limit, the deposited metal 24Kh4MFBS ( $C_e = 1.45$ ,  $HV$  400), in which as compared to the deposited metal 25Kh5FMS the content of chromium and carbon is reduced, as well as niobium introduced. In this case, the change in carbon equivalent  $C_e$  in the range of 1.07–1.45 is accompanied by an increase in the metal hardness  $HV$  from 305 to 400, but to a lesser extent — a decrease in impact toughness (Table 1). The latter is explained by the presence of batch martensite in the structure, which affects the energy-in-

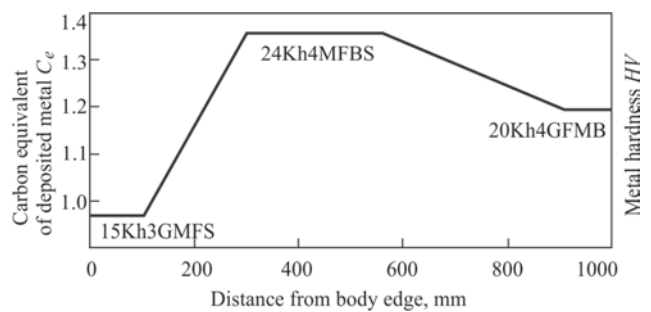


**Figure 2.** Change in carbon equivalent  $C_e$  and hardness of deposited metal

tensive destruction mechanism — transcrystalline chipping and microtough pit one.

In steel 15Kh3GMFS, containing (wt.%): 0.15 C; 3.2 Cr; 0.3 Mo; 0.08 V; 1.2 Mn; 0.5 Si ( $C_e = 1.066$ ), after surfacing and thermocyclic tempering, a ferrite-cementite structure is formed, in which ~ 10% of free ferrite is formed, and carbide phase is represented by large plates of cementite [7]. Such a structure is characterized by a low hardness  $HV$  305 (HSD 46), high ductility, impact toughness and crack resistance during cyclic heat changes (see Table 1). The mechanism of destruction of such a structure is mainly microtough pit one. At the same time, as a result of the limited resistance to friction wear at elevated temperatures, it is rational to use the composition 15Kh3GMFS for surfacing the edge of a body (Figure 2). Moving further from the edge, the composition and hardness of the deposited layer are changed by the law, given in Figure 2 in such a way, that the maximum value of the carbon equivalent and metal hardness can be achieved on the area of the most intensive wear. This area on the body of the roll is located in the zone of the slab edge (for a horizontal slabbing mill roll it is ~ 400 mm from the edges of the body) (Figure 2). To such a value  $C_e$ , the composition 24Kh4MBFS corresponds, which contains (wt.%) 0.24 C; 4.2 Cr; 0.8 Mo; 0.40 V; 0.25 Nb; 0.8 Mn; 0.5 Si, which provides the hardness  $HV$  400 (HSD 57) and a high wear resistance. These characteristics are remained unchanged on the body area (Figure 2), and

**Table 1.** Operational properties of deposited metal

Metal composition	$A_{cr}$ , mm/min	$KC^{**}$ , MJ/m <sup>2</sup>	$K_{ID}$ , MPa·m <sup>1/2</sup>	Number of cycles heating-cooling until cracking	Relative wear resistance at 600 °C
15Kh3GMFS	11.9	0.46	29.5	1930	1.0
20Kh4GFMB	11.3	0.40	28.6	1800	1.3
24Kh4MFBS	11.0	0.37	28.5	1670	1.5

\*\*Tests for determination of  $KC$  and  $K_{ID}$  were carried out at 20 °C.

\*Calculation of values of carbon equivalent  $C_e$  was carried out according to the dependence proposed by the International Institute of Welding.

**Table 2.** Influence of ratio of feed rates of strip electrodes LN-15Kh3GMFS and LN-24Kh4MFBS on the value  $C_e$  and metal properties

Ratio of rates	$C_e$	HV (HSD)	$\psi$ , %	$\sigma_{0.2}$ , MPa
100/0	1.066	305 (46)	57.0	680
40/60	1.297	365 (53)	53.0	740
0/100	1.453	400 (57)	48.0	780

then, reducing the carbon content to 0.20 %, a change in the composition of the deposited layer (20Kh4G-FMB) is provided. Here,  $C_e$  is reduced to 1.297, and the hardness of metal — to HV 365 (HSD 53), in its structure martensitic matrix with relatively large primary and dispersed secondary chromium, niobium and vanadium carbides is observed.

In accordance with the developed materials, at the Illich Steel and Iron Works an industrial production of cold-rolled alloyed strip of 1.0<sup>-0.2</sup> mm thickness and 30 mm width and production of strip electrodes for surfacing of rolling mills were mastered [8, 9]. During strengthening of the horizontal slabbing mill roll, surfacing layer of variable chemical composition is provided by feeding of two strip electrodes LN-15Kh3GMFS and LN-24Kh4MFBS to a common weld pool at an adjustable rate. The ratio of the mass rate of their feeding (at a constant total rate) is selected based on the carbon equivalent value in such a way as to obtain the composition of the body with the minimum  $C_e$  value (to which steel 15Kh3GMFS corresponds). Further, changing the ratio of feed rates, an increase in  $C_e$  value to its maximum value is provided (to which steel 24Kh4MFBS corresponds). The mode of surfacing with two strip electrodes with a total cross-section of 60 mm<sup>2</sup> is the following: current of constant reverse polarity  $I_s = 700-740$  A,  $U = 34-36$  V,  $v_s = 10.5$  m/h; total volume rate of feeding two strips 0.9 cm<sup>3</sup>/s.

Industrial operation of deposited horizontal slabbing mill rolls 1150 with the working layer of variable chemical composition showed that the unevenness of the body wear decreased, and also the work of 1 mm wear of the working layer increased (Table 3).

Thus, the use of the technology of surfacing the working layer of variable chemical composition and hardness for strengthening of the horizontal slabbing rolls provides stabilization of the output profiling due to a more even wear of bodies. This improves the slabs geometry, which during a further rolling on a broadstrip mill allows reducing the

**Table 3.** Results of operation of deposited crimping rolls

Horizontal rolls of slabbing mill 1150	Volume of rolled metal, thou t	Operation per 1 mm of wear, t/mm
Rolls of steel 60KhN	825.0	22.0
Rolls, deposited by the layer of constant composition	927.0	38.4
Rolls, deposited by the layer of variable composition	1050.0	43.5

metal consumption associated with a tolerance to the width of the strip.

**Conclusions**

During investigations it was established:

1. It is rational to perform the development of the technology of surfacing mill rolls by the layers of variable composition at a given alloying system, choosing the ratio of feed rates of electrodes with the smallest and largest carbon equivalent value, which determines the properties of the deposited metal.
2. The application of the technology of surfacing horizontal slabbing rolls by the working layer of variable chemical composition and properties leads not only to eliminating an uneven wear, but also to increase in the operation of rolls per 1 mm of wear of the working layer.

1. Ryabtsev, I.A., Kondratiev, I.A., Vasiliev, V.G. et al. (2010) Investigation of structure and service properties of deposited metal for reconditioning and strengthening of rolling mill rolls. *The Paton Welding J.*, **7**, 12–15.
2. Ryabtsev, I.A., Babinets, A.A., Gordan, G.N. et al. (2013) Structure of multilayer samples, simulating surfaced tools for hot deforming of metals. *Ibid.*, **9**, 41–45.
3. Matvienkov, S.A., Shebanits, E.N., Murashkin, A.V. et al. (2012) Surfacing of working and backup rolls using the ceramic flux I-KF-45-65 at MMK im. Ilyicha. *Metall i Litio Ukrainy*, **2**, 50–54 [in Russian].
4. Ivanov, V.P., Leshchynskiy, L.K., Shcherbakov, S.V. (2019) Modeling the technology of deposition of a layer of variable chemical composition. *The Paton Welding J.*, **11**, 33–37.
5. Corbett, R. (1990) *Rolls for metalworking industries*. Warrendale, Iron & Steel Society.
6. Ryabtsev, I.A., Senchenkov, I.K. (2013) *Theory and practice of surfacing works*. Kiev, Ekotekhnologiya [in Russian].
7. Samotugin, S.S., Lavrik, V.P., Leshchinskyi, L.K., Solyanik, N.H. (2001) Plasma treatment of sparcely-alloyed heat-resistant deposited metal. *Problemy Spets. Elektrometallurgii*, **2**, 26–31 [in Russian].
8. Leshchinskiy, L.K., Ivanov, V.P., Maslov, A.A. at al. (1997) *Electrode strip for surfacing*. Pat. 2087589 RU, Int. Cl. B23K020/227 [in Russian].
9. Boiko, V.S., Stepnov, K.K., Shebanits, E.M. et al. (2003) *Electrode strip for surfacing*. Pat. 62591 UA, Int. Cl. B23K 35/00 [in Ukrainian].

Received 01.07.2021

# DEVELOPMENT OF TECHNOLOGY OF MANUFACTURE OF DRILL BITS WITH PROTECTIVE COATING OF WORKING BODIES

**B.V. Stefaniv**

E.O. Paton Electric Welding Institute of the NAS of Ukraine

11 Kazymyr Malevych Str., 03150, Kyiv, Ukraine. E-mail: [office@paton.kiev.ua](mailto:office@paton.kiev.ua)

The peculiarities of manufacturing drill bits and cutters are considered and studied. The carried out analysis of operation of working bodies of drill bit frames showed that during drilling most often a wear of cutters, a protective coating of sitters and a calibrating surface of frames of drilling bits occur. It was investigated that in arc surfacing using TIG method, low rates of heating and cooling of metal during preheating of working bodies of a bit allow reducing residual stresses and avoiding the formation of cracks in coatings and base material. It was established that the optimal thickness of surfacing the protective coating should be within 2.0–3.0 mm, where a uniform distribution of tungsten carbides throughout the volume of the deposited layer is observed, which effectively resists wear of the working bodies of blades and frames of bits in the conditions of alternating and shock loads, hydroabrasive wear, corrosion, erosion, etc. It was established that bits with a protective coating, having a high wear and corrosion resistance, increase the mechanical speed of drilling and solve the most important task of reducing the number of lowering and lifting operations when drilling gas and oil wells. As a result of carried out production tests of manufactured drill bits, it was found that protective coating of working bodies allows extending the service life. 18 Ref., 1 Table, 8 Figures.

*Key words:* bits, cutters, drilling, wear, working body, polycrystalline diamond cutter (PDC), hard-alloy coating, surfacing, tungsten carbides, microstructure, wear resistance, tests

For effective drilling of subsoils for extraction of hydrocarbons requires a proper choice of a bit under certain operating conditions. The main drilling tool is a bit for rotational drilling (which, broadly speaking, is classified as a bit with fixed cutters or as a cone bit) is intended for different rocks and a wide range of conditions. Today at the Ukrainian market drill bits are represented by bits of domestic and foreign production.

In the world there are more than three dozen companies engaged in development and production of a drilling tool. The leading place is occupied by «Varel International», «Hughes Christensen», «Halliburton», «Smith Bits», «Reed Hycalod», «National Oilwell Varco», «Schlumberger», «Reed Tools Company», «Baker Hughes» and «Gemdrill», etc. These companies deliver tools to more than 86 countries. The share of imported drill bits in the Ukrainian market for oil and gas industry amounts to about 12 %, and for mining it is 14 %.

The main characteristics of wearing out PDC bits (of both own as well as foreign production) in deposits of Ukraine are: wear of teeth — 17 %, breakage of teeth — 30 %, chipping of teeth — 31 %, loss of teeth — 3 and 19 % — absence of wear [1].

In Ukraine, PDC and cone bits are produced by the V.M. Bakul Institute for Superhard Materials [2] and the Drohobych Drill Bits Plant «LLC «Universal drilling equipment» [3]. The disadvantage of PDC bits produced by the V.M. Bakul Institute for Superhard Materials is insufficient protection of working bodies, namely blades and calibrating surface of the frame without a protective coating, which significantly affects their wear resistance and service life.

At the Drohobych Drill Bits Plant «LLC «Universal drilling equipment», tricone drill bits are mostly produced, in which cutters are equipped with insert hard-alloy teeth. The disadvantage of cone bits is an insufficient protection of working bodies, namely the loss of fragments of a cutter (splitting of cutter body, breakage of leg axle), rolling bodies (jamming of supports and stop of cutters rotation) or an entire section (splitting, wear, loss of insert rock-destruction mountings of cutters).

The use of PDC bits with a protective coating of working bodies provides an increase in sinking by an order and more as compared to cone bits and bits without a protective coating and reducing the cost of lowering-lifting operations. This indicates the need in further investigations in the direction of analysis and selection of data on drilling, since drilling with the use of PDC bits allows facilitating drilling works, shortening terms of wells construction, especially in the process of drilling deep wells, and the absence of

moving elements in the design of bits excludes the emergency situations. The design of PDC bits provides a long-term service life and high drilling speeds due to a high wear resistance of the protective coating of working bodies and cutting elements of PDC-cutters, the absence of a bearing support, which improves sinking of drilling tool. Insignificant effect of a bit operation dynamics on the bottom-hole and a drill rod (as compared to cone bits) and a high wear resistance of the protective coating and cutters of a calibrating surface exclude the need in reaming and calibrating wellbore before lowering of a frame column.

For drilling tool, the main indices of mechanical properties of wear-resistant coatings are hydroabrasive wear resistance, hardness and corrosion resistance, which provides an effective resistance to a number of problems of wearing working bodies of bits in the conditions of alternating and shock loads, hydroabrasive wear, corrosion, erosion, etc. The strength of the protective coating depends on temperature, pressure, mechanical load, aggressiveness of the medium and strength of rocks. Having a high wear and corrosion resistance, bits with a protective coating increase the speed of mechanical drilling and solve the most important task of reducing the cost of a meter of sinking.

Taken into account the abovementioned, the aim of the work consisted in development of a technology for manufacture of drill bits with a protective coating of the working bodies, which provides an extension of the service life.



**Figure 1.** Scheme of arrangement of working bodies of a bit: 1 — cutter; 2 — hard-alloy insert of calibration surface; 3 — interblade space for sludge removal; 4 — protective coating of watercourse; 5 — hard-alloy nozzle of watercourse; 6 — protective coating of working bodies of blades

**Materials and methods.** The object of investigations are the areas of working bodies of frames of steel drill bits. Examinations of microstructures were carried out according to the standard procedure in the Tescan Mira 3 LMU electron microscope and the Neophot 32 optical microscope. Welding devices: Koral-300 and PRS-3M. Composite material: Tero Cote 7888T.

**Results of investigations.** To protect working bodies of drilling tool from different types of wear, composite materials based on Ni, Fe, NiCr, NiCrBSi, copper, etc. alloys reinforced with tungsten carbides are widely used [4, 5]. This is primarily associated with the unique properties of the reinforcing phase of such alloys — tungsten carbides. Tungsten carbide is one of the hardest and most shock-resistant carbides, and surfacing of a hard-alloy coating (HAC) is a fast method to deposit a tungsten carbide coating on the areas of working bodies exposed to the action of intense abrasive loads and it help to maintain mechanical properties over a wide temperature range, resistant to frictional corrosion and is able to form a strong bond with metals [6, 7].

The carried out studies of wear resistance of composite materials in the conditions of hydroabrasive wear showed that wear resistance of the protective coating TeroCote 7888T based on Ni-Cr-B-Si system with chipped tungsten carbide particles exceeds the wear resistance of relite «L3-11-7» and Diamax M [8]. According to the results of investigations on wear resistance, the alloy TeroCote7888T was selected, on the basis of which studies of this material on corrosion resistance were carried out. The results of studies of corrosion resistance showed [9] that the use of a protective coating deposited using a composite material TeroCote 7888T provides a significant reduction in the corrosion rate of steel working bodies of drill bits without a protective coating. Based on the results of studies of hydroabrasive and corrosion wear of composite materials, the main attention was paid to this alloy, which belongs to the category of corrosion-resistant protective materials.

The stability and performance of drilling with the use of steel bits having a protective coating directly depends on the ability of cutting structure elements in the form of polycrystalline diamond cutters and hard-alloy inserts to resist abrasive wear of the blades around these elements, which strive to destroy the system for fixation of these rock-destroying elements (Figure 1). In particular, abrasive wear of steel areas of the blades located around the cutting and calibrating elements, as well as the brazing alloy that keeps them from pulling, promotes an uncovering, increase

in the size of the protrusion and a gradual loss of individual elements.

To determine the thickness of the protective coating of working bodies of bits, research works on surfacing of the composite TeroCote 7888T alloy were carried out. Surfacing was performed by TIG method on the specimens of 30Kh steel of 14 mm thickness. During surfacing of a wear-resistant layer of up to 1.5 mm (Figure 2, *a*) on the specimens, a chaotic arrangement of tungsten carbide particles, and at 2.0–3.0 mm (Figure 2, *b*) — a uniform arrangement of tungsten carbides throughout the entire volume of the deposited layer is observed. With an increase in the coating thickness of 3.5 mm (Figure 2, *c*), a bulk of the tungsten carbide particles is located in the lower and middle zones, and it is practically absent in the upper zones. All this can be explained by physical properties of the composite material, because the matrix material contains 65 % of tungsten carbides. A high content of tungsten carbides does not allow the matrix material to get wet and spread on the surface of the base metal.

Based on the results of the carried out works, it can be stated that the optimal thickness of surfacing should be within 2.0–3.0 mm, where a uniform distribution of tungsten carbides throughout the volume of the deposited layer is observed, whereas at a smaller thickness, tungsten carbide particles are located in the upper zone, and at a larger one, tungsten carbide particles are mainly located in the middle and lower zones of surfacing. The thickness of the deposited wear-resistant layer in the range of 2.0–3.0 mm provides an effective protection of the surface of the working body of a steel drill bit from corrosion, erosion and abrasive wear during drilling of gas and oil wells.

The technology of manufacturing drill bits with a protective coating of working bodies requires a number of technological operations. From its own developments on the base of the E.O. Paton Electric Welding Institute of the NAS of Ukraine such a technological scheme was created:

- designing of a bit taking into account well conditions;
- manufacture of bit parts at the five-coordinate processing center (CNC);
- surfacing of wear-resistant hard-alloy material on working bodies;
- mounting and brazing of cutters and hard-alloy inserts;
- treatment of surfaces of a bit to the size;
- tests.

The choice of drill bit types at the designing stage was made in two ways: according to mechanical and abrasive properties of rocks and on the basis of in-

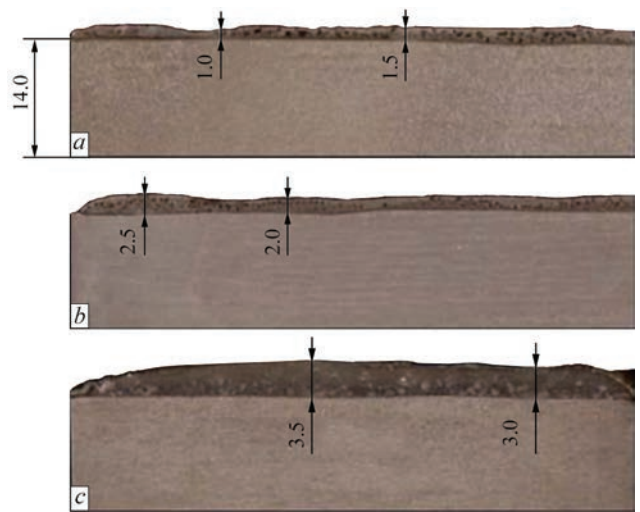


**Figure 2.** Deposition of wear-resistant coating on specimens: *a* — 1.0–1.5; *b* — 2.0–2.5; *c* — 3.0–3.5 mm

dustrial data. The design of a drill bit was based on six factors of influence, namely: characteristics of drilled out rocks according to [10], drill bit diameter, load, number of rotations, volume of flushing fluid, bottom-hole pressure. Of course, the mentioned parameters do not fully describe all possible factors of influence, but they were chosen by us because namely these parameters are recorded in drilling logs. An additional parameter for bits of domestic production was drilling type (1 — rotary; 2 — turbine).

At the stage of designing drill bits, information on operation performance was used. Such information was obtained from the data of wear-out time of similar structures in real drilling conditions. Modeling of drill bits with a diameter of 165.1 mm (Figure 3) was carried out based on the results of our previously carried out works on underground and surface drilling of soft-medium, medium and hard rocks for extraction of dispersed methane and natural gas [11]. According

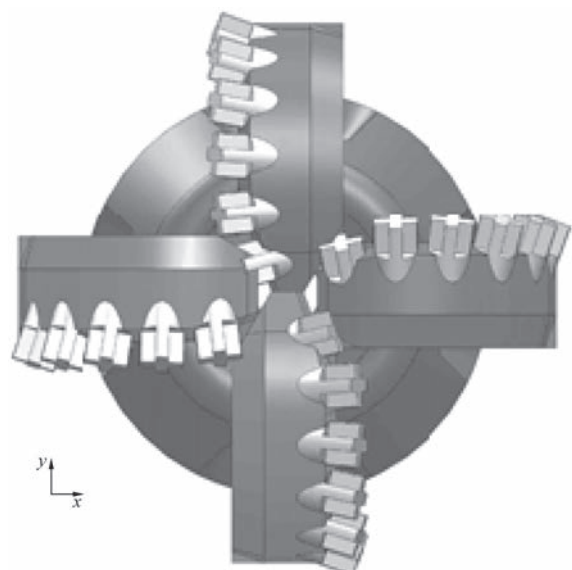


**Figure 3.** Modeling of cutters of blades of bit frame



Figure 4. Frame of an integrally-milled bit

to the results of the works carried out at the PWI, designs of drill bits and calibrators were developed and patents for their invention were obtained [12, 13].

The manufacture of a drill bit included turning and milling of the frame, drilling of the central channel of the frame and boring of channels for flushing fluid supply to cool the blades and cutting edges of diamond-hard alloy cutters. The works were performed at a five-coordinate processing center (CNC). The billets of frame for integrally-milled bits (Figure 4) and billets of frame and blades for combined (Figure 5) drill bits were made. Combined bits differ from integrally-milled ones in the fact that the frame of a bit is joined to the blades by welding, which allows reducing the cost of manufacturing bits.

Welding of the blades with the frame of a drill bit was performed by argon arc welding in a pure argon of grade A using nonconsumable electrode in the apparatus «Koral-300». The root of the weld was pro-

duced with filler wire of grade VNS-17 (03Kh11N-10M2T) of 2 mm diameter. The welding current is  $I = 140\text{--}150$  A, voltage is  $U = 11\text{--}12$  V. Reinforcement of the leg of the weld was performed using a filler wire of grade 18Kh4GMA of 3 mm diameter ( $I = 160\text{--}170$  A,  $U = 12\text{--}13$  V). To relieve welding stresses in the welds, the bit was tempered in a furnace at a heating temperature of  $640$  °C for 2 h. The bit was cooled in air. The hardness after tempering was *HB* 179.

According to the results of the carried out works [14, 15] on deposition of a protective coating of the working bodies of frames of drill bits, a composite material TeroCote 7888 T was chosen, which wets the base metal well and has no defects during surfacing of a layer on the leading and running-off areas of mounting sockets for diamond hard-alloy cutters (DHAC). During the development of the technology of surfacing corrosion-resistant layer to the areas of the working bodies of the bits, a preference was given to arc surfacing. The essence of the surfacing process consists in using heat for melting filler material and its joining with the base metal of a bit frame. The need in using local heating of the working bodies of a bit frame is predetermined by low values of flowability and spreading of the composite material, which contains about 65 wt.% of particles of tungsten carbides as compared to its base – high-temperature alloy of the metal system Ni–Cr–B–Si. Using the possibilities of arc surfacing, on the surface of the blades it is possible to produce a deposited layer of the required thickness and chemical composition with the desired properties.

Before deposition of the protective coating on the areas of the working bodies, graphite plugs should be tightly mounted into the sockets of the blade holes, which make it possible to protect these holes from leakage of the deposited wear-resistant alloy during surfacing and a preheating of the working bodies of the frame to the temperature of  $400\text{--}500$  °C should be carried out. During surfacing of the areas of the working bodies (Figure 6, *a*), two sources of thermal



Figure 5. Combined bit: *a* — frame; *b* — blades

## Arc surfacing modes

Voltage, V	Current type	Current, A	Argon flow rate, dm <sup>3</sup> /min	Surfacing rate, m/h	Power source
10–12	Direct, straight polarity	80–100	2.5–3.0	2–4	PRS-3M



**Figure 6.** Deposition of coating on working bodies of a bit: *a* — blade; *b* — bit after brazing of diamond-hard-alloy cutters and inserts

power were used: electromagnetic field of high-frequency alternating current (induction) for preheating of the frame, and a heat released by the TIG method of surfacing — deposition of the filler TeroCote 7888T alloy at a temperature of 1200–1250 °C (Table).

The average thickness of the deposited layer of the working bodies of the blades was 2–3 mm.

Brazing of diamond-hard-alloy cutters in the sockets of the holes of the working bodies of the blades of the bit frame was carried out at a temperature of 650–680 °C (Figure 6, *b*) because a higher temperature of heating begins to affect the strength properties of polycrystalline diamond cutters [16, 17]. All this can lead to graphitization of polycrystalline synthetic diamonds, formation of cracks caused by the difference in the coefficients of thermal expansion of diamond and cobalt, and, as a consequence, to the destruction of the diamond layer.

To determine microstructure of the protective coating, microsections of 30Kh steel with a deposited layer were made (Figure 7). Metallographic examinations showed that in TIG surfacing during the formation of the deposited layer, a uniform distribution of tungsten carbide particles throughout the volume of the composite material TeroCote 7888T occurs, which causes a uniform distribution of hardness along the depth of the coating.

The microstructure of the deposited layer of the steel bit contains a solid nickel-chromium solution reinforced with tungsten carbides and a content of silicon and boron depressants. The presence of boron and silicon in the composition of filler wires provides them with self-fluxing properties during surfacing on steel. Tungsten carbides of irregular shape (of different sizes) are distributed throughout the whole field of the microsection. It

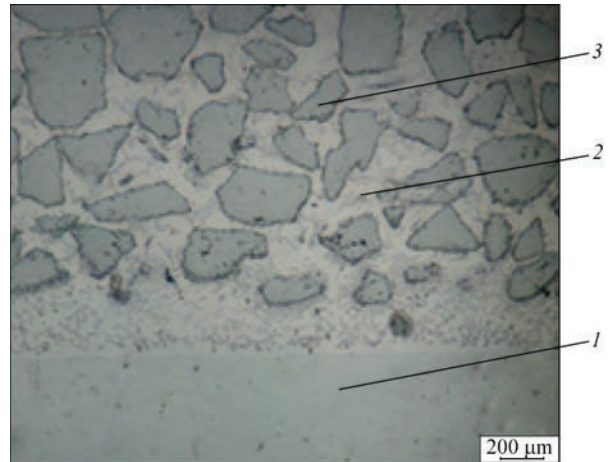


**Figure 7.** Microstructure of coating of a steel bit: *1* — 30Kh steel; *2* — matrix based on NiCrBSi alloy; *3* — tungsten carbides

is known from the literature that a high-quality wear-resistant coating should have a uniform distribution of solid phases with a distance between these phases smaller than the size of abrasive particles [18].

The produced structure of the deposited coating layer provides an effective protection of the surface of the working bodies of drill bits from erosion and abrasive wear caused by the influence of such materials as sand, gravel, earth, minerals, etc. A tough matrix of the deposited alloy absorbs shock loads and improves the corrosion resistance, whereas the special shape of tungsten carbides makes it impossible to pull them out from the matrix. The examinations showed that during TIG surfacing, low rates of heating and cooling of the metal during preheating of the working bodies of the bit allow reducing residual stresses and avoiding the formation of cracks in the coatings and the base material.

After each use, the bits are subjected to maintenance and repair. Repairs are carried out at the area of repair of the working bodies of bits applying the same



**Figure 8.** Drill bits with a protective coating: *1* — combined bit; *2* — integrally-milled bit; *3* — calibrator

technology as in the production of new drill bits. A batch of drill bits and calibrators with a protective coating of working bodies of 165.1 mm diameter, manufactured at the PWI, successfully passed tests during drilling wells in oil and gas condensate fields of Kharkiv region (Figure 8).

### Conclusions

1. It was established that optimal thickness of surfacing of the protective coating should be within 2.0–3.0 mm, where a uniform distribution of tungsten carbides throughout the whole volume of the deposited layer is observed.

2. According to the results of production tests of steel drill bits, it was established that using of these bits with a protective coating of the working bodies allows increasing the service life during drilling of gas and oil wells.

1. Draganchuk, O.T., Prygorovska, T.O. (2008) Analysis of drilling bit wear of PDC type in deposits of Ukraine and world. *Naftogazova Energetyka*, 9(4), 33–39 [in Ukrainian].
2. Bondarenko, N.A. (2018) High-efficient diamond tool ISM for drilling of oil and gas wells: Review. *Sverkhvorydye Materialy*, 5, 79–92 [in Russian].
3. Yakym, R.S. (2014) Evaluation of reliability and criteria of quality improvement of tricone drill bits for drilling of extra hard rocks. *Rozvidka ta Rozrobka Naftovykh i Gazovykh Rodovyshch*, 53(4), 43–51 [in Ukrainian].
4. *Wear-resistant materials. Rods for gas and TIG welding.* <https://docplayer.ru/32381351-Iznosostoykie-materialy-i-tvyordye-splavy-na-osnove-kobalta.html>
5. *Materials for brazing and surfacing.* TeroCote. <http://www.castolin.com.ua>
6. Samsonov, G.V., Vitryanyuk, V.N., Chaplygin, F.I. (1974) *Tungsten carbides*. Kiev, Naukova Dumka [in Russian].
7. Pierson, H.O. (1996) *Handbook of refractory carbides and nitrides*. New Jersey, Noyes Publications.
8. Stefaniv, B.V. (2016) Investigation of wear resistance of protective coatings under conditions of hydroabrasive wear. *The Paton Welding J.*, 9, 26–29.
9. Stefaniv, B.V., Nyrkova, L.I., Larionov, A.V., Osadchuk, S.O. (2020) Corrosion resistance of composite material deposited by TIG method using flexible cord TeroCote 7888T. *Ibid.*, 2, 29–32. DOI: <https://doi.org/10.37434/as2020.02.05>
10. Sajfutdinov, A.B., Sharnin, M.Yu. (1998) Efficiency of drill bits PDC. *Neftyanoe Khozyajstvo*, 9 [in Russian].
11. Khorunov, V.F., Maksymova, S.V., Stefaniv, B.V. (2010) Manufacture of drill bits for production of dispersed methane in mine working. *The Paton Welding J.*, 6, 48–51.
12. Paton, B.E., Stefaniv, B.V., Khorunov, V.F. et al. (2009) *Diamond drill bit*. Ukraine Pat. 92268, (51), Int. Cl. E21B 10/46 E21B 10/5; Fill. 05.05.2009; Publ. 11.10.2010 [in Ukrainian].
13. Paton, B.E., Stefaniv, B.V., Khorunov, V.F. et al. (2009) *Calibrator*. Pat. Ukraine 92820, (51), Int. Cl. E21B 10/26 E21B 7/28; Fill.10.03.2009; Publ. 10.12.2010 [in Ukrainian].
14. Stefaniv, B.V., Khorunov, V.F., Sabadash, O.M. et al. (2014) Features of reconditioning steel drill bit watercourse. *The Paton Welding J.*, 11, 50–54.
15. Stefaniv, B.V., Khorunov, V.F., Sabadash, O.M. et al. (2015) Peculiarities of restoration of working parts of drilling bit matrix bodies. *Ibid.*, 8, 47–50.
16. Stefaniv, B.V. (2013) Development of the technology of brazing diamond-hard alloy cutters. *Ibid.*, 2, 37–41.
17. Stefaniv, B.V. (2013) Peculiarities of induction brazing of diamond-hard alloy cutters to blade of body of complex drill bit. *Ibid.*, 8, 49–53.
18. *Wear-resistant materials.* [http://www.svarka52.ru/upload/osnovnoi\\_katalog\\_po\\_paike\\_i\\_Terocote\\_BRAZING\\_1.pdf](http://www.svarka52.ru/upload/osnovnoi_katalog_po_paike_i_Terocote_BRAZING_1.pdf)

Received 21.06.2021

## XX INTERNATIONAL INDUSTRIAL FORUM - 2021

INTERNATIONAL TRADE FAIRS

 METAL WORKING
  UKWELD
  HYDRAULICS PNEUMATICS
  BEARINGS
  GREEN TECH
  UKFOUNDRY
  AUTOMATION
  PATTERNS, STANDARDS AND INSTRUMENTS
  HOISTING AND TRANSPORTING STOREHOUSE EQUIPMENT
  INDUSTRIAL SAFETY

November  
16-19



**ORGANIZER:**  
International Exhibition Centre

General Information Partner:  


Exclusive Media Partner:  
ЖУРНАЛ ГОЛОВНОГО ІНЖЕНЕРА

Technical Partner:  


  
International Exhibition Centre  
15 Brovarskyi Ave., Kyiv, Ukraine  
“Livoberezhna” underground station  
☎ +38 044 201 11 65, 201 11 56, 201 11 58  
e-mail: alexk@iec-expo.com.ua  
[www.iec-expo.com.ua](http://www.iec-expo.com.ua)  
[www.tech-expo.com.ua](http://www.tech-expo.com.ua)

# INFLUENCE OF ALLOYING ELEMENTS ON SOLIDUS AND LIQUIDUS TEMPERATURES OF ALLOYS OF Cu–Mn–Ni–Si SYSTEM

S.V. Maksymova, I.V. Zvolinsky and E.V. Ivanchenko

E.O. Paton Electric Welding Institute of the NAS of Ukraine

11 Kazymyr Malevych Str., 03150, Kyiv, Ukraine. E-mail: [office@paton.kiev.ua](mailto:office@paton.kiev.ua)

Plasma brazing of steels is performed using brazing filler metals having liquidus temperature higher than 1000 °C. This work shows the possibility of lowering the brazing temperature by applying brazing filler metals having a lower melting temperature. The method of high-temperature differential thermal analysis was used to establish the influence of manganese, nickel and silicon on solidus and liquidus temperatures of experimental alloys of the Cu–Mn–Ni–Si system. Empirical data and mathematical processing methods were applied to determine the influence of chemical elements on calculated coefficients of the impact of alloying elements on solidus and liquidus temperatures of alloys of the Cu–Mn–Ni–Si system that promotes lowering of melting temperature. The influence of nickel and silicon content at a fixed quantity of manganese of 10 and 16 wt.% on the spreading area over 08kp (rimmed) steel and melting temperature range was studied. High-quality formation of brazed joints from 08kp alloy produced by plasma brazing with application of the studied alloys was proved experimentally. 16 Ref., 2 Tables, 5 Figures.

*Keywords:* plasma brazing, spreading area, solidus and liquidus temperature, high-temperature differential thermal analysis, melting temperature range

Currently, as an alternative to MIG brazing, the process of plasma brazing is developed, in which two independent arcs are used — pilot and primary one. Pilot arc is burning between the nozzle and tungsten electrode, and primary arc is burning between the tungsten electrode and a product. Brazing is performed using an direct constant and modulated current, the brazing filler metal is supplied automatically. Plasma brazing is quite successfully applied to join parts in the manufacture of car bodies, metal-plastic windows and ventilation boxes [1–6]. For plasma brazing, a wide range of standard copper based alloys is proposed, which are divided into three groups, depending on the nature of alloying (Table 1).

Most often bronzes alloyed with silicon (SG–CuSi<sub>3</sub>) and aluminium (SG–CuAl<sub>8</sub>) are used. All brazing filler metals have a liquidus temperature of about 1000 °C and higher. A decrease in the melting tem-

**Table 1.** Chemical composition of brazing filler metals and melting temperature [7, 8]

Order number	Bronze grade	Melting temperature interval, °C
1	SG–CuSi <sub>3</sub>	910–1025
2	SG–CuSn <sub>6</sub>	910–1040
3	SG–CuAl <sub>8</sub>	1030–1040

\*\*Here and further wt.%.

S.V. Maksymova — <https://orsid.org/0000-0003-0158-5760>, I.V. Zvolinsky — <https://orsid.org/0000-0003-1442-7980>, E.V. Ivanchenko <https://orcid.org/0000-0001-7417-4087>

© S.V. Maksymova, I.V. Zvolinsky and E.V. Ivanchenko, 2021

perature of the brazing filler metal allows reducing the input energy required to produce high-quality brazed joints [6, 9, 10]. This leads to a decrease in residual stresses and an increase in the life of brazed joints.

The aim of the work is to establish the regularities of the influence of Mn, Ni and Si on the solidus and liquidus temperature of alloys of the Cu–Mn–Ni–Si system, which are used as brazing filler metals in plasma brazing.

**Procedure of experiment.** For investigations, cast brazing filler metals were produced in a laboratory electrode installation (Figure 1) on a copper water-cooled substrate in a purified argon.

As the source components, materials with cleanliness of not lower than 99.95 wt.% were used. The solidus and liquidus temperature of the produced alloys was determined by the method of high-temperature differential thermal analysis in the VDTA-8M installation in helium at heating and cooling rates of 40 °C/min. Based on the multifactorial planning method [11] and the analysis of binary diagrams of the state Cu–Mn, Cu–Ni and Cu–Si [12, 13], a matrix with a variable composition of alloying elements Mn, Ni and Si was plotted. Cu–13Mn–2Ni–2Si\*\* alloy with a solidus temperature of 823 °C, and a liquidus one of 962 °C (interval of crystallization temperature is 139 °C) was selected as the base one. Concentration borders of manganese



**Figure 1.** Laboratory installation for melting brazing filler metals in argon

(10–16 wt.%) were selected based on the analysis of binary diagrams of the state copper-manganese [12] with the account of the melting temperature interval.

The wetting of the experimental brazing filler metals of steel 08kp was performed using arc (TIG) method that contributes to the uniform heating of the larger area of the base metal substrate as compared to plasma heating [14]. The heating temperature was monitored using the Cr/Al thermocouple and the TRM device.

The ends of the thermocouple were welded-on from the reverse side of the base metal (substrate) to produce a hot brazing filler metal. The calculation of the obtained experimental data from spreading (spreading area) was carried out using AutoCard software.

For plasma brazing of specimens from steel 08kp, the power source KEMPPi Master TIG 2300 with a plasma module was used.

According to the standard procedure, microsections were prepared that were investigated without chemical etching using the TescanMira 3 LMU electron scanning microscope.

**Results of experiments and their analysis.** The influence of alloying elements Mn, Ni and Si to the liquidus and solidus temperature of copper-based alloys was evaluated using formulas (1) and (2). In fact, this implies the decomposition of the function of influence in a series of Taylor [15, 16] in the area of melting pure copper.

$$T_{(Cu)}^{sol} = T_{Cu} + \left( \frac{\partial T_{Cu}}{\partial C_{Mn}} \right)^{sol} C_{Mn} + \left( \frac{\partial T_{Cu}}{\partial C_{Ni}} \right)^{sol} \times C_{Ni} + \left( \frac{\partial T_{Cu}}{\partial C_{Si}} \right)^{sol} C_{Si}; \quad (1)$$

$$T_{(Cu)}^{lic} = T_{Cu} + \left( \frac{\partial T_{Cu}}{\partial C_{Mn}} \right)^{lic} C_{Mn} + \left( \frac{\partial T_{Cu}}{\partial C_{Ni}} \right)^{lic} \times C_{Ni} + \left( \frac{\partial T_{Cu}}{\partial C_{Si}} \right)^{lic} C_{Si}, \quad (2)$$

where  $\frac{\partial T_{Cu}}{\partial C_i}$  is the tangent of the inclination angle of

the solidus and liquidus lines near the melting point of pure copper on the diagrams of the state of the respective binary systems [13]. The area of the used alloying concentrations show that the dependence of solidus and liquidus temperature can be accepted as

close to the linear and the ratio  $\frac{\partial T_{Cu}}{\partial C_i}$  can be changed for  $\frac{\Delta T_{Cu}}{\Delta C_i}$ , which indicates the influence of Mn, Ni

and Si on the solidus and liquidus temperature of copper-based alloys within the alloying complex, %: 1–3 of silicon; 1–3 of nickel and 10–16 of manganese. According to the results of calculations, it was determined that silicon greatly affects a decrease in the solidus and liquidus temperature (Table 2).

The calculated coefficients of the influence of alloying elements on the solidus and liquidus temperature in the alloys of the Cu–Mn–Ni–Si system show that at a set change in the concentration interval of the alloying elements, a decrease in the solidus and liquidus temperature is more strongly influenced by a silicon content with a coefficient of –40.5 for solidus temperature and –23.5 for liquidus one. The amount of manganese affects the decrease in the solidus and liquidus temperature to a lower extent, which is indicated by lower values of the coefficients: –8.3 and –0.33 (for solidus and liquidus temperature, respectively).

Based on the experimental data, which were obtained while spreading of the investigated alloys, it was found that the presence of nickel within 1–3 % in the brazing filler metal of the Cu–Mn–Ni–Si system at a fixed concentration of manganese of 10 and silicon of lower than 2 %, leads to a decrease in spreading area (as

**Table 2.** Coefficients of influence of alloying elements on solidus and liquidus temperature of copper-based alloys (calculated data)

Alloying element <i>i</i>	$\Delta T_i^{lic}, ^\circ C$	$\Delta T_i^{sol}, ^\circ C$	$\Delta C_i, \text{ wt.}\%$	$(\Delta T/\Delta C)^{lic}$	$(\Delta T/\Delta C)^{sol}$
Mn	–62	–50	6	–10.33	–8.33
Ni	12	7	2	6	3.5
Si	–47	–81	2	–23.5	–40.5

*Note.*  $\Delta C$  is the change of concentration interval, in which a decrease in melting temperature by the value of  $\Delta T$  is observed.  $\Delta T$  is a change in the temperature range, which depends on the concentration of the constituent elements.

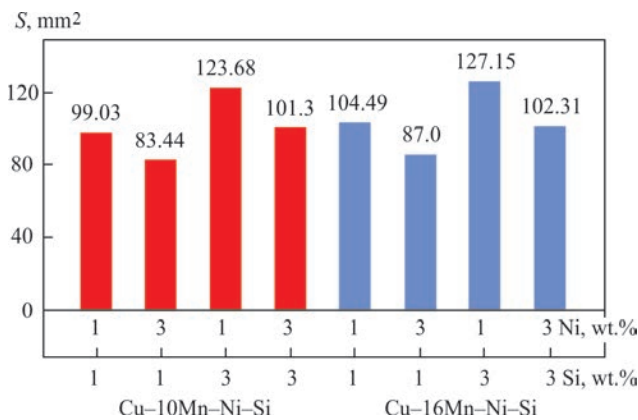


**Figure 2.** Dependence of spreading area of experimental alloys of the Cu–Mn–Ni–Si system at a fixed Mn content on the amount of Mn and Si

compared to the base one). An increase in the concentration of silicon to more than 2 % and a decrease in the nickel content contribute to an increase in the spreading area as compared to the base alloy (Figure 2).

At a concentration of manganese of 16 % and silicon of lower than 2 %, a reduction in nickel content (up to 1 %) as compared to the base one increases the spreading area, and an increase in nickel to higher than 2 %, leads to a decrease in the spreading area. In the alloys with the content of manganese of 16 % and nickel of lower than 2 % and silicon within 1–3 %, a gradual increase in the spreading area to 104.49 and 127.15 mm<sup>2</sup>, respectively, is observed. With an amount of nickel being higher than 2 %, a reduction in the silicon content as compared to base one reduces the spreading area.

The results of investigations of experimental brazing filler metals by high-temperature differential thermal analysis showed that with a manganese content of 10 % and of silicon being lower than 2 %, nickel alloying in the range of 1–3 % increases the solidus and liquidus temperature. While reducing the amount of nickel in the alloy containing 10 % of manganese and more than 2 % of silicon, a decrease in the solidus and liquidus temperature of the alloy is observed. An increase in the content of the nickel increases the solidus temperature (Figure 3, *a*).

In the alloy containing 16 % of manganese and lower than 2 % of silicon, alloying by nickel contrib-

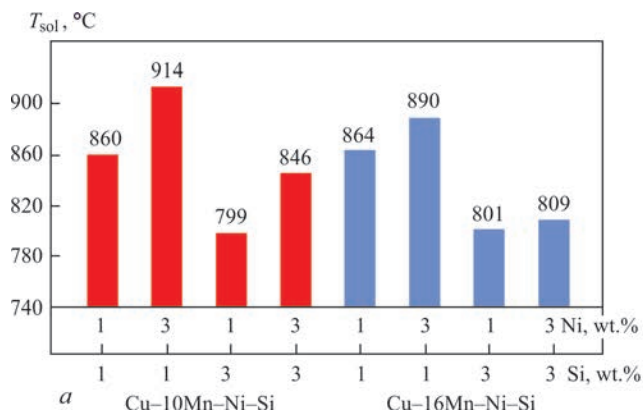


**Figure 3.** Dependence of solidus (*a*) and liquidus (*b*) temperature of experimental alloys of the Cu–Mn–Ni–Si system on content of manganese, nickel and silicon

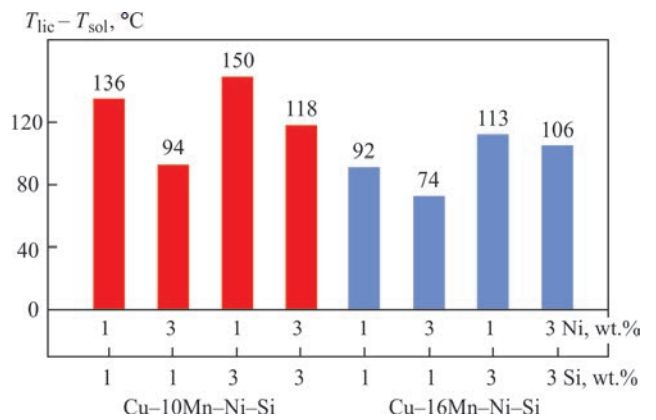


**Figure 4.** Dependence of temperature interval of melting experimental alloys of the Cu–Mn–Ni–Si system on content of manganese, nickel and silicon

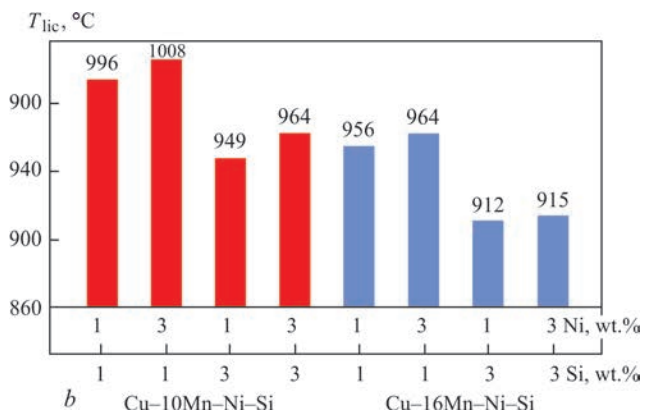
utes to an increase in the solidus temperature. The liquidus temperature also grows, but slightly (Figure 3, *b*). Doping of the alloy by silicon (up to 3 %), containing an increased concentration of nickel (up to 3 %) contributes to reduction in the solidus and liquidus temperature (Figure 3, *a, b*).

It is known that the temperature interval of melting is the difference between the solidus and liquidus temperature of the alloy. From the obtained results of investigations, it follows that at the concentration of manganese of 10 % and silicon being lower than 2 %, alloying by nickel reduces the crystallization interval as compared to the base alloy.

The content of silicon being higher than 2 % and a decrease in the amount of nickel lead to an increase in the temperature interval of melting as compared to the base values, whereas an increase in the nickel content reduces it (Figure 4).

Nickel doping within 1–3 % of the alloy of the Cu–Mn–Ni–Si system containing 16 % of manganese and less than 2 % of silicon leads to a decrease in the temperature interval of melting, which is also observed in the alloys, containing more than 2 % of silicon.

Based on the obtained results of experimental investigations, the optimal components of brazing filler metals with an acceptable temperature interval were selected, which were used in plasma brazing. Structur-



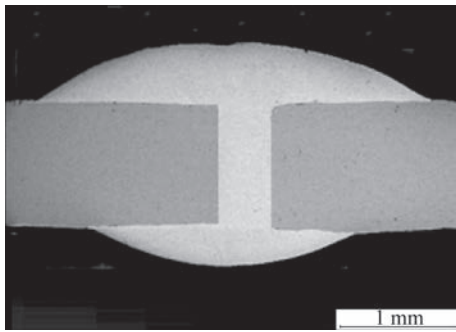


**Figure 5.** Brazed joint of steel 08kp, produced in plasma brazing. All investigations of brazed joints showed a high-quality formation of dense defect-free welds while using the brazing filler metal Cu–16Mn–1Ni–3Si ( $T_{lic} = 912\text{ °C}$ ) (Figure 5).

### Conclusions

Applying the calculation method, the coefficients of influence of alloying elements on the solidus and liquidus temperature in the alloys of the Cu–Mn–Ni–Si system were determined, which show that at a set change in the concentration interval of alloying elements, a decrease in the solidus and liquidus temperature is more strongly influenced by a silicon content with a coefficient of  $-40.5$  for solidus temperature and  $-23.5$  for liquidus one. The amount of manganese affects a decrease in the solidus and liquidus temperature to a lower extent, which is indicated by lower values of the coefficients:  $-8.3$  and  $-10.33$  (for solidus and liquidus temperature, respectively).

It was experimentally proved that alloying with nickel within the range of 1–3 % of the alloy of the Cu–Mn–Si system, which contains a fixed amount of manganese of 10 %, silicon of lower than 2 %, leads to a decrease in the spreading area (to 99.03–83.44 mm<sup>2</sup>) and an increase in the solidus temperature to 860–914 °C and the liquidus one to 996–1008 °C as compared to the base alloy. At an increase in the concentration of silicon to 3 %, a decrease in the content of nickel promotes an increase in the spreading area to 123.68 mm<sup>2</sup> as compared to the base alloy.

The results of experimental studies show that an increase in the nickel content at a manganese concentration of 10 % and that of silicon being lower than 2 % reduces the melting temperature interval from 136 to 94 °C as compared to the base one. Reducing the amount of nickel in the alloy with an increased concentration of silicon (more than 2 %) increases the of melting temperature interval to 150 °C as compared to the similar indices of the base alloy.

Nickel doping of the alloy containing 16 % of manganese and less than 2 % of silicon reduces the temperature interval of crystallization to 74–92 °C as compared to the base values. At an increased concentration of silicon, alloying with nickel leads to an increase in the melting interval to 106–113 °C.

On the basis of a comprehensive evaluation of empirical data, the concentration limits of alloying elements were selected, wt.%: 10–16 Mn, 1–3 Ni, 1–3 Si, which provide an acceptable solidus and liquidus temperature of the brazing filler metal on the base of copper and high-quality formation of brazed joints from steel 08kp.

1. Frigs, A., Stockel, S. (2012) Vollmechanisches Metall-Inert gas hartloten von feuerverzinktem Feinblech aus Stahl. *Schweißen und Schneiden*, **12**, 624–629.
2. Chovet, C., Guiheux, S. (2006) Possibilities offered by MIG and TIG brazing of galvanized ultra-high strength steel for automotive applications. *La Metallurgia Italiana*, **7–8**, 47–53.
3. Kim, Y., Park, K. (2016) A review of arc brazing process and its application in automotive institute for advanced engineering. Robot Center, Yongin, Republic of Korea, Sungbok Kwak Duckyang Ind. Co., Ltd., R&D Center, Suwon, Republic of Korea. *Int. J. of Mechanical Engineering and Robotics Research*, **5(4)**, 246–250.
4. Matusiak, J., Wycislik, J. (2015) Influence of shielding gas on fume and gas emission during arc weld brazing of steel sheets with coatings. *Shielding Gas on Fumeing Arc Weld Brazing of Steel Sheets with Coatings. Metalurgija*, **54**, 71–74.
5. Wook-Je Cho, Tae-Jin Yoon, Sung-Yun Kwak et al. (2017) Effects of brazing current on mechanical properties of gas metal arc brazed joint of 1000 MPa grade DP steel. *J. of Welding and Joining*, **35(2)**, 23–29.
6. Norbert Knopp, Mündersbach, Robert Killing, Solingen (2005) Brazing of galvanised sheets using an arc-reliable and economically viable. *Welding and Cutting*, **4(6)**, 7–9.
7. Belkacem Bouaifi (2003) Low-heat process enhances joining of coated sheet metals. *Welding J.*, **1**, 26–30.
8. Knopp, N., Killing, R. (2004) Hartlöten verzinkter Feinbleche mit dem Lichtbogen sicher und wirtschaftlich (Teil 2). *Der Praktiker*, **1**, 8–12 [in German].
9. Maksymova, S.V., Zvolinsky, I.V., Yurkiv, V.V. et al. (2020) Residual stresses in thin-sheet galvanized steel joint after arc welding and plasma brazing. *The Paton Welding J.*, **9**, 31–35. DOI: <https://doi.org/10.37434/tpwj2020.09.05>.
10. Knopp, N., Killing, R. (2003) Hartloten verzinkter Feinbleche mit dem Lichtbogen – sicher und wirtschaftlich (Teil 1). *Der Praktiker*, **12**, 366–371 [in German].
11. Ashmarin, I.P., Vasiliev, N.N., Ambrosov, V.A. (1975) *Fast statistical methods and experimental design*. Izd.-vo Leningrad. Un-ta [in Russian].
12. Lyakishev, N.P. (1997) *Constitutional diagrams of binary metal systems: Refer. Book*, 3 Vol., Vol. 2. Moscow, Mashinostroenie [in Russian].
13. Massalski, T.B., Okamoto, H., Subramanian, P.R., Kacprzak, L. (1990) Binary alloy phase diagrams. The materials information society. *ASM Int.*, **1**.
14. *Application of the process of plasma and plasma+TIG welding*. <https://www.svartools.ru/technology/primenenieprotses-sa-plazmennoy-i-plazmennoy-tig-varki> [in Russian].
15. Bronshtejn, I.N., Semendyaev, K.A. (1986) *Mathematics handbook*. Moscow, Nauka [in Russian].
16. Ivanchenko, V.G., Oshkaderov, S.P., Severina, S.N. (2012) Determination of optimum compositions of complex solid solution hardened alloys based on nickel-chrome for orthopedic dentistry. *Metallofizika i Novejshie Tekhnologii*, **34(8)**, 1133–1143 [in Russian].

Received 28.04.2021

## NUMERICAL MODELING OF STRESS-STRAIN STATE OF ELEMENTS MANUFACTURED BY 3D PRINTING

I.K. Senchenkov<sup>1</sup>, M.V. Iurzhenko<sup>2</sup>, O.P. Chervinko<sup>1</sup>, O.P. Masiuchok<sup>2</sup> and M.G. Korab<sup>2</sup>

<sup>1</sup>S.P. Tymoshenko Institute of Mechanics of the NAS of Ukraine  
3 Nesterov Str., 02000, Kyiv, Ukraine

<sup>2</sup>E.O. Paton Electric Welding Institute of the NAS of Ukraine  
11 Kazymyr Malevych Str., 03150, Kyiv, Ukraine. E-mail: office@paton.kiev.ua

Manufacture of parts by the method of 3D printing, in particular, applying FDM (Fusing Deposition Modeling) technology, is a promising trend in many branches of mechanical engineering, architecture, construction, medicine, etc. This range of problems challenges three main directions of studies: FDM 3D printing technology, materials science and mathematical modeling of processes for evaluation of functional qualities, in particular, strength of products. This work is devoted to the third direction: evaluation of stress-strain state of products manufactured by 3D printing using FDM technology. The paper considers three stages of solving this problem: 1 — mathematical formulation of the problem, which includes universal balance relations, determining equations of mechanical behaviour of the material; 2 — method of numerical solution of the problem; 3 — solving specific problems in order to determine patterns of thermomechanical processes and provide recommendations for technological settings of 3D printing. 10 Ref., 12 Figures.

*Keywords:* additive technologies, FDM 3D printing, mathematical modeling, stress-strain state

Modeling by the method of layer-by-layer surfacing or FDM 3D printing with polymer materials due to its versatility, simplicity, multifunctional capabilities and affordability is considered to be the most common 3D printing technology in the world, based on which millions of 3D printers — from the cheapest to industrial three-dimensional printing systems are operating [1, 2]. To create products by FDM 3D printing, a polymer material is used in the form of a thread (filament) from different thermoplastic materials that are supplied in coils. There may be two standard diameters of a filament: 1.75 and 3.0 mm depending on the printer specification [3].

As in all 3D printing technologies, the first step on the way of manufacturing a physical object is building

its digital 3D model [4] in special programs (Autodesk 3DsMAX, ZBrush, Maya, Blender, SolidWorks, etc.), which in the STL format is transmitted to the software of a 3D printer. Before launching the printing process, the necessary 3D printing settings (speed, temperature, etc.) are selected and the model in the slicer-program is automatically divided into horizontal layers to calculate the ways for movement of the extruder (printing head) — a device equipped with a mechanical drive for feeding a filament, a heating element for its fusion and a die, through which the extrusion is directly carried out — pushing out of the fused polymer material to the surface of a product (Figure 1, a).

At the same stage, if necessary, supporting structures are generated if overhanging elements are pres-

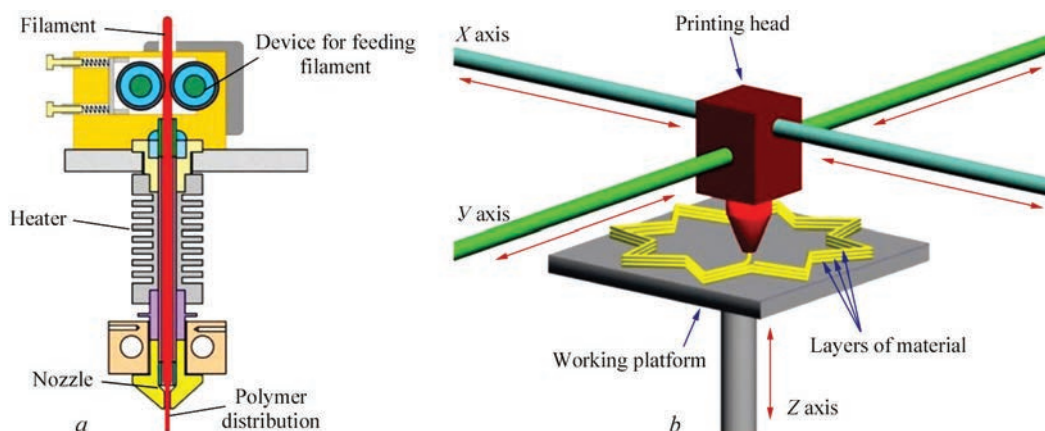


**Figure 1.** Schemes of the extruder of FDM 3D printer (a) and the process of creating a three-dimensional model by it (b) [5]

M.V. Iurzhenko — <http://orcid.org/0000-0002-5535-731X>, O.P. Masiuchok — <https://orcid.org/0000-0002-3302-3079>  
M.G. Korab — <https://orcid.org/0000-0001-8030-1468>

© I.K. Senchenkov, M.V. Iurzhenko, O.P. Chervinko, O.P. Masiuchok and M.G. Korab, 2021

ent in the model. When the preparatory part is completed, the control code (G-Code) is generated for the 3D printer based on digital data and selected settings. Further, a filament from the coil is unwound to be introduced into the extruder and a process of 3D printing itself is launched: the extruder fuses a filament and feeds a polymer material with a high precision by thin layers to a working surface of the 3D printer according to the printing algorithm and a digital 3D model.

After deposition of a layer, a polymer material is cooled and getting solid, and the platform, on which an object is formed, lowers to the level equal to the thickness of the deposited layer. The movement in three planes of the head and platform (Figure 1, *b*) is set by the algorithm developed in advance with the help of special software. When the process of building a product is completed, auxiliary structures are removed (manually or dissolved in a special solution), and a finished product can be used in a printed form or exposed to any method of further treatment.

For evaluation of the strength of parts, information on current and residual stresses, as well as distortion, especially for thin-walled elements plays an important role. Therefore, the development of methods for mathematical modeling of processes and evaluation of the mentioned settings is an actual issue in this range of problems.

**Problem formulation.** In this work, a simplified thermoelastic formulation of the problem is used. This model does not take into account the relaxation effect and provides the upper evaluation of current and residual stresses [6]. A more precise formulation that takes into account viscoelastic properties of the material, structural transformations (crystallization) in the material, as well as their influence on physical and mechanical properties of the material, will be considered in the next publications.

**Balance equations.** Element building is considered in the rectangular coordinate system. Material is considered to be isotropic. The initial formulation of the problem in an invariant form includes kinematic relations, equation of thermal conductivity

$$c_v \dot{\theta} = \text{div}(k \text{grad} \theta) + Q, \quad (1.1)$$

of quasi-static equilibrium

$$\text{div} \underline{\sigma} = 0, \quad (1.2)$$

boundary and initial conditions  $\theta = \theta_0$  at  $t = 0$ ;  $-k \vec{n} \cdot \text{grad} \theta = -q + \gamma(\theta - \theta C)$

$$\underline{\sigma} \vec{n} = 0, \quad (1.3)$$

where  $\theta$  is the temperature;  $\underline{\sigma}$  is the tensor of stresses;  $Q$  is the power of a volumetric heat source;  $q$  is the set heat flow;  $c_v$  and  $k$  are the coefficients of heat capac-

ity and heat conductivity;  $\gamma$  is the coefficient of heat transfer;  $\theta_m$  is the temperature of surrounding medium;  $\theta_0$  is the initial temperature;  $\vec{n}$  is the external normal to the body surface;  $\underline{\sigma} = \sigma_{ij}, i, j = x, y, z; i, j = x, y, z$ .

Further, these equations will be modified taking into account the process of building.

For 2D state strained in the plane  $Oxy$ , we have

$$\sigma_{zz} = \sigma_{zx} = \sigma_{yz} = 0, u_i = u_i(x, y), \varepsilon_{ij} = \varepsilon_{ij}(x, y), \\ \sigma_{ij} = \sigma_{ij}(x, y), \theta = \theta(x, y).$$

Thermomechanical behaviour of the material is described with the help of the following relations

$$\underline{\varepsilon} = \underline{\varepsilon}^e + \underline{\varepsilon}^\theta; \quad \underline{\varepsilon}^\theta = \alpha(\theta - \theta_0) \underline{I}; \quad (1.4)$$

$$\underline{s} = 2G\underline{\varepsilon}, \quad \text{tr} \underline{\sigma} = 3K_v \text{tr}(\underline{\varepsilon} - \underline{\varepsilon}^\theta), \quad (1.5)$$

here  $\underline{\varepsilon}^e$  and  $\underline{\varepsilon}^\theta$  are elastic and thermal components of deformation;  $s$  and  $\underline{\varepsilon}$  are deviators of stress tensors and deformations;  $G$  and  $K_v$  are shear and bulk modulus;  $\text{tr}$  is the trace of tensor;  $\underline{I}$  is a single tensor.

**Model of building bodies.** Let us consider the modification of relations (1.4), (1.5), taking into account the process of building [7–9]. Let us assume that the problem is solved by the finite elements method. Let the building process is controllable, i.e., the rate of building and final body configuration are known. The simplest variant of the solution algorithm is as follows. A building body configuration is covered by the fixed CE-mesh. CE-mesh covers both the body to be built in the original configuration, as well as all layers to be built in the future. Therefore, the mesh (number of nodes) does not change in the process of numerical modeling. Another approach consists in the fact that the mesh is increased as a result of attachment of building elements. In the area occupied by a source body, the properties are determined by the body material. Initially, to the elements being built, the properties of the «cavity» material are attributed, which is considered to be thermoelastic with the following characteristics

$$E \approx 0, \nu \approx 0, \alpha = \alpha_f,$$

where  $E$  is the Young's modulus;  $\nu$  is the Poisson's ratio;  $\alpha_f$  is the coefficient of linear thermal expansion of a building material. The thermophysical properties of the «cavity» are accepted the same as in a building material. Therefore, the element is «empty» only in terms of mechanics. In the process of filling, which is considered as a process developing in time, «empty» elements of the CE-mesh will be filled with a building material. It is important to keep in mind that in the process of filling the elements (building), the whole CE-mesh is deformed, which covers both the source body as well as «empty» elements adjacent to the body.

Let at the time of filling  $t^*$ , some empty element  $\Delta V(t^*)$  of the mesh has a deformation  $\underline{\varepsilon}_{ij}^*$  and let it be

filled with a material having a temperature  $\theta^*$ . It is assumed that the material of the building elements up to the contact with the surface of the body is unstrained:

$$\sigma_{xx} = \sigma_{yy} = \sigma_{zz} = \sigma_{xy} = \sigma_{yz} = \sigma_{xz} = 0 \text{ at } t = t^*. \quad (1.6)$$

In the frames of this model of building, there is a filling of an element having a preliminary deformation  $\varepsilon_{ij}^*$ , a building material with a temperature  $\theta^*$ . Thus, the conditions (1.6) mean that

$$\sigma_{ij}(\varepsilon_{kl}^*, \theta^*) = 0 \text{ in } \Delta V(t^*). \quad (1.7)$$

In order to that the determining equations of a building material (1.5) meet the condition (1.7), it is necessary and enough to modify the equation (1.5) as follows:

$$\begin{aligned} \underline{s} &= 2G_f(\underline{e} - \underline{e}^*), \\ tr \underline{\sigma} &= 3K_f tr(\underline{\varepsilon} - \underline{\varepsilon}^* - \alpha_f(\theta - \theta^*)\underline{I}). \end{aligned} \quad (1.8)$$

Here the lower index  $f$  shows that the settings relate to the material of the building volume. Therefore, in order to meet the condition of building (1.6), all the elements being built should have the determining equations,  $\underline{\varepsilon}^*$  individualized by those specific values of deformation and temperature  $\theta^*$ , at which their filling occurred. Therefore, the state  $(\varepsilon_{ij}^*, \theta^*)$  for these elements can be interpreted as «own», as far as it does not cause stresses.

**Problem formulation for building bodies.** Taking into account the results mentioned in the preceding paragraph, the mathematical problem includes the following relations:

- equations of equilibrium (1.2) and thermal conductivity of (1.1)
- determining equations for base material

$$\varepsilon_{ij} = \varepsilon_{ij}^e + \varepsilon_{ij}^\theta; \quad (1.9)$$

$$s_{ij} = 2Ge_{ij}, \quad \sigma_{kk} = 3K_V(\varepsilon_{kk} - \varepsilon_{kk}^\theta); \quad (1.10)$$

- determining equations for material being built in a component form

$$\begin{aligned} s_{ij} &= 2G(e_{ij} - e_{ij}^*), \\ \sigma_{kk} &= 3K_f(\varepsilon_{kk} - \varepsilon_{kk}^\theta - \varepsilon_{kk}^*), \end{aligned} \quad (1.11)$$

where  $G$  and  $K$  are the shear and bulk moduluses;  $Q$  is the heat source;  $\lambda$  and  $c_v$  are the coefficients of thermal conductivity and bulk heat capacity

$$\varepsilon_{ij}^\theta = \alpha(\theta - \theta_r)\delta_{ij}; \quad \varepsilon_{ij}^{\theta^*} = \alpha(\theta - \theta^*)\delta_{ij}, \quad (1.12)$$

here  $\theta$  is the current temperature;  $\theta_r$  is some reference temperature;  $\alpha$  is the coefficient of linear thermal expansion.

**Numerical method of problem solution.** *Variational formulation of the problem.* The three-dimensional problem of the thermomechanical state of building parts is solved numerically using the finite element method [9]. Lagrange variational formulation of the problem in the Cartesian system of  $Oxyz$  coordinates has the following form

$$\begin{aligned} \delta I &= \int_F \left[ \lambda \left( \frac{\partial \theta}{\partial x} \delta \left( \frac{\partial \theta}{\partial x} \right) + \frac{\partial \theta}{\partial y} \delta \left( \frac{\partial \theta}{\partial y} \right) + \frac{\partial \theta}{\partial z} \delta \left( \frac{\partial \theta}{\partial z} \right) \right) + \right. \\ &\quad \left. + (c_v \dot{\theta} - Q) \delta \theta \right] dx dy dz + \\ &\quad + \int_S (-q + \gamma(\theta - \theta_c)) \delta \theta ds = 0; \end{aligned} \quad (2.1)$$

$$\begin{aligned} \delta \Phi &= \int_F \left( \sigma_{xx} \delta \varepsilon_{xx} + \sigma_{yy} \delta \varepsilon_{yy} + \sigma_{zz} \delta \varepsilon_{zz} + 2\sigma_{xy} \varepsilon_{xy} + \right. \\ &\quad \left. + 2\sigma_{yz} \varepsilon_{yz} + 2\sigma_{zx} \varepsilon_{zx} \right) - \\ &\quad - \int_S \left( t_{nx} \delta u_x + t_{ny} \delta u_y + t_{nz} \delta u_z \right) ds = 0, \end{aligned} \quad (2.2)$$

wherein  $\delta I$  is the variation of the functional for the problem of thermal conductivity;  $\delta \Phi$  is the variation of the functional for the problem of mechanical equilibrium;  $t_{nr}$  and  $t_{nz}$  are the components of stress vector on the contour;  $u_r$ ,  $u_z$  are the radial and axial components of the movement vector;  $V$  and  $S$  are the volume and surface of the body.

The equation of thermal conductivity is integrated by time using an implicit scheme. In this case, the linearization of the problem is achieved due to the fact that the characteristics dependent on the temperature are calculated for the previous time step. The distribution of temperature calculated for the time is used to solve the problem of mechanics. From the condition of the stationarity of the functional  $\delta \Phi = 0$  (2.2), we obtain the system of algebraic equations for the movements in the nodal points. At the same time, the temperature included in the functional is taken by a constant element and does not vary. Based on the found nodal displacements, the deformations and stresses are calculated at the integration points, which are then averaged by a finite element method.

From the condition of the stationary functional  $\delta I = 0$  to determine the nodal values of the temperature  $\theta_i$ , we obtain a system of linear differential equations of the first order in time. The accuracy of the calculation depends on the number of finite elements. The required density of mesh of elements is determined by comparing the solutions of the problem at a different number of finite elements.

**Object of investigation.** The configuration of a building element is shown in Figure 2.

The sizes of the element:  $a = 6$  mm,  $b = 2$  mm,  $h = 0-50$  mm,  $\Delta h = 0.14-0.42$  mm.

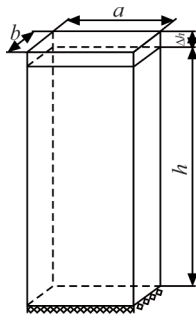


Figure 2. Building element

Let us assume that one layer  $\Delta h = 0.14$  mm is built for 1.1 s (from the calculation: the rate of building of element  $0.14 \times 0.14$  mm is 80 mm/s, i.e. the building time for one layer is 0.14 mm, at the end it is 1.1 s). Next we will consider three cases of building: by layers of 0.14 mm for 1.1 s per a layer, 360 layers; 0.28 mm for 2.2 s per a layer, 180 layers; 0.42 mm for 3.2 s per a layer, 120 layers, i.e. the rate of building (increase in height) in these three cases is the same.

On the lower surface the following conditions of fixing are set:  $u_y = 0, \sigma_{xy} = 0, y = 0$ .

**Thermomechanical properties of the material.**

The material of the object is a PLA polymer with temperature-dependent properties.

The dependence of the specific heat capacity on temperature is shown in Figure 3.

The dependence of the Young's modulus of elasticity on temperature, taken from [10], is shown in Figure 4. Other settings are  $\rho = 1210$  kg/m<sup>3</sup> is the density,  $\nu = 0.35$  is the Poisson's ratio,  $\alpha = 41 \cdot 10^{-6}$  K<sup>-1</sup> is the coefficient of thermal expansion,  $\lambda = 0.13$  W/m<sup>2</sup>·K are the coefficients of thermal conductivity. On free surfaces a heat exchange with an ambient temperature of  $\theta_m = 20$  °C with a heat transfer coefficient  $\gamma = 30$  W/m<sup>2</sup>·K occurs.

During building, the base temperature is maintained at 50 °C. Building occurs by fusion the material at 200 °C.

**Results of calculations.** Figure 5 shows the division of the area on finite elements at  $\Delta h = 0.28$  mm. Here the resulting division is shown when all the layers are already built.

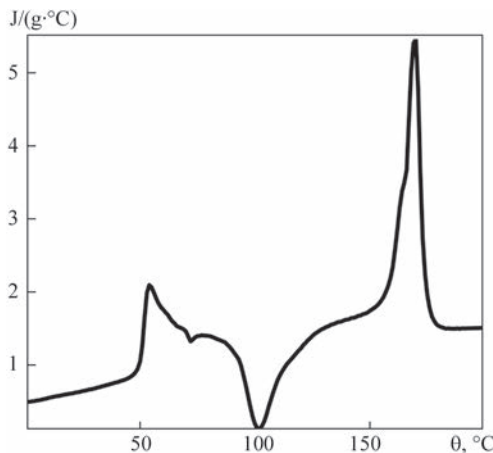


Figure 3. Dependence of specific heat capacity on temperature

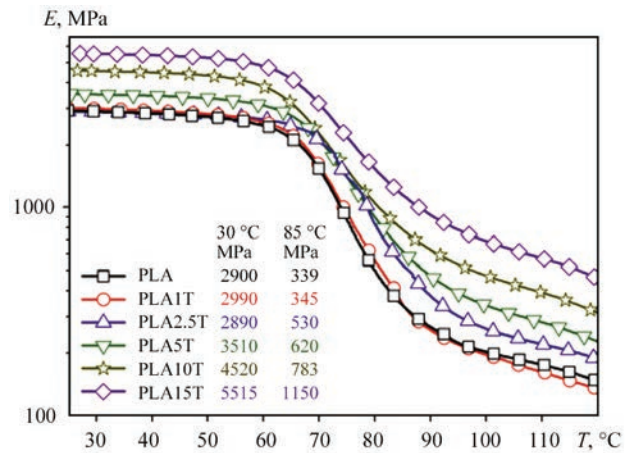


Figure 4. Dependence of the Young modulus of elasticity  $E$  on temperature

Figure 6 shows the isolines of the temperature distribution at different moments of building (Figure 6, a, b) and at the moment of cooling (Figure 6, c).

Figure 7 shows the variation in temperature over time at the points 1, 2 and 3, shown in Figure 5. Points 1 and 2 appear at the moment when the 90<sup>th</sup> layer is built. The point 3 corresponds to the highest point of the element at different moments of time.

Figure 8 shows similar curves for the stress  $\sigma_{yy}$  at the points 1 and 2.

Let us note that residual stresses in the thermoelastic problem are formed as a result of applying a heated layer on the already cooled previously deposited layer. The classic problem is mounting a heated bushing on the shaft (hot press fit), when residual compressive stresses can occur without plastic deformations.

It is seen that the residual stress distribution is formed at the temperature change from 80 °C to 50 °C. This is associated with the temperature depen-

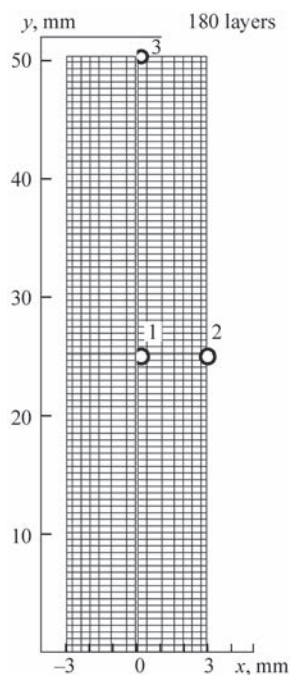
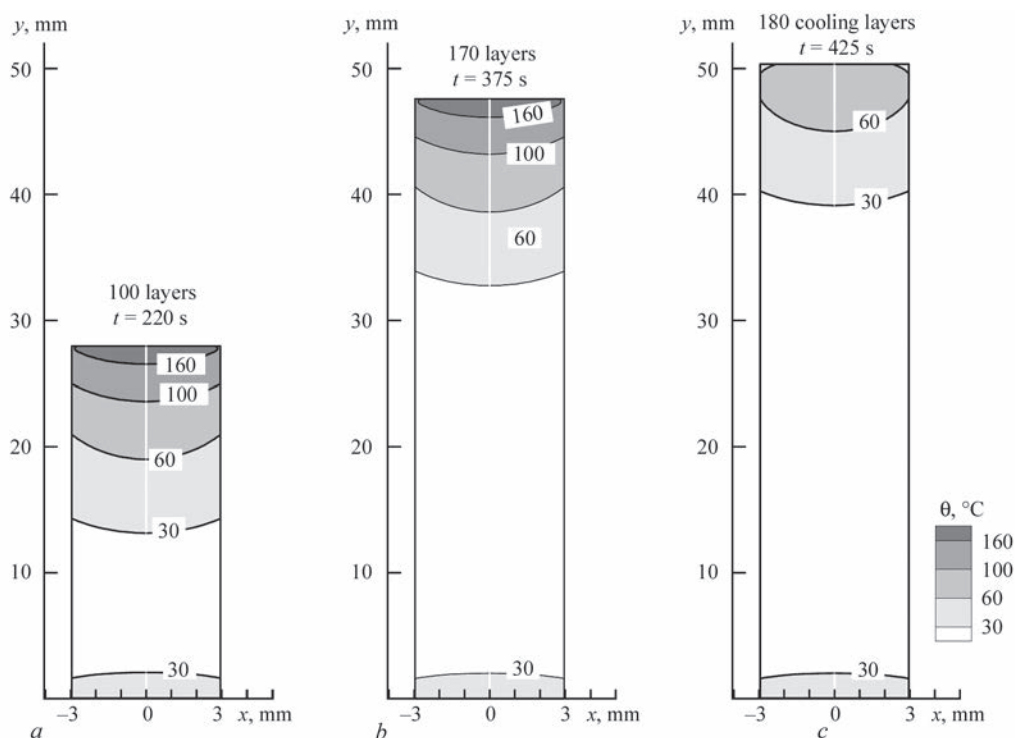


Figure 5. Division of area on finite elements



**Figure 6.** Isotherms of temperature distribution  $\theta$  at different moments of building

dence of the Young's modulus (see Figure 4). In this temperature range an increase in the rigidity of the material is observed.

Figure 9 shows the isotherms of the residual distribution of  $\sigma_{yy}$  in the  $Oxy$  plane.

Let us study the influence of the thickness of building layer of the material on residual stresses. Let us consider three cases.

1. Building with layers of 0.14 mm. The results of the calculation are shown in Figure 10. Figure 10, *b* shows changes of  $\sigma_{yy}$  in the scale of the layers.

2. Building with layers of 0.28 mm. The results of the calculation are shown in Figure 11.

3. Building with layers of 0.42 mm. The results of the calculation are shown in Figure 12.

It is seen that the level of  $\sigma_{yy}$  stresses is decreased with an increase in thickness of a building layer (Figures 10, *a*; 11, *a*; 12, *a*). The smaller the thickness of building, the higher the average stress level, whereas

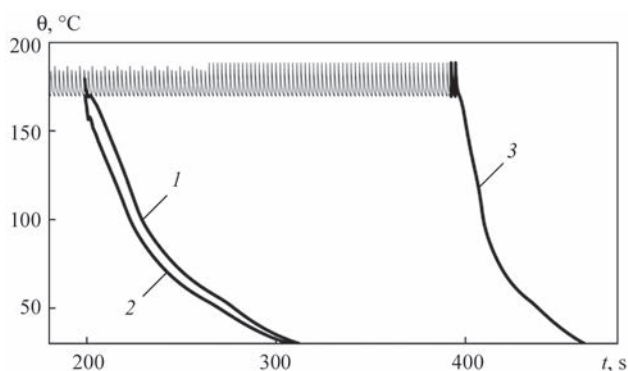


**Figure 7.** Temperature change over time at the points 1, 2 and 3

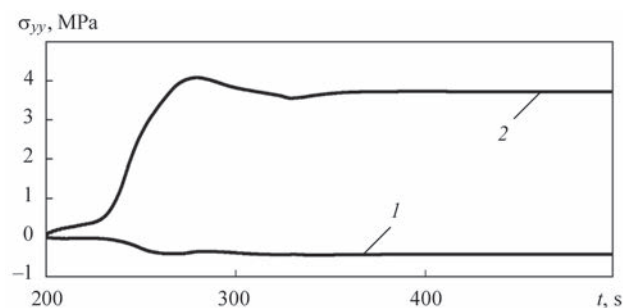


**Figure 8.** Change in  $\sigma_{yy}$  stress over time at the points 1 and 2

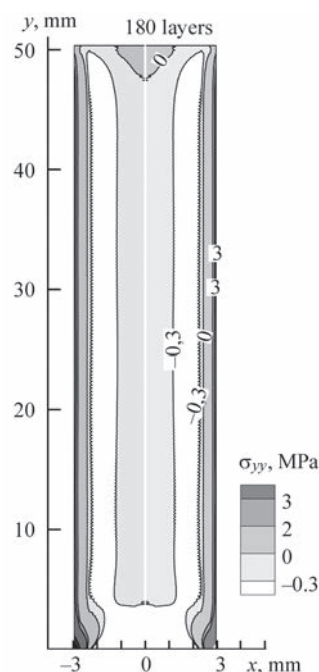


**Figure 9.** Residual distribution of longitudinal stress

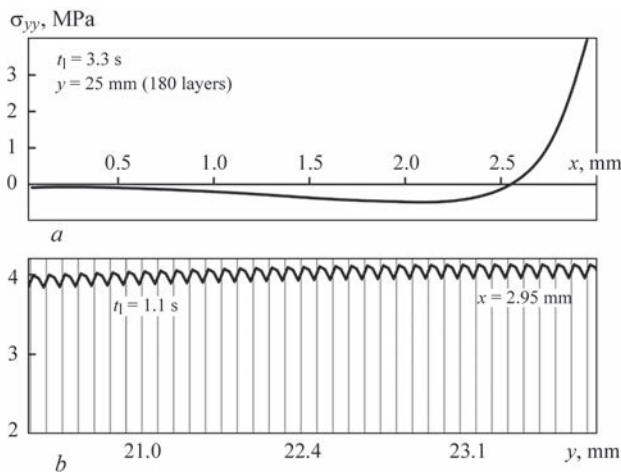


**Figure 10.** Building by layers of 0.14 mm, 360 layers: *a* —  $\sigma_{yy}$  in the cross-section  $y = 0.02$  m; *b* — in the cross-section  $x = 0$ , along the axis  $y$

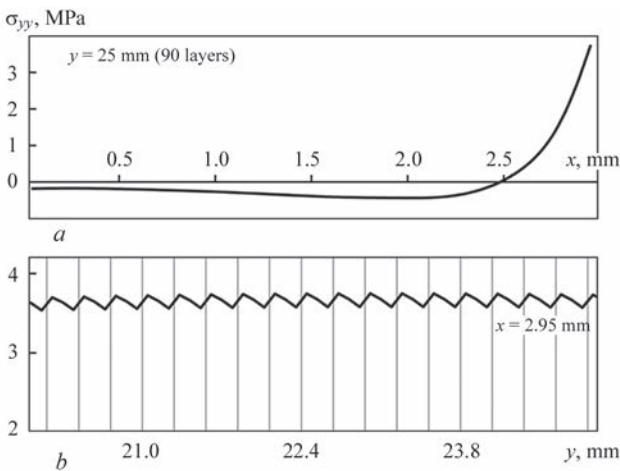


**Figure 11.** Building by layers of 0.28 mm,  $t = 2.2$  s, 180 layers: *a* —  $\sigma_{yy}$  in the cross-section  $y = 0.02$  m; *b* — in the cross-section  $x = 0$ , along the axis  $y$

the variations within the boundaries of the built layer differ insignificantly (Figures 10, *b*; 11, *b*; 12, *b*).

## Conclusions

1. In this work, a thermoelastic model of the stress-strain state of elements, manufactured by the method of additive molding by FDM 3D printing technology was developed. Namely, this is a model of multilayer building of bodies based on the theory of building bodies. Moreover, a finite element method by calculation of the thermoelastic state of layered objects was proposed.

2. The results of carried out investigations and calculations of the current and residual thermomechanical state of a particular building plate element at different moments of building and at the moment of cooling indicate that the residual stress distribution is formed by changing the temperature from 80 to 50 °C, which is associated with the temperature dependence of the

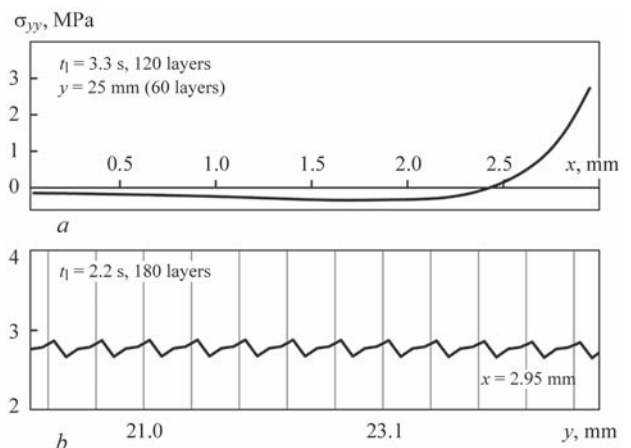


**Figure 12.** Building by layers of 0.42 mm,  $t = 3.3$  s: *a* —  $\sigma_{yy}$  in the cross-section  $y = 0.02$  m; *b* — in the cross-section  $x = 0$ , along the axis  $y$

Young's modulus of the test material and an increase in its rigidity in the specified temperature range.

3. Evaluation of the influence of the thickness of a building layer of the material (0.14; 0.28; 0.42 mm) on the residual stress state of the elements showed that the level of  $\sigma_{yy}$  stresses decreases with an increase in the thickness of a building layer.

- (2016) *Additive Manufacturing and 3D Printing State of the Industry*. Annual Worldwide Progress Report. Wohler's Associates, Inc.
- Masiuchok, O.P., Iurzhenko, M.V., Kolisnyk, R.V., Korab, M.H. (2020) Additive technologies of polymer materials (Review). *The Paton Welding J.*, **5**, 53–60. DOI: <https://doi.org/10.37434/as2020.05.08>
- Turner, B.N., Strong, R., Gold, S.A. (2014) A review of melt extrusion additive manufacturing processes. Pt I: Process design and modeling. *Rapid Prototyping J.*, **20**(3), 192–204.
- Wong, K., Hernandez, A. (2012) *A Review of Additive Manufacturing*, International Scholarly Research Network (ISRN). Mechanical Engineering. <https://doi.org/10.5402/2012/208760>.
- 3D-printing for «dummies» or what is 3D-printer*. [http://3dtoday.ru/wiki/3dprint\\_basics/](http://3dtoday.ru/wiki/3dprint_basics/) [in Russian].
- Sapronov, O.O., Buketov, A.V., Marushchak, P.O. et al. (2019) Research of crack initiation and propagation under loading for providing impact resilience of protective coating. *Functional Materials*, **26**(1), 114–120. DOI: <https://doi.org/10.15407/fm26.01.114>.
- Arutyunyan, N.Kh., Drozdov, A.D., Naumov, V.E. (1987) *Mechanics of growing viscoelastoplastic bodies*. Moscow, Nauka [in Russian].
- Senchenkov, I.K. (2005) Thermomechanical model of growing cylindrical bodies from physically nonlinear materials. *Prikl. Mekhanika*, **41**(9), 118–126 [in Russian].
- Motovilovecz, I.A., Kozlov, I.I., (1987) *Mechanics of associated fields in materials and elements of structures*. In: 5 Vol. Vol.1: Thermoelasticity. Kiev, Naukova Dumka [in Russian].
- Battegazzore, D., Bocchini, S., Frache, A. (2011) Crystallization kinetics of poly(lactic acid)-talc composites. *EXPRESS Polymer Letters*, **10**(5), 849–858.

Received 11.06.2021

# STRUCTURE AND MECHANICAL PROPERTIES OF 2219-T87 ALUMINIUM ALLOY JOINTS PRODUCED BY FLASH BUTT WELDING

**S.I. Kuchuk-Yatsenko, K.V. Hushchyn, I.V. Ziakhor,  
S.M. Samotryasov, M.S. Zavertannyi and A.M. Levchuk**  
E.O. Paton Electric Welding Institute of the NAS of Ukraine

11 Kazymyr Malevych Str., 03150, Kyiv, Ukraine. E-mail: [office@paton.kiev.ua](mailto:office@paton.kiev.ua)

During designing and manufacture of aircraft structures from modern thermomechanically strengthened aluminium alloys, there is a problem of producing welded joints with satisfactory mechanical properties without post heat treatment of large-sized products. In the work the formation of joints of thermomechanically strengthened 2219-T87 alloy during flash butt welding was investigated. It was found that a low-temperature resistance heating in combination with a short-term heating by flashing provide the formation of defect-free welded joints. Metallographic examinations showed that joints are formed through a thin layer of melt, which is a necessary condition for a high-quality welding of aluminium alloys. The influence of intense plastic deformation during upsetting with a forced formation on the morphology of  $\theta$ -phase ( $\text{CuAl}_2$ ) particles was studied. A decrease in the values of hardness in the joint area as a result of dissolution and coagulation of a strengthening  $\theta'$ -phase was established. The strength of welded joints both along and across the rolled metal lines amounts to 76 % of the strength of the base metal. 20 Ref., 2 Tables, 7 Figures.

*Keywords:* 2219 aluminium alloy, flash butt welding, welded joint, mechanical properties

In the design of space and aircraft engineering, thermally strengthened aluminium alloys of the Al–Cu system are widely used [1]. 2219 alloy and its analogue 1201 alloy have been successfully used for structural elements operating at low temperatures, in particular for the manufacture of fuel tanks and load-carrying structural elements of the rockets Saturn V, Apollo, Space Shuttle, Ariane V and «Buran» [2].

To achieve the maximum level of strength, the workpieces of 2219 alloy are delivered in a thermomechanically strengthened state T87, which is achieved by heat treatment on a solid solution by deformation strengthening and a subsequent artificial ageing [3–6].

In the manufacture of products for aircraft and space engineering from 2219 alloy, different methods of welding (electron beam [7], argon arc with consumable [8–10] and nonconsumable electrode [11, 12], friction stir (FSW) [12–18] and flash butt welding [19, 20]) are used, which differ in the thermal cycle and the level of reduction of the mechanical properties of the metal in the heat-affected zone (HAZ). For example, the joints of 2219-T87 alloy, made by argon arc welding with consumable and nonconsumable electrode and FSW, have a tensile strength of 0.6–0.65 from the level of the base metal values [8–18], which is predetermined by a full dissolution

of particles of nanosized strengthening  $\theta'$ -phase in the weld and the HAZ.

In addition, the thermal cycle of welding products of 2219 alloy can reduce the corrosion resistance of the joints as a result of coagulation (coarsening) of  $\theta$ -phase particles ( $\text{SiAl}_2$ ) in the near-weld zone. The problem of reducing indices of mechanical properties and characteristics of corrosion resistance of welds as a result of liquation in the fusion zone while using the methods of fusion welding was studied in [7–12] and while using FSW in [13–18].

In particular, in [8–12] it was found that during argon arc welding of 2219 alloy with a nonconsumable electrode, in the near-weld zone, a eutectic reaction between the particles of  $\theta$ -phase ( $\text{CuAl}_2$ ) and  $\alpha$ -matrix of the alloy:  $\alpha + \theta \rightarrow L_E$  with the formation of liquid phase  $L_E$  at the eutectic temperature  $T_E = 548^\circ\text{C}$  and higher occurs. Liquation around the large  $\theta$ -particles leads to an increase in their size and the formation of the  $\alpha$ -matrix of the alloy areas with a lower copper concentration. Liquation of copper at grain boundaries leads to the appearance of a split eutectic, which consists of bands with a high concentration of Cu (up to 33 at.%) and adjacent areas of the  $\alpha$ -phase with a low content of Cu, which causes a decrease in the corrosion resistance and mechanical properties of welds

S.I. Kuchuk-Yatsenko — <https://orcid.org/0000-0002-1166-0253>, K.V. Hushchyn — <https://orcid.org/0000-0003-3298-4537>,  
I.V. Ziakhor — <https://orcid.org/0000-0001-7780-0688>, S.M. Samotryasov — <https://orcid.org/0000-0003-4891-9625>,  
M.S. Zavertannyi — <https://orcid.org/0000-0002-8415-8555>, A.M. Levchuk — <https://orcid.org/0000-0002-0361-7394>

© S.I. Kuchuk-Yatsenko, K.V. Hushchyn, I.V. Ziakhor, S.M. Samotryasov, M.S. Zavertannyi and A.M. Levchuk, 2021

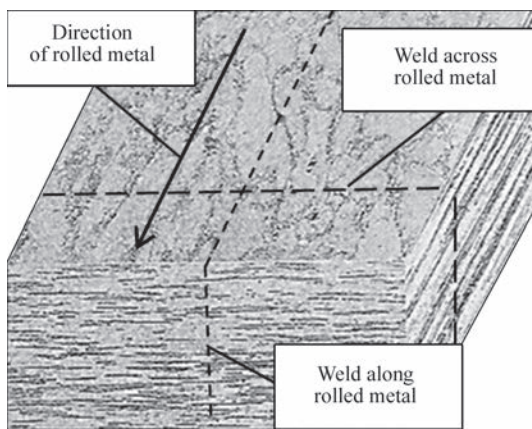


**Figure 1.** Scheme of rolled metal lines in the specimens of 2219-T87 alloy during FBW

[8–10]. The similar problems occur also during FSW of 2219 alloy [13–15].

Heat treatment (hardening and ageing) of products from 2219 alloy after welding allows a significant restoration of the structure and mechanical properties of the welds, but in the production of large-sized structures, such a task can hardly be realized. Therefore, the urgent problem is the development of technologies for welding of 2219 alloy, which provide a higher level of strength of joints without a post heat treatment, which will meet the technical requirements of space engineering developers.

An effective technology for the manufacture of load-carrying aircraft elements (stringers, shells, frame rings) from extruded profiles of developed and compact cross-section is flash butt welding (FBW). This method provides a high stable quality of joints, unites assembly and welding operations in a single cycle, does not demand application of consumables [19, 20]. In welding of billets of up to 12 mm thickness, the FBW technology provides high indices of strength of aluminium alloys at an insignificant width of the HAZ.

In FBW of profiles of a larger thickness it is necessary to carry out resistance preheating of billets, which causes an increase in width of HAZ and, probably, emergence of the problems characteristic of methods of fusion welding and FSW.

The aim of the work consisted in establishing the features of the formation of joints at FBW of thick-walled extruded profiles of 2219-T87 alloy, the study of their microstructure and determination of mechanical properties.

**Procedure of works.** The investigations were carried out on the specimens of 2219-T87 alloy of a

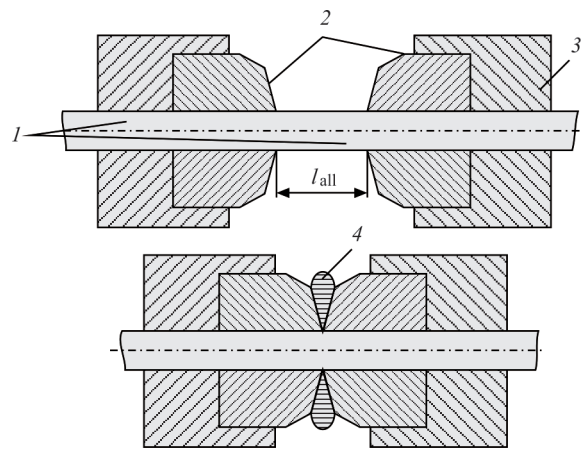


**Figure 2.** Scheme of FBW with the joint formation: 1 — parts; 2 — forming devices; 3 — current conductor; 4 — extruded metal;  $l_{all}$  — allowance for welding

rectangular section with 15 mm thickness and 60 mm width. The length of the specimens was not less than 200 mm. The chemical composition of the studied alloy is given in Table 1.

Since anisotropy of the structure and mechanical properties is characteristic for pressed profiles from aluminium alloys, the experiments on FBW of the specimens of 2219-T87 alloy were carried out at different direction of the rolled metal lines (Figure 1), which represent the clusters of  $\theta$ -phase particles. During welding of billets with a longitudinal arrangement of rolled metal fibers, the joint is formed in a plane perpendicular to the direction of rolled metal fibers (further, weld across the rolled metal). During welding of billets with a transverse arrangement of rolled metal fibers, the joints are formed in a plane parallel to the direction of rolled metal fibers (further, weld along the rolled metal).

Experimental welding was carried out in a laboratory flash butt welding machine K607, equipped with a welding transformer with a capacity of 75 kV·A and an upsetting drive with a force of up to 1000 kN. The FBW process included several stages: resistance preheating, flashing and upsetting. Deformation during upsetting occurs in the conditions of volume compression with the help of forming devices (Figure 2).

The parameters of the FBW process were established within the ranges: flashing voltage  $U_{2fl} = 5-6$  V, flashing rate  $V_{fl} = 2-18$  mm/s, upsetting rate  $V_{ups} \geq 200$  mm/s. The total allowance for flashing and upsetting is  $l_{all} = 60$  mm.

Macrostructure of welded joints was evaluated by visual inspection using the magnification glass Levenhuk Zeno Multi ML7 at a magnification

**Table 1.** Chemical composition (wt.%) of 2219 alloy [4, 5]

Al	Cu	Mn	Mg	Si	Zr	V	Zn	Fe	Ti
Base	5.8–6.8	0.2–0.4	<0.2	<0.2	0.1–0.25	0.05–0.15	<0.1	<0.3	0.02–0.1

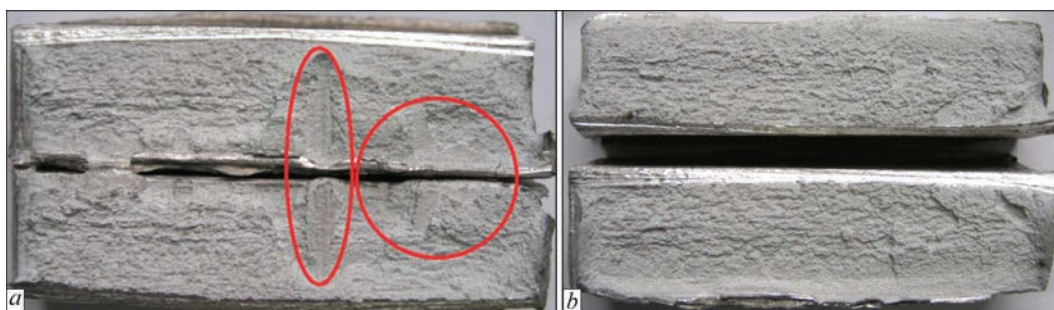


**Figure 3.** Fractures of welded joints: *a* — with defects (oxide films); *b* — without visible defects

of  $\times 3$ – $10$ . Metallographic examinations were performed with the use of an optical microscope Neophot-32 at a magnification of  $\times 25$ ,  $\times 100$  and  $\times 400$ . The preparation of the surface of macrosections was carried out in a grinding-polishing machine Struers LaboPol-5. To reveal the structure, Keller reagent ( $0.5\text{HF}-1.8\text{HCl}-2.7\text{HNO}_3-95\text{H}_2\text{O}$  (vol.%) and a 5 % aqueous solution of hydrofluoric acid were used. The study of the distribution of hardness *HRB* in the joint zone was carried out using a stationary hardness meter Novotest TS-BPR at a load of 600 N (ball diameter is  $1/16''$ ) with a step of 1–2 mm. Mechanical tensile tests of specimens of welded joints were carried out in the TsDM-10 machine with a maximum force of 100 kN.

**Results of investigations.** During welding, preheating resistance to  $200\text{ }^\circ\text{C}$  was used, the current of is  $I_{2pr} = 20\text{ kA}$ . Heating to this temperature does not lead to a

loss of the strength of 2219-T87 alloy. Further increase in the temperature of a preheating results in an increase in the width of the zone in which the complete dissolution and coagulation of the nanosized strengthening  $\theta'$ -phase in the FBW process is observed, that causes a decrease in the strength of the alloy.

In the process of testing the welding modes, an «express analysis» of the quality of welded joints — bending of specimens with a notch along the joint line until fracture was performed. The quality of the joints was evaluated by the presence (absence) of defects such as oxide films during visual inspection of fractures of the destroyed specimen (Figure 3, *a*). When testing the FBW modes, we tried to minimize the time of welding in order to reduce the width of the HAZ joints of 2219-T87 alloy.

According to such procedure, the FBW modes were determined, that provide the absence of defects (Fig-

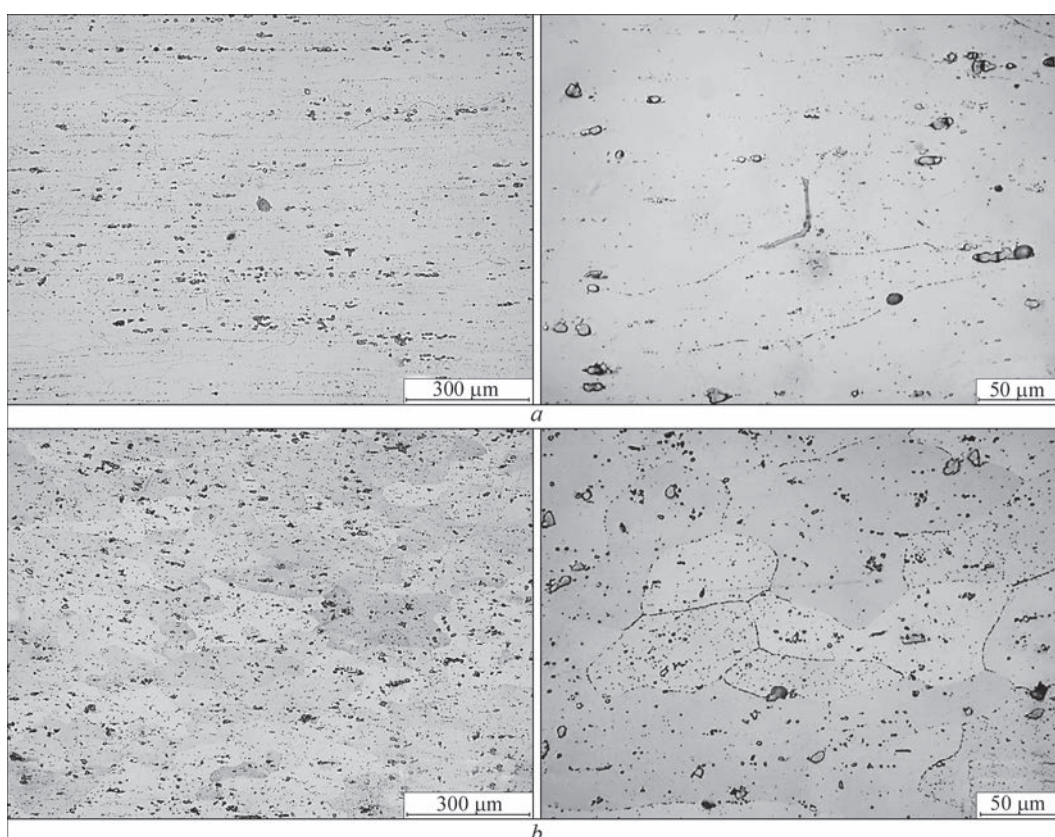


**Figure 4.** Microstructure of base metal of 2219-T87 alloy along (*a*) and across (*b*) the rolled metal

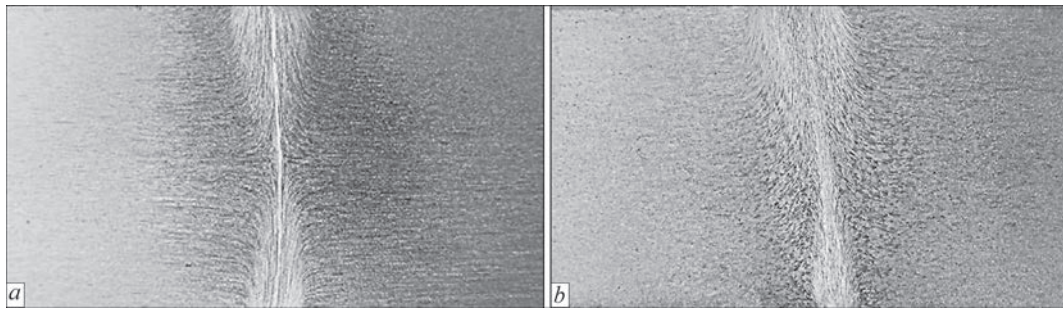


**Figure 5.** Structure of welded joint of specimens of 2219-T87 alloy: thickness  $\delta = 15$  mm: *a* — weld across the rolled metal; *b* — weld along the rolled metal

ure 3, *b*) along the joint line. It was established that a low-temperature resistance heating to 200 °C with a subsequent flashing during 15 s and deformation at the value of upsetting pressure not lower than 500 MPa provide the formation of high-quality joints. After obtaining positive results, batches of specimens were welded for metallographic examinations and mechanical tests.

The results of examinations of the microstructure of the base metal (BM) and welded joints (WJ) made by FBW are shown in Figures 4–6. The base metal of 2219-T87 alloy (Figure 4) is characterized by a pronounced texture with the grains deformed in the direction of the rolled metal and a large number of  $\theta'$ -phase particles ( $\text{CuAl}_2$ ) of different sizes, arranged in

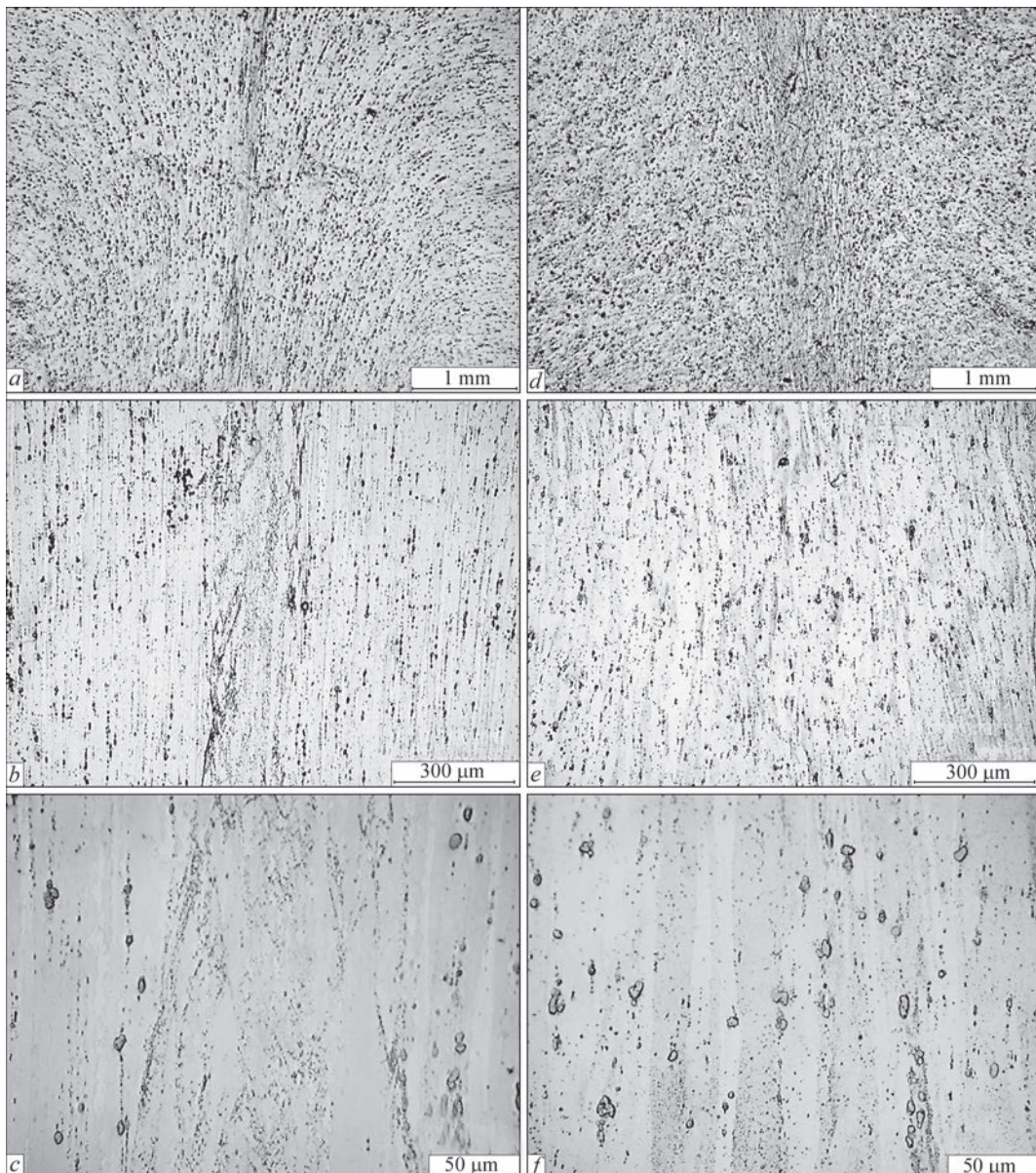


**Figure 6.** Microstructure of welded joint of 2219-T87 alloy of weld across (*a–c*) and along the rolled metal (*d–f*)

**Table 2.** Mechanical properties of base metal and welded joints of 2219-T87 alloy depending on the direction of the rolled metal

Specimen	$\sigma_t$ , MPa	$\sigma_{0.2}$ , MPa	$\delta_{5\%}$ , %	Bending angle $\alpha^\circ$	KCV, J/cm <sup>2</sup> ( $T = 20^\circ\text{C}$ )	Strength coefficient $\sigma_{t\text{WJ}}/\sigma_{t\text{BM}}$
Weld across the rolled metal						
BM	486	413	10.9	37	13.9	—
WJ	372	263	4.3	33	16.6	0.76
Weld along the rolled metal						
BM	486	410	8.0	21	6.9	—
WJ	372	249	5.0	31	20.5	0.76

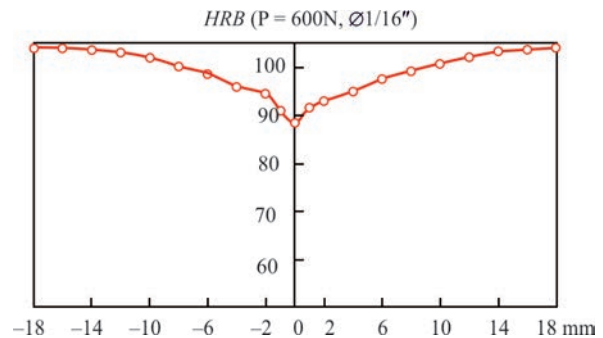
the form of «chains», the largest particles have a size of 10–15  $\mu\text{m}$ .

Approaching the joint line, a change in the orientation of the grains is observed, and the direction of rolled metal fibers in the zone of thermomechanical effect (ZTME) gradually changes to  $90^\circ$  as compared to the initial direction of BM grains and coincides with the direction of metal extrusion during upsetting deformation (Figure 6). As a result of metal extrusion into the gap between the forming devices, the  $\theta$ -phase precipitations are partially dissolved in ZTME — their size decreases, clusters in the form of «chains» are partially destroyed, the particles become separated. Such structure indicates a significant effect of intense plastic deformation during upsetting with a forced formation (extrusion) on the morphology of secondary phase precipitates.

In the welded joint both across (Figure 6, *a-c*) as well as along the rolled metal (Figure 6, *d-f*), such defects as oxide films, delaminations and eutectic formations are absent. In HAZ coarsening of  $\theta$ -phase particles ( $\text{CuAl}_2$ ) and the emergence of a split eutectic are not observed, which is characteristic for the methods of fusion welding [7–12] and FSW [13–18] of 2219 alloy.

The size of the  $\theta$ -phase particles in the center of the butt (joint area with a width of 150–200  $\mu\text{m}$ ) is 1–2  $\mu\text{m}$ , which is much smaller than that for BM of the alloy, and indicates the complete dissolution of the particles during welding and their repeated precipitation in a more dispersed form during cooling. Analysis of the microstructure (Figure 6) shows the formation of the joint through a thin layer of melt, which is a necessary condition for a high-quality welding of aluminium alloys.

Analysis of the hardness distribution in the joint zone of 2219-T87 alloy (Figure 7) shows that the width of the HAZ is about 28 mm. The decrease in hardness values is predetermined by structural transformations in the joint zone of 2219-T87 alloy under the influence of the FBW thermal cycle, namely by the dissolution and coagulation of nanosized strengthening of the  $\theta'$ -phase.

**Figure 7.** Hardness distribution in the welded joint zone of 15 mm thick specimens from 2219-T87 alloy

The results of tensile tests of BM of 2219-T87 alloy and welded joints are given in Table 2. Therefore, the tensile strength  $\sigma_t$  of the welded joints of the plates with a thickness of 15 mm from 2219-T87 alloy, produced by FBW, is 76 % of the strength values of the BM alloy both with the arrangement of the weld along and across the rolled metal.

## Conclusions

1. It was established that a resistance preheating of specimens of 2219-T87 alloy to a temperature of  $200^\circ\text{C}$  and conducting FBW with a forced formation under pressure value at an upsetting of not lower than 500 MPa, provide the formation of high-quality (defect-free) joints.

2. The microstructure of the metal in ZTME of the joint of 2219-T87 alloy indicates a significant effect of intense plastic deformation during upsetting with a forced formation on the morphology of  $\theta$ -phase particles ( $\text{CuAl}_2$ ). As a result of extrusion of the metal in a gap between the forming devices, a partial dissolution of the  $\theta$ -phase particles occurs — their size decreases, clusters in the form of «chains» are partially destroyed.

3. The size of the  $\theta$ -phase particles in the center of the joint zone with a width of 150–200  $\mu\text{m}$  is 1–2  $\mu\text{m}$ , which is predetermined by the complete dissolution of the  $\theta$ -phase during welding and a repeated precipitation into a more dispersed form during cooling. Such a transformation of  $\text{CuAl}_2$  particles indicates the formation of a joint through a thin layer of the

melt, which is a necessary condition for a high-quality welding of aluminium alloys.

4. The ultimate strength of the joints of 15 mm thick plates of 2219-T87 alloy, produced by the developed FBW technology, amounts to 76 % of the base metal of the alloy, both with the arrangement of the weld along and across the rolled metal. The decrease in hardness values in the joint zone is predetermined by the dissolution and coagulation of nanosized strengthening  $\theta'$ -phase.

- Gureeva, M.A., Grushko, O.E. (2009) Aluminium alloys in welded structures of modern transport vehicles. *Mashinostroenie i Inzhenernoe Obrazovanie*, **3**, 27–41 [in Russian].
- Setyukov, O.A. (2013) 1201 aluminium alloy in structure of spacecraft «Buran». *Aviats. Materialy i Tekhnologii*, Special Issue, 15–18 [in Russian].
- Federal aviation administration flight standards service (2018) *Aviation Maintenance Technician Handbook*. [https://www.faa.gov/regulations\\_policies/handbooks\\_manuals/aircraft](https://www.faa.gov/regulations_policies/handbooks_manuals/aircraft).
- ASTM International – Standards Worldwide (2014) *ASTM B209M – 14 Standard Specification for Aluminium and Aluminium-Alloy Sheet and Plate (Metric)*. <https://www.astm.org/Standards/B209M.htm>
- George, E., Totten, G.E. (2003) *Handbook of aluminium*. Vol. 1: Physical metallurgy and processes. Marcel Dekker Inc. New York, NY, USA.
- An, L.H., Cai, Y., Liu, W. et al. (2012) Effect of pre-deformation on microstructure and mechanical properties of 2219 aluminium alloy sheet by thermomechanical treatment. *Transact. Nonferr. Met. Soc. China.*, **22**, 370–375. DOI: [https://doi.org/10.1016/S1003-6326\(12\)61733-6](https://doi.org/10.1016/S1003-6326(12)61733-6).
- Lu, Y., Wang, J., Li, X. et al. (2018) Effects of pre-deformation on the microstructures and corrosion behavior of 2219 aluminium alloys. *Mater. Sci. Eng. A*, **723**, 204–211. doi: 10.1016/j.msea.2018.03.041.
- Sobih, M., Elseddig, Z., Almazy, K., Sallam, M. (2016) Experimental evaluation and characterization of electron beam welding of 2219 Al-alloy. *Indian J. of Materials Sci.*, Article ID 5671532, DOI: <https://doi.org/10.1155/2016/5671532>.
- Huang, C., Kou, S. (2000) Partially melted zone in aluminium welds – liquation mechanism and directional solidification. *Weld J.*, **79**(5), 113–120.
- Huang, C., Kou, S. (2001) Partially melted zone in aluminium welds: solute segregation and mechanical behavior. *Ibid.*, **80**(1), 9–17.
- Huang, C., Kou, S. (2001) Partially melted zone in aluminium welds planar and cellular solidification. *Ibid.*, **80**(2), 46–53.
- Srinivasa, Rao, P., Sivadasan, K.G., Balasubramanian, P.K. (1996) Structure-property correlation on AA 2219 aluminium alloy weldments. *Bull. Mater. Sci.*, **19**(3), 549–557.
- Poklyatsky, A.G., Chajka, A.A., Klochkov, I.N., Yavorskaya, M.R. (2009) Strength and structure of aluminium alloy welded joints made by friction stir and nonconsumable electrode welding. *The Paton Welding J.*, **9**, 9–12.
- Venkateswarlu, D. (2017) Analysing the friction stir welded joints of AA2219 Al–Cu alloy in different heat-treated state. In: *Proc. of IOP Conf. Series: Mater. Sci. and Eng. (Hyderabad, India, 1–2 June, 2017)*. IOP Publishing. DOI: <https://doi.org/10.1088/1757-899X/330/1/012074>.
- Kang, J., Feng, Z.C., Frankel, G.S. et al. (2016) Friction stir welding of Al alloy 2219-T8: Pt I – Evolution of precipitates and formation of abnormal  $Al_2Cu$  agglomerates. *Metall. Mater. Transact. A*, **47**(9), 4553–4565. DOI: <https://doi.org/10.1007/s11661-016-3648-7>.
- Kang, J., Feng, Z.C., Li, J.C. et al. (2016) Friction stir welding of Al alloy 2219-T8: Pt II – mechanical and corrosion. *Ibid.*, **47**(9), 4566–4577. DOI: <https://doi.org/10.1007/s11661-016-3646-9>.
- Kang, J., Liang, S., Wu, A. et al. (2017) Local liquation phenomenon and its effect on mechanical properties of joint in friction stir welded 2219 Al alloy. *Acta Metall. Sin.*, **53**(3), 358–368. DOI: <https://doi.org/10.11900/0412.1961.2016.00311>.
- Rivera, O.G., Allison, P.G., Brewer, L.N. et al. (2018) Influence of texture and grain refinement on the mechanical behavior of AA2219 fabricated by high shear solid state material deposition. *Mater. Sci. Eng. A*, **724**, 547–558. DOI: <https://doi.org/10.1016/j.msea.2018.03.088>.
- Kuchuk-Yatsenko, S.I. (1992) *Flash butt welding*. Kiev, Naukova Dumka [in Russian].
- Kuchuk-Yatsenko, S.I., Chvertko, P.N., Semyonov, L.A. et al. (2010) Peculiarities of flash butt welding of high-strength aluminium alloy 2219. *The Paton Welding J.*, **3**, 9–12.

Received 05.07.2021

**SEPTEMBER 10, 1957** Plasma cutter was patented. Plasma cutting was invented in 1954 in a laboratory of Linde department of Union Carbide Company. Young scientist Robert Gage found that TIG arc passed through small diameter nozzle significantly rises its intensity and temperature. Passing through this focused arc sufficiently large gas flow, he discovered that such arc can be used for metal cutting. Arc temperature, reaching more than 24000 K, melts metal and intensive air flow blows out molten metal for cutting. Since gas in arc was in overheated state, called plasma, this process was named plasma cutting.

**SEPTEMBER 15, 2014** Huge welding installation was developed at NASA. Vertical assembly platform is a single 170 meter welding aggregate, which was called «Vertical Assembly Center» and located inside the NASA assembly center based in New Orleans. This huge welding installation is designed for welding of lift launch vehicle tank. This development allows successful welding of parts of perspective super heavy — lift launch vehicles that are planned to be used for the most different purposes among which Mars flights.



# UPE-500 COMPLEX FOR DETERMINING WELDING AND TECHNOLOGICAL CHARACTERISTICS OF COATED ELECTRODES

O.M. Kostin<sup>1</sup>, O.O. Yaros<sup>2</sup>, Y.O. Yaros<sup>2</sup> and O.V. Savenko<sup>3</sup>

<sup>1</sup>Admiral Makarov National University of Shipbuilding

9 Heroiv Ukrainy Prosp., 54025, Mykolaiv, Ukraine. E-mail: kostin.weld@gmail.com

<sup>2</sup>LLC AMITI

42 Novozavodska Str., 54028, Mykolaiv, Ukraine. E-mail: yaros.amity.mk.ua@gmail.com

<sup>3</sup>PJSC PlasmaTec

18 Maksymovycha Str., 21036, Vinnytsia, Ukraine. E-mail: alexsv62@gmail.com

The article presents the methodology of quantitative evaluation of welding-technological characteristics of coated electrodes using the UPE-500 complex, which provides a high stability of the control welding process in all spatial positions in the automatic mode. The complex is equipped with the measuring system PicoScope 4444 with the software PicoScope 6 which fix and statistically process high reliability parameters of welding process stability that provides online-control of quality of manufacturing industrial batches of electrodes. 8 Ref., 1 Table, 3 Figures.

*Keywords:* electrode, melting stability, evaluation methodology, automatic mode

The modern technology of manufacturing coated electrodes from the moment of their invention by Oscar Kelberg in 1904 have passed a complex way of improvement and provides a high-quality welding of a wide range of structural materials. The vast majority of properties of electrodes, such as mechanical characteristics of deposited metal, its chemical and structural composition, content of harmful impurities and gases, corrosion resistance, etc. are regulated and easily controlled by manufacturers according to quantitative indices. However, welding and technological characteristics of coated electrodes, that have a crucial importance in providing stability of welding process is traditionally controlled, relying on a subjective qualitative evaluation of a highly-skilled welder. This is not fully objective and needs to be improved.

Despite the fact that the scientific society actively uses quantitative indices of arc burning stability during the development of new compositions of coatings and improvement of the technology of manufacturing electrodes, manufacturers do not have serial equipment, that could evaluate welding and technological characteristics in the manufacture of industrial batches of coated electrodes according to quantitative criteria. The use of such equipment in electrode production will automatically provide a high-accuracy evaluation of the quality of electrode manufacturing, which is extremely relevant. In this regard, the Scientific-Industrial Company of the LLC «AMITI» (Mykolaiv) by order of the

PJSC «PlasmaTec» (Vinnytsia) designed and produced a laboratory complex UPE-500 (TU U 27.9-20864642-003:2021), with the help of which manufacturer can control the quality of products online. The work was carried out according to the methodological assistance of the experts of the Ukrainian Certification Committee of Welders and with the assistance of the Society of Welders of Ukraine.

**Analysis and research methodology.** The welding process stability is a complex and multifactorial concept and does not have a standardized definition. According to many authors, the most successful formulation of this physical phenomenon is the definition of Yu.M. Lankin, which he provided in the article [1]: «The process of welding, the deviation of whose parameters from average values does not exceed a set level, is called stable. The measure of stability is the deviation from a parameter of the average value. As a deviation of a parameter from the average value, its dispersion is taken, mean square deviation or variation coefficient.» Thus, the welding process stability can be controlled by quite quantitative indices.

In this regard, basic parameters of welding mode, which are traditionally used to evaluate the stability of mass transfer, is a short circuit duration of arc gap ( $\tau_{sh-c}$ , ms), cycle duration — period of formation and transfer of a drop ( $T_{sh-c}$ , ms), current value (maximum  $I_{max}$  and minimum  $I_{min}$ , A); rate of current increment ( $V_{increment}$ ,  $I_w$  and  $V_{drop}$ ,  $I_w$ , A/s) [1, 2]. In this case, for

example, in [3], as a criterion of stability, the authors propose to use mean square deviation of short-circuit duration ( $\sigma \tau_{\text{sh.-c}}$ ) and their frequency ( $\sigma T_{\text{sh.-c}}$ ) and the authors of work [2, 4] use mean square deviation of the amplitude value of current ( $\sigma I_w$ ), short-circuit current ( $\sigma I_{w \text{ max}}$ ) and variation coefficient of rate of increment of short-circuit current ( $K_v, I_{w \text{ max}}$ ).

The choice of specific parameters of the process stability depends on the type of mass transfer, as far as the mass transfer stability does imply the stability of the process. Academician B. Paton clearly described the boundary types of mass transfer as a coarse-droplet (with short circuits or without them) and foggy [5]. Each type of electrode coating is characterised by the own type of mass transfer. For example, electrodes with the main type of coating are characterized by a coarse-droplet transfer (usually with short circuits). Therefore, the criteria for stability of the process are criteria of short circuits stability (droplet transfer): dispersion and coefficient of frequency variation of short circuits or their period. Electrodes with rutile-cellulose coating are characterized by a fine-droplet and even fog-shaped transfer, during which a short circuit is an exception and can not serve as a criterion for stability of the process and vice versa — small deviations of welding current is an index of a stable fine-droplet transfer. Therefore, to evaluate the stability of the process of melting electrodes with rutile-cellulose coating, dispersion and coefficient of variation of welding current are used [4]. Therefore, the only standardized methodology for determining the stability of welding process does not exist and the choice of research methodology is based on the parameters of studying object.

First of all, it should be noted that the overwhelming majority of certified electrodes, providing metal surfacing with a low content of harmful impurities and gases, guarantee the serviceability of welded structures operating under the conditions of a dynamic limit load, especially at negative temperatures, belong to the coatings of the basic type. In this regard, the work was focused on studying stability of the welding process with the electrodes of the basic type of coating. Based on the analysis of existing publications on this occasion and preliminary studies, the following criteria for evaluation of the mass transfer process stability were selected: average frequency of short circuits (mass transfer) —  $f_{\text{av}}$ ; mean square deviation of frequency of short circuits (mass transfer) —  $\sigma$ ; coefficient of variation of frequency of short circuits (mass transfer) —  $K_{vf} = \sigma/f_{\text{av}}$ ; calculated mass of a drop, which is determined as a physically obvious ratio of the mass melting rate to the frequency of mass transfer  $m_{\text{av}} = dM/f_{\text{av}}$ .

The calculated mass of a drop is required for its comparison with a critical mass of a drop  $m_{\text{dr}}$ , which is one of the boundary criteria for evaluation of the pro-

cess stability. As a critical mass of a drop, the authors took a mass of a drop with a diameter, equal to diameter of the electrode (for example, for the electrode of 4 mm diameter  $m_{\text{dr}} = 0.26$  g). It is physically obvious, that further exceeding in the size, and, consequently, in the mass of a drop leads to its insufficient protection by slag and causes increased spattering and a complete destabilization of welding process. The data on the effect of a drop size on the stability of welding process, obtained by other authors, confirm the validity of applying this criterion [6]. The real mass of a drop will be slightly less than the calculated one, taking into account the processes of burnout, evaporation and a partial dispersion of liquid metal, which provides a safe margin to researchers. Therefore, the first condition of the process stability is the inequality  $m_{\text{av}} < m_{\text{dr}}$ .

The statistical indices of mass transfer (short circuits) characterize the stability of the process, but not fully determine the convenience and quality of welding. All previous researchers note the importance of increasing the frequency and reduction in the mass of a drop to increase the convenience and quality of welding, including the completeness of running exchange reactions [6]. Therefore, the welder in case of the same stability of the process, intuitively prefers the electrodes providing a higher frequency of mass transfer and a smaller drop size. In this regard, taking into account the fact that the average short-circuit frequency can not be absolutely objective for comparison, as far as it varies within the limits described by the coefficient of variation, in the work a new indice was for the first time introduced — critical frequency of mass transfer, which is equal to the difference of medium frequency and mean square deviation of frequency  $f_{\text{dr}} = f_{\text{av}} - \sigma$ . Mathematically, critical frequency of mass transfer corresponds to the properties of a normal distribution described by specific values of an average short circuit frequency and a mean square deviation of the short-circuit frequency and physically it determines the lower boundary of the mass transfer frequency. Moreover, 82 % of drop transition occurs with a higher frequency. Accordingly, in such circumstances, it is possible to form drops with an average maximum size  $m_{\text{max}} = dM/f_{\text{dr}}$ , which can additionally be taken into account for comparison with a critical mass of a drop  $m_{\text{dr}}$ .

The reliability of the obtained results depends in the first turn on the methods of obtaining and processing of results. In this regard, the measurement and fixation of electrical parameters, as well as their statistical characteristics were performed with the use of the measuring system PicoScope 4444 and the software PicoScope 6. During measurements, a digital frequency filter with a frequency of 40 Hz is used, built in the PicoScope 4444 [4], which eliminates the impact of 50 Hz mains. As compared to most of the measuring

systems, PicoScope 4444 is in a set with PicoScope 6 has a number of advantages. Let us consider them in detail because this determines the quality and reliability of the obtained data.

The measuring system PicoScope 4444 and the software PicoScope 6 allow determining the mean square value and the mean square deviation not only of welding current and voltage, but also frequency of mass transfer. In this case, the automatic use of amplitude-frequency analysis based on Fourier transformation does take into account the used digital frequency filter, provides a reliable automatic determination of frequency and other characteristics of the mass transfer, even at a partial or a complete lack of short circuits in the mass transfer, which is especially important for obtaining characteristics at a large arc length. In addition, automatic determination and registration of the mean arithmetic value and the mean square deviation of frequency of mass transfer allow increasing the time of process to be analyzed, which significantly increases reliability of the results. In our case, we restricted the time of automatic analysis to 50 s, that even at a frequency of 3 Hz provides 150 cycles of mass transfer. The reliability of the obtained data also increases the use of automatic processing of oscillograms. The obtained reliability of the results allows applying one of the principles of mathematical statistics in full: «If the value of the variation coefficient does not exceed 33 %, then the population is considered homogeneous, and if more than 33 %, then it is inhomogeneous». In our case: if the value of the variation coefficient of the frequency of mass transfer does not exceed 33 %, then the process is stable, and if it more than 33 %, then it is unstable. Therefore, the second condition of the process stability is the inequality  $K_{\nu} < 33 \%$ .

In order to realize all the advantages of the mentioned methodology, the integrated evaluation of welding and technological characteristics of coated electrodes was constructed and the laboratory UPE-500 complex was manufactured, which corresponds to the needs of modern production of welding consumables.

**Laboratory UPE-500 complex.** The UPE-500 complex is designed to determine and optimize welding and technological characteristics of electrodes and welding wire in combination with shielding gases during welding in all spatial positions. In the work of the complex, Bi-auto principle is realized, which involves automated fixation, processing and registration of obtained data with simultaneous stabilization of welding modes, which is also performed in automatic mode. This principle of work allows obtaining authentic characteristics of stability of melting electrodes without a subjective intervention of operator.

The complex allows welding with the use of different power sources both of direct as well as alternating current. It is strictly forbidden to use welding



Figure 1. Appearance of manipulator

power sources with oscillators, stabilizers or other pulsed high-voltage devices for arc stabilization. The complex consists of three parts: control panel with the port for connecting personal computer, measurement and switching unit with the possibility of connecting oscilloscope and directly manipulator. Appearance of the manipulator is shown in Figure 1.

The manipulator provides movements of welding tool across and along the weld and the electrode feed in the automatic mode typical for welder during welding with a coated electrode. In this case, the function of dynamic regulation of its feed rates with a feedback stabilizes the arc voltage, which fixes its length with a high accuracy. The complex also provides a digital fixation of parameters and video records of welding process. In addition, the complex is connected to the central server of the enterprise, which provides the online control of the quality of electrode manufacturing. All the received information is archived, which makes it possible to have a data bank for further statistical analysis in order to determine the optimal ways of improving the electrode production.

#### Basic performance characteristics of the UPE-500 complex:

Dimensions of the workplace:

length, mm	450
width, mm	400
height, mm	400

Feed of coated electrode in welding zone with a smooth adjustment of welding voltage in the range, V

Movement of a product or a welding tool with a smooth rate adjustment in the range, cm/min

Smooth adjustment of movement of a welding tool across the weld: linear and circumferential movement for all spatial positions

amplitude of oscillations, mm	0–55 (0–100 %)
separately adjustable (left/right) delays	
along the edges, s	0–5 (0–100 %)
oscillation speed, cm/min	17.8–178 (0–100 %)

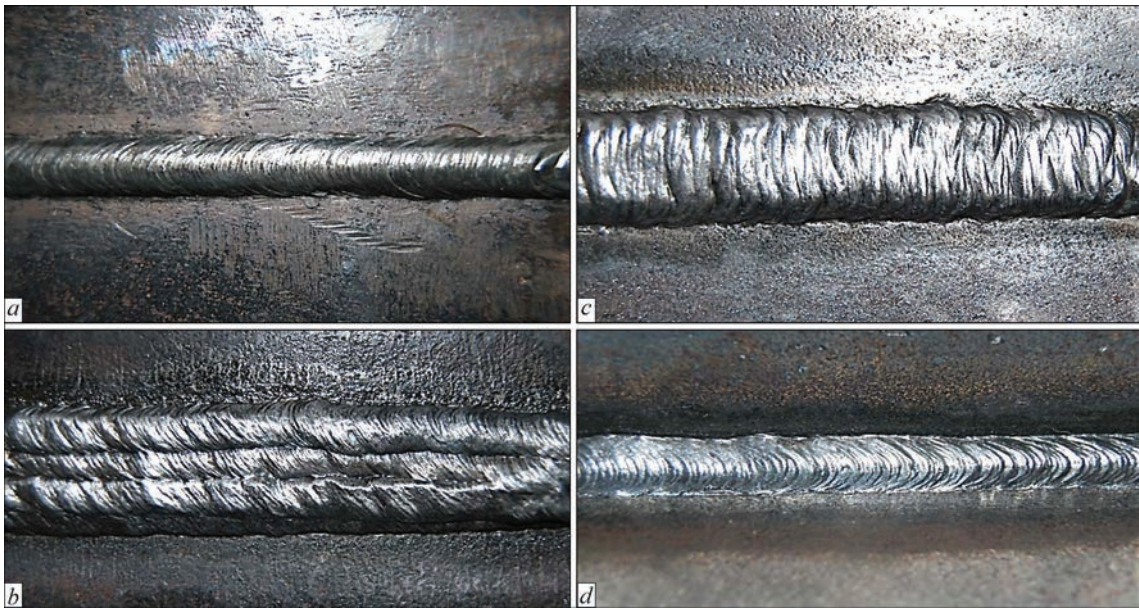


**Figure 2.** Appearance of butt (*a–c*) and fillet (*d*) welds in spatial positions: *a* — flat; *b* — horizontal; *c* — overhead; *d* — horizontal overhead

Positioning of welding tool in all spatial positions:

range of linear positioning across the weld, mm . . . . .	0–400
range of linear positioning along the vertical, mm . . . . .	0–400
range of circumferential positioning in a transverse weld plane, grad . . . . .	0–360
range of inclination in a longitudinal weld plane, deg . . . . .	0–45
maximum admissible length of electrode, mm . . . . .	500

To provide a high-quality test welding with the use of the UPE-500 complex, welding process specifications (WPS) were developed for butt and fillet welded joints, as well as for surfacing in all spatial positions. Welding process specifications are executed in accordance with the requirements of the standard DSTU EN ISO 15609-1:2019. Welding and surfacing technologies are certified in accordance with the requirements of standards DSTU EN ISO 15614-1: 2019 and DSTU EN ISO 15614-7:2019. The typical appearance of welds produced using the UPE-500 complex is shown in Figure 2.

The possibilities of the complex provide a quantitative evaluation of stability of melting electrodes that are serially produced and their automatic comparison with the reference values, which allows providing the desired quality of electrode manufacturing. In addition, the laboratory complex can be used to evaluate the effective range of parameters of welding specific grades of electrodes, arc elasticity (a recommended range of arc length in welding), effect of coating components and their condition on the stability of electrode melting, testing of new grades of electrodes to introduce them into serial production, solving the promotional issues related to the controversial evaluation of quality of electrode products by a consumer and much more accompanied by modern electrode production.

**Example of application.** The PJSC «PlasmaTec» successfully produces electrodes UONI-13/55

«PLASMA», which are in a great demand for a consumer due to a balanced relation of price to quality. One of the advantages of these electrodes relating to type E 7018 according to the AWS A5.1 standard is the presence of iron powder in coating mixture [7, 8], which increases the efficiency of their use by 20 %. In this case, the losses of metal on burnout and spattering are compensated, the cost of electrodes is reduced by 10–15 %, the deposition rate is increased by 8–10 %, weld formation and slag crust separation are improved. Traditionally, for manufacture of these electrodes at the company enterprises, a mixture of iron powders PZhrV 2.200.28 (TU 14-1-5365–98) and DIP 400 30W (EN 10204 3.1) is used. After purchasing a complex of equipment at the Company Atomising System Ltd (England), it became possible to produce the own iron powder.

To determine the influence of the method of producing and composition of iron powder on the characteristics of stability of melting electrodes UONI-13/55 «PLASMA», two batches of electrodes of 4 mm diameter were manufactured according to conventional and improved technology based on the use of powder of the own production in the equipment of the Company Atomising System Ltd. The work was preceded by large-scale studies on optimization of granulometric characteristics and chemical composition of iron powder of the own production.

The electrodes were tested in the UPE-500 complex. Welding was performed in the flat position within the requirements of the welding process specification WPS No. 111-01-20 on the following modes: welding current: 160 A, arc voltage: 24 V, welding rate: 14 cm/min. From each batch of electrodes, five pieces of electrodes were randomly selected that passed tests. Characteristic oscillograms and operating indices of

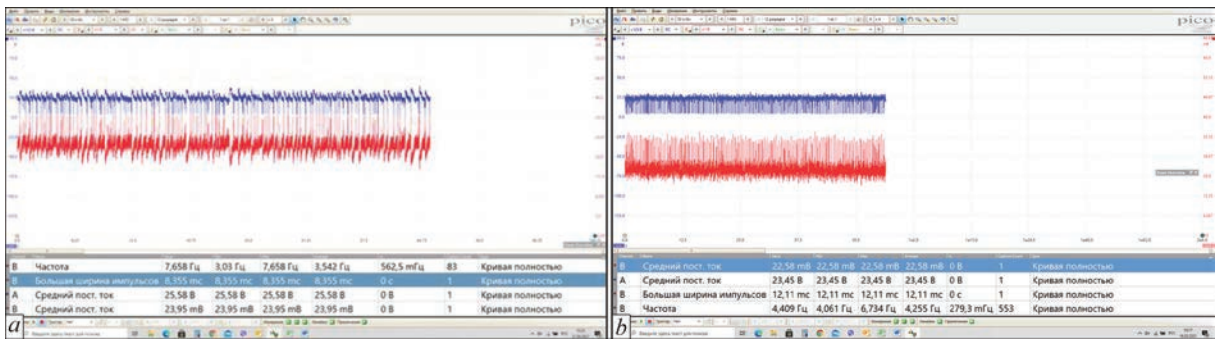


Figure 3. Oscillogram of welding process: *a* — conventional technology; *b* — improved technology

Criteria of welding process stability

Technology of electrode manufacturing	Average frequency $f_{av}$ , Hz	Critical frequency $f_{cr}$ , Hz	Coefficient of variation $K_{vp}$ , %	Average mass of drop $m_{av}$ , g	Maximum mass of drop $m_{max}$ , g
Conventional	3.7	3.53	6.2	0.161	0.168
Improved	4.14	3.92	5.3	0.148	0.156

mass transfer of welding processes using electrodes of conventional and improved manufacturing technology, calculated in the automatic mode, are shown in Figure 3. The average indices of the criteria for the stability of melting electrodes in the mentioned conditions of welding are given in Table.

The analysis of the obtained results showed that in both cases, the conditions of the process stability ( $m_{av} < m_{dr}$  and  $K_{vf} < 33\%$ ) are provided, but welding with the electrodes, containing an optimized iron powder of its own production, allows a significantly increase in the stability of the process and an increase in the frequency of mass transfer. In absolute units, the average frequency of mass transfer increased by 10.6 %, the critical frequency of mass transfer increased by 9.9 %, and the variation coefficient decreased from 6.2 to 5.3 %. Characteristically, that the average mass of drop decreased by 8.1 % and the maximum average mass of a drop (0.156 g) decreased to less than the average mass of a drop (0.161 g) for the conventional technology of manufacturing electrodes, which is a significant positive effect and provides a considerable improvement in welding-technological properties of electrodes and the quality of welding.

Therefore, the use of the UPE-500 complex unlike the qualitative standard method of evaluation in the form of a questionnaire of welder, provides a high reliability quantitative evaluation of parameters of the welding process stability.

## Conclusions

1. The methodology for evaluation of criteria of welding process stability using coated electrodes with the basic type of coating (average frequency of short circuits, mean square deviation of short circuit frequency, coefficient of variation of short circuit frequency,

calculated average mass of a drop and, in addition, critical average short circuit frequency) provides a quantitative evaluation of parameters of the welding process stability with a high reliability.

2. The UPE-500 laboratory complex performs welding in all spatial positions with a simultaneous stabilization of the process in an automatic mode and performs automatic fixation, processing and registration of received data, which provides a quantitative evaluation of welding and technological characteristics of coated electrodes without a subjective intervention of operator.

- Lankin, Yu.N. (2011) Indicators of stability of the GMAW process. *The Paton Welding J.*, **1**, 6–13.
- Pokhodnya, I.K. (1990) *Metallurgy of arc welding. Processes in arc and melting of electrodes*. Kiev, Naukova Dumka [in Russian].
- Ilyashchenko, D.P. (2017) *Influence energy parameters of inverter power sources on structure and properties of permanent joints in manual arc welding*: Syn. of Thesis for Cand. of Techn. Sci. Degree. Tomsk, RF [in Russian].
- Letyagin, I.Yu. (2010) *Development of methods of rapid evaluation of arc burning stability and repeated arc ignition in manual arc welding*: Syn. of Thesis for Cand. of Techn. Sci. Degree. Perm, PSTU [in Russian].
- (1974) *Technology of electric fusion welding of metals and alloys*. Ed. by B.E. Paton. Moscow, Mashinostroenie [in Russian].
- Zhiznyakov, S.N., Sidlin, Z.A. (2006) *Manual arc welding. Materials. Equipment. Technology*. Kiev, Ekotekhnologiya [in Russian].
- Didit Sumardiyanto, Sri Endah Susilowati (2019) Effect of welding parameters on mechanical properties of low carbon steel API 5L shielded metal arc welds. *American J. of Materials Sci.*, **9**(1), 15–21.
- Santhosh, S., Jaganathan, S., Anantha Raman, L., Balmurugan, M. (2018) Experimentation and comparative study of E6013 and E7018 weldments using shielded metal arc welding. *Int. J. of Mechanical and Production Engineering Research and Development*, **8**, 169–174.

Received 11.05.2021

# MATHEMATICAL MODELING OF HYDRODYNAMIC AND THERMAL PROCESSES AT CRYSTALLIZATION OF TITANIUM INGOTS PRODUCED BY EBM

S.V. Akhonin<sup>1</sup>, V.O. Berezos<sup>1</sup>, O.I. Bondar<sup>2</sup>, O.I. Glukhenkyi<sup>2</sup>, Yu.M. Goryslavets<sup>2</sup> and A.Yu. Severin<sup>1</sup>

<sup>1</sup>E.O. Paton Electric Welding Institute of the NAS of Ukraine

11 Kazymyr Malevych Str., 03150, Kyiv, Ukraine. E-mail: office@paton.kiev.ua

<sup>2</sup>Institute of Electrodynamics of the NAS of Ukraine

56 Peremohy Prosp., 03057, Kyiv, Ukraine. E-mail: bondar\_o\_i@ukr.net

It is shown that when specifying the efficiency of EBM process, the phenomenon of thermogravitational convection is a weighty factor, which determines the thermal state of the ingot. A mathematical model of interrelated hydrodynamic and thermal processes in the crystallizing metal, taking into account the phenomena of thermogravitational convection, was formulated for a steady-state mode of the process of electron beam melting of titanium into a straight-through cylindrical mould. The thermal state of the ingot as well as the position of the crystallization front at a continuous feeding of liquid titanium from the cold hearth into the mould depending on metal temperature at the inlet and speed of ingot drawing for a laminar mode of hydrodynamic flow in the liquid pool was determined. It is found that at increase of metal temperature at the inlet into the mould in the studied range (2040–2100 K) shifting of the point of maximum pool depth from the ingot axis becomes smaller. Calculations within the constructed mathematical model were used to study the impact of the rate of liquid metal feed from the cold hearth into the mould on the shape and depth of a liquid pool. It is found that at increase of ingot drawing rate by 30 % the liquid pool depth increases by 1.5 times, and the point of the maximum liquid pool depth becomes close to the ingot axis. 10 Ref., 1 Table, 9 Figures.

*Key words*: mathematical modeling; electron beam melting; hydrodynamic and thermal processes; ingot; titanium; continuous casting

Solidification of metal in the mould during electron beam melting (EBM) is accompanied by complex and transient physical processes of heat transfer, hydrodynamic flows and radiation. In practice, it is often impossible to measure values of the parameters in these processes, especially with a sufficient accuracy. In addition, in metallurgy, full-scale experiments are labour-consuming and involve high material costs because of a high energy consumption and cost of a melted metal. Therefore, numerical experiments with the use of methods of mathematical modeling and calculations in computers are of great importance, which allow making a qualitative and quantitative picture of the phenomena occurring in metallurgical processes at relatively low costs and a minimal amount of experimental data.

In [1, 2] the basic principles of modeling thermophysical processes in ingots produced by the methods of special electrometallurgy are formulated. Regarding the processes describing different stages of EBM, such as melting of the initial charge, mixing and evaporation of metal and impurities in the cold hearth, ingot formation in the mould, ingot cooling etc., they were considered in [3–6]. However, in the mentioned works, taking into

account the complexity of solving interrelated three-dimensional multiphysical problems and the limited available calculating resources, a mathematical modeling of thermophysical processes in producing titanium ingots was mainly reduced to considering the thermal state of the ingot without heat and mass transfer due to the movement of a melt in the mould.

The modern development of numerical methods and ever-increasing capacity of computer technologies provide a possibility of formulating more complete and complex problems of modeling technological processes and the numerical approach is the most attractive in the study of hydrodynamic processes and processes of heat and mass transfer that occur while producing ingots by EBM method. In [7], a three-dimensional mathematical model of interrelated hydrodynamic and thermal processes of metal solidification in a straight-through cylindrical mould during electron beam melting with a cold hearth was presented and considered in detail. This mathematical model allows studying the processes in the quasi-fatigue mode of continuous ingot melting, during which the position of the crystallization front of the alloy in the mould does not change over time. On the example of the ingot of titanium Ti–6Al–4V alloy, which solidi-

S.V. Akhonin — <https://orcid.org/0000-0002-7746-2946>, V.O. Berezos — <https://orcid.org/0000-0002-5026-7366>,

O.I. Bondar — <https://orcid.org/0000-0002-1678-8862>, O.I. Glukhenkyi — <https://orcid.org/0000-0001-5053-5677>,

Yu.M. Goryslavets — <https://orcid.org/0000-0003-1668-4972>, A.Yu. Severin — <https://orcid.org/0000-0003-4768-2363>

© S.V. Akhonin, V.O. Berezos, O.I. Bondar, O.I. Glukhenkyi, Yu.M. Goryslavets and A.Yu. Severin, 2021

fies in a cylindrical mould with a diameter of 0.6 m, it was shown that the effect of a turbulent thermal conductivity on the position of the crystallization front and the liquid pool depth is negligible for a set speed of ingot drawing (4 mm/min). In this case this allows making assumptions about the presence of turbulence only in the zone of inlet of the liquid metal jet from the cold hearth into the mould and about the predominant laminar nature of a melt in the liquid pool in general.

The shape and depth of a liquid pool can be more significantly affected by the overheating temperature of the liquid metal fed from the cold hearth and the efficiency of the continuous casting process. Therefore, the aim of this study is to determine the thermal state of the ingot and the position of the crystallization front at a continuous feeding of liquid titanium from the cold hearth into the mould depending on the metal temperature at the inlet and the speed of ingot drawing for a laminar hydrodynamic flows in the liquid pool. The study of these issues was carried out on the example of casting commercial titanium into a straight-through cylindrical mould of 0.4 m diameter.

For modeling the mentioned process, the following mathematical model was formulated, which includes the laws of conservation of mass (1), pulse (2) and power (3):

$$\nabla(\rho\mathbf{u}) = 0; \quad (1)$$

$$\rho(\mathbf{u} \cdot \nabla)\mathbf{u} = -\nabla p + \nabla \cdot \left( \mu(\nabla\mathbf{u} + (\nabla\mathbf{u})^T) - \frac{2}{3}\mu(\nabla \cdot \mathbf{u})\mathbf{I} \right) + \rho\mathbf{g} + \frac{C(1-F_L)^2}{q+F_L^3}(\mathbf{u} - \mathbf{u}_{\text{cast}}); \quad (2)$$

$$\rho C_p(\mathbf{u} \cdot \nabla)T = -(\nabla \cdot \mathbf{q}), \quad (3)$$

where  $\rho$  is the density;  $\mathbf{u}$  is the speed;  $p$  is the pressure;  $\mu$  is the dynamic viscosity;  $\mathbf{I}$  is a single matrix;  $\mathbf{g}$  is the gravity vector;  $C = 10^5$  and  $q = 0.01$  are the constants, the ratio of which should be sufficient to suppress the movement (except for the casting speed  $\mathbf{u}_{\text{cast}}$ ) in the solid zone;  $F_L$  is the fraction of the liquid phase (varies in the range from 0 to 1);  $\mathbf{u}_{\text{cast}}$  is the vector of speed of ingot drawing;  $C_p$  is the specific heat capacity;  $T$  is the temperature;  $\mathbf{q} = -k\nabla T$  is the heat flux due to thermal conductivity;  $k$  is the coefficient of thermal conductivity.

The position of the crystallization front was determined in accordance with the phase field method. The essence of the method consists in the fact that the phase transition occurs in a certain temperature range of  $\Delta T = T_1 - T_s$ . The liquid zone is determined by the temperature higher than the liquidus temperature  $T_1$ , the solid zone is the temperature lower than the solidus temperature  $T_s$ , and the transition zone is between

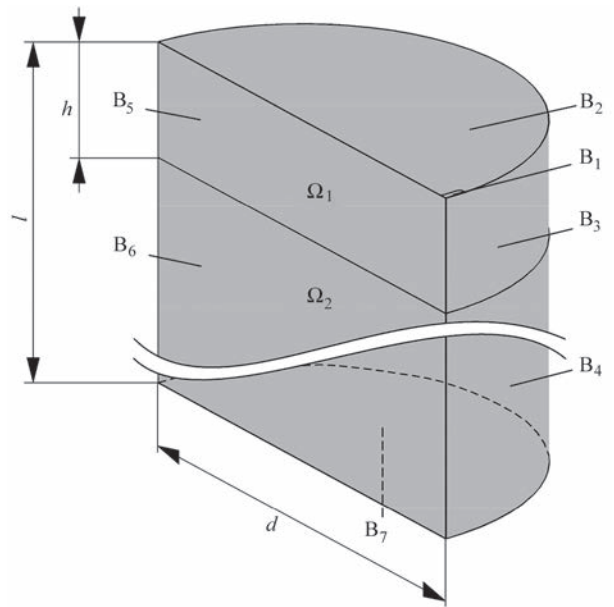


Figure 1. Calculation region for numerical modeling

them. The crystallization front is determined by the isotherm of melting temperature  $T_m = T_s + \Delta T/2$ . Expressions for determination of the fraction of a liquid phase  $F_L$  and the corresponding physical properties of materials in the transition zone (zone of phase state variation) are presented in [7].

The calculation region for studying the mentioned processes is presented in Figure 1, where  $B_1$ – $B_7$  are the borders of the calculation region,  $d = 0.4$  m,  $h = 0.15$  m,  $l = 2 \cdot d$ , the intersection of a melt jet at the inlet into the mould ( $B_1$ ) is  $10 \times 40$  mm.

The boundary conditions for the calculation region presented in Figure 1 are given in the Table, where  $\mathbf{n}$  is the vector of normal to the surface;  $u_{\text{cast}}$  is the speed of ingot drawing;  $q_{\text{ev}}$  is the thermal flux from the surface of liquid metal due to evaporation;  $\varepsilon$  is the radiation coefficient;  $h$  is the coefficient of contact heat dissipation;  $\sigma_{\text{SB}} = 5.67 \cdot 10^{-8}$  W/(m<sup>2</sup>·K<sup>4</sup>) is the Stefan–Boltzman constant;  $T_{\text{amb}} = 293.15$  K is the ambient temperature.

Physical characteristics of titanium are as follows: melting temperature  $T_m = 1941$  K; latent melting heat  $L = 295$  kJ/kg; coefficient of dynamic viscosity for the liquid zone  $\mu_l = 0.0035$  Pa·s; coefficient of dynamic viscosity for the solid zone  $\mu_s = 1$  Pa·s. Therefore, at a set temperature range of the phase transition  $\Delta T = 60$  K, liquidus temperature was  $T_1 = 1971$  K and solidus temperature was  $T_s = 1911$  K. Characteristics of the transition zone (phase transition zone) were determined according to the method of total heat capacity (apparent heat capacity formulation).

Temperature dependences of the specific heat capacity  $C_p(T)$ , coefficient of thermal conductivity  $k(T)$  and density  $\rho(T)$  for solid and liquid phases of titanium are presented in Figure 2, *a–c* respectively [8]. The depen-

Boundary conditions of calculation region for numerical modelling

Boundary	Conditions for speed	Conditions for heat flux
B <sub>1</sub>	$\mathbf{u} - (\mathbf{u} \cdot \mathbf{n})\mathbf{n} = 0$	$T = T_m$
B <sub>2</sub>	$\mathbf{u} \cdot \mathbf{n} = 0$ $\mathbf{K} - (\mathbf{K} \cdot \mathbf{n})\mathbf{n} = 0$ $\mathbf{K} = \mu(\nabla \mathbf{u} + (\nabla \mathbf{u})^T)\mathbf{n}$	$-\mathbf{n} \cdot \mathbf{q} = \varepsilon_2 \sigma (T_{\text{amb}}^4 - T^4) - q_{\text{ev}} + \frac{3P_{\text{eb}}}{\pi d^2}$ $\varepsilon_2 = 0.5$
B <sub>3</sub>		$-\mathbf{n} \cdot \mathbf{q} = \varepsilon_3 \sigma (T_{\text{amb}}^4 - T^4) + h_3 (T_{\text{amb}} - T)$ $\varepsilon_3 = 0.35(1 - F_l)$ $h_3 = h_s(1 - F_l) + h_l F_l$ $h_s = 60 \text{ W}/(\text{m}^2 \cdot \text{K})$ $h_l = 2000 \text{ W}/(\text{m}^2 \cdot \text{K})$
B <sub>4</sub>		$-\mathbf{n} \cdot \mathbf{q} = \varepsilon_4 \sigma (T_{\text{amb}}^4 - T^4)$ $\varepsilon_4 = 0.35$
B <sub>5</sub>		$-\mathbf{n} \cdot \mathbf{q} = 0$
B <sub>6</sub>		
B <sub>7</sub>	$\mathbf{u} \cdot \mathbf{n} = u_{\text{cast}}$	$-\mathbf{n} \cdot \mathbf{q} = h_7 (T_{\text{amb}} - T)$ $h_7 = 10 \text{ W}/(\text{m}^2 \cdot \text{K})$

dence of losses from the surface of liquid titanium due to evaporation of  $q_{\text{ev}}(T)$  is shown in Figure 2,  $d$  [9].

During calculations, as basic output data, the efficiency of ingot drawing ( $G = 250 \text{ kg/h}$ ) was taken, which corresponds to the basic speed of ingot drawing

$$u_{\text{base}} = \frac{4 \cdot G}{\rho_{T_{\text{out}}} \cdot \pi \cdot d^2} = \frac{4 \cdot 250}{4400 \cdot \pi \cdot 0.4^2 \cdot 3600} =$$

$$= 1.256 \cdot 10^{-4} \text{ m/s (approximately 7.5 mm/min),}$$

the temperature of liquid metal at the inlet into the mould  $T_{\text{in}} = 2061 \text{ K}$  and heating of the ingot is evenly distributed throughout the surface by a thermal flux of

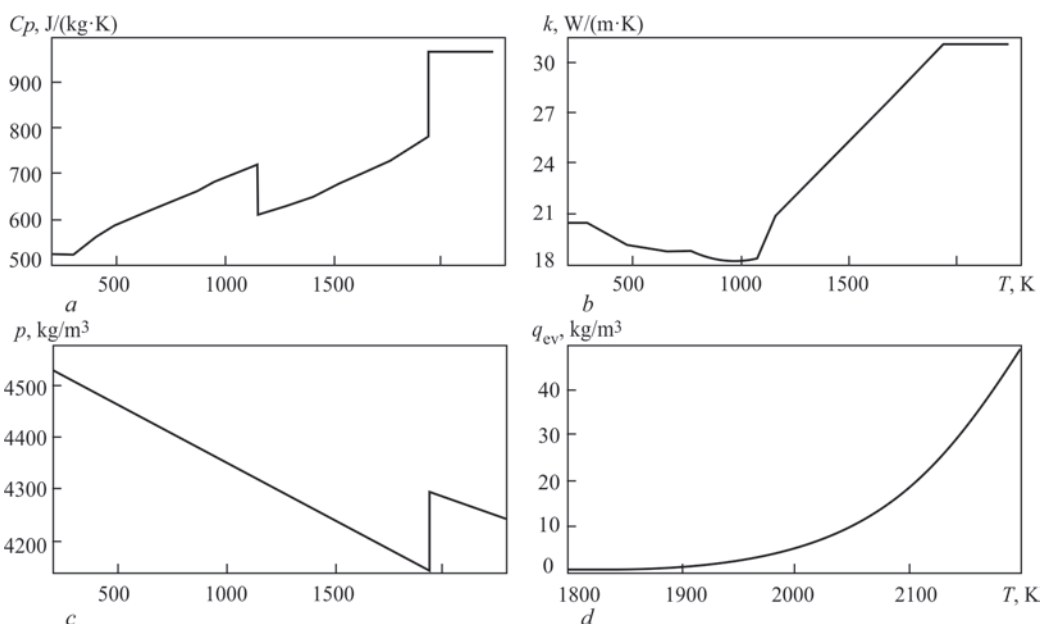


Figure 2. Dependences of specific heat capacity (a), coefficient of thermal conductivity (b), density (c) and evaporation (d) on temperature

a total power  $P_{\text{eb}} = 90$  kW with an efficiency coefficient of electron beam heating being 75 %.

The importance and necessity of taking into account thermogravitation forces in the mathematical model of physical processes in the mould was determined and substantiated by comparing the results of calculations taking into account and without these forces. In order to study the degree of impact of the phenomenon of thermogravitation convection on the thermal state of the ingot and the position of the interphase boundary, the modeling of this process was carried out without taking into account the component  $\rho g$  in the equation (2). The temperature distribution, as well as the isotherms of solidus and liquidus (solid lines) are presented in Figure 3. In this case, the depth of liquid pool is 257 mm. For comparison, in Figure 3 the position of the interphase zone (dashing lines) is shown, obtained taking into account thermogravitation forces.

The results show that not taking into account thermogravitation forces leads to a more than twice increase in the depth of a liquid pool (by 137 mm) and, accordingly, to a change in the nature of the movement of liquid metal. In this case, shifting of the point of the maximum pool depth from the ingot axis is almost absent, despite the asymmetric view of the pool itself.

Therefore, the phenomenon of thermogravitation convection in the specified efficiency of EBM process is a significant factor that determines the thermal state of the ingot, so further calculations were performed, taking it into account.

To determine the exposure of the liquid metal to the overheating temperature, which is fed from the

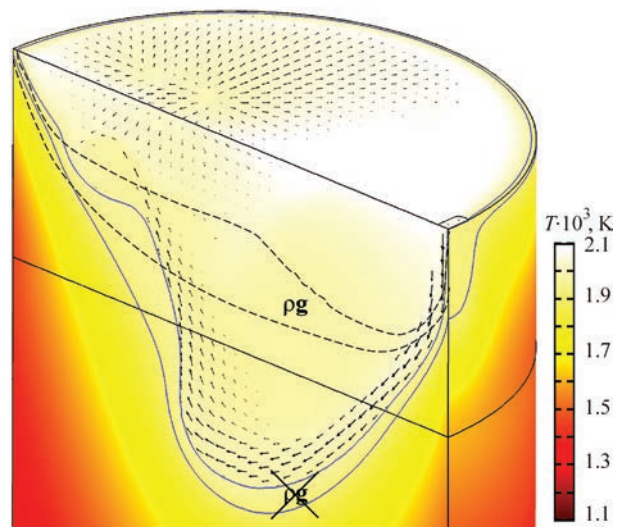


**Figure 3.** Impact of thermogravitation convection phenomenon on interphase zone position

cold hearth, calculations for different temperatures of the liquid metal at the inlet into the mould ( $T_{\text{in}}$ , K: 2041, 2061, 2081, 2101) were performed. As a result, in the studied zone distributions of temperature and speed were obtained, presented in Figures 4 and 5, respectively.

The analysis of distribution of temperatures in the ingot, obtained on the results of modeling showed that under the action of electron beam heating, the surface layer of a melt is heated to the maximum temperature — about 2085 K (Figure 4), which in some cases may even exceed the temperature of the liquid metal, that is fed from the cold hearth with a temperature of 2040–2100 K (Figure 4, *a, b*). Due to the intensive cooling of the liquid metal, the walls of the mould

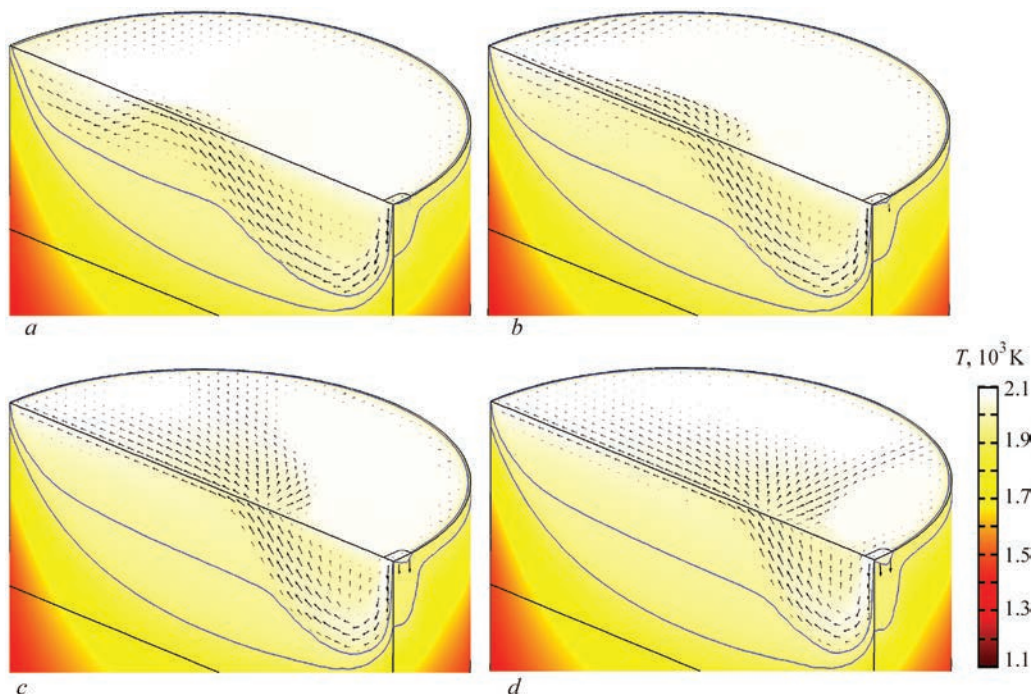


**Figure 4.** Distribution of temperature ( $T_{\text{in}}$ ) in ingot during EBM, K: *a* — 2041; *b* — 2061; *c* — 2081; *d* — 2101

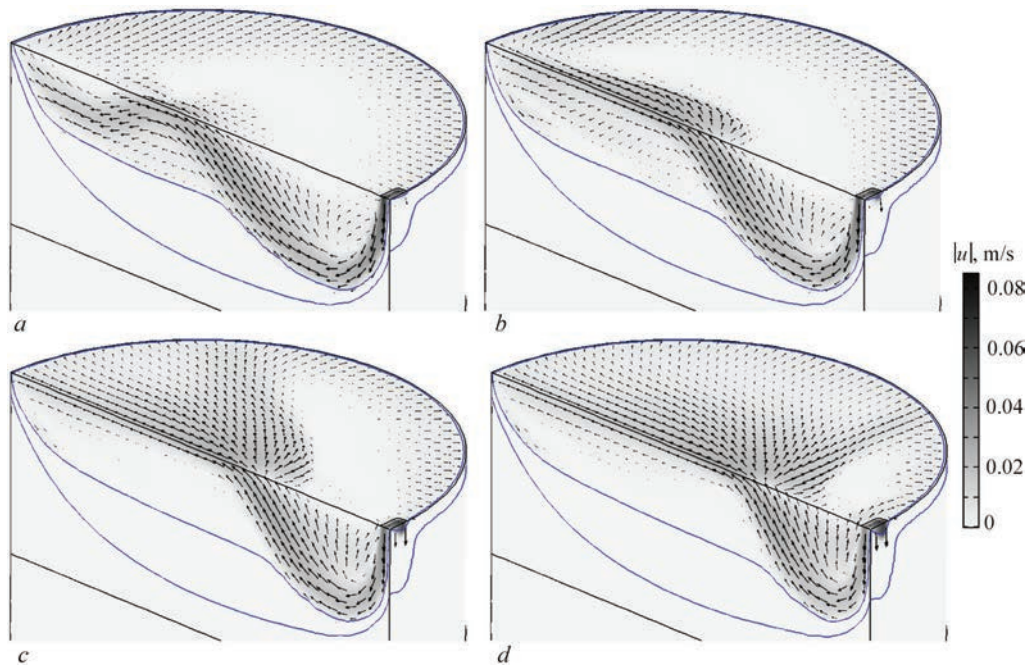


**Figure 5.** Distribution of melting speed ( $T_{in}$ ) in ingot during EBM, depending on temperature, K: *a* — 2041; *b* — 2061; *c* — 2081; *d* — 2101

form the outer surface of the ingot in it, the thickness of the skull between the liquid metal and the wall of the mould in its upper part is 5–7 mm. Along the length of the ingot, the temperature decreases from 2085 K on the surface of a melt to 1000 K on its lower boundary of the calcualtion region. At the output of the ingot from the mould, the temperature of its surface is about 1500 K and weakly depends on the technological parameters of melting.

The analysis of the distribution of the rate of movement of the liquid metal in the mould showed that the flow of a melt from the cold hearth is deepened near the wall of the mould to the maximum depth and then mirrored from the bottom of the pool, gets to its surface and spreads throughout the volume of a melt (Figure 5, *a, b*). It should be noted that in the place of deepening of the inlet flow, the thickness of the two-phase zone is minimal and amounts to 3–6 mm. Under the conditions of a low overheating of a melt getting into the mould from the cold hearth, at the temperature, higher than the melting temperature of titanium, the movement of the liquid metal occupies the entire volume of the pool, where the temperature exceeds the liquidus temperature of titanium. Whereas with an increase in the temperature of the metal flow at the inlet, the melt movement is concentrated only near a free surface, forming quite volumetric stagnation zones (Figure 5, *c, d*). This phenomenon may be predetermined by the action of thermogravitation forces.

In general, the calculations showed that the shape of a liquid pool is asymmetric (Figures 4, 5). Al-

though the crystallization front is approaching the plane one, in the region of the inlet zone of the liquid metal, washing of the solid phase near the wall of the mould is observed (Figure 6). The thickness of the skull in this zone is 2–3 mm, which is 2–3 times smaller than the thickness of the skull in other zones of the mould. During movement of the ingot downwards, such a thin skull can be destroyed and form well-known typical defects of metal tangling on the surface of the ingot.

Shifting of the maximum depth point relative to the ingot axis ( $d_{pool}$ ) and the liquid pool depth ( $h_{pool}$ ) depending on the overheating temperature on the liquid metal at the inlet into the mould are presented in Figure 7. These parameters were determined by the isotherm, which corresponds to the melting temperature of titanium ( $T_m = 1941$  K).

It is interesting that with an increase in the metal temperature at the inlet into the mould (in the test range), shifting of the point of the maximum pool depth from the ingot axis (Figure 7, *a*) decreases. Although it was expected, that with an increase in the overheating temperature of the liquid metal, fed from the cold hearth, the maximum liquid pool depth will be shifted from the ingot axis in the direction of the inlet of a liquid metal jet.

As for the depth of a liquid pool, it almost does not change in the test range of the temperature of the liquid metal at the inlet into the mould (Figure 7, *b*), based on which the conclusion can be made of their weak dependence. However, as can be seen from Figure 4, with an increase in the temperature of the liq-

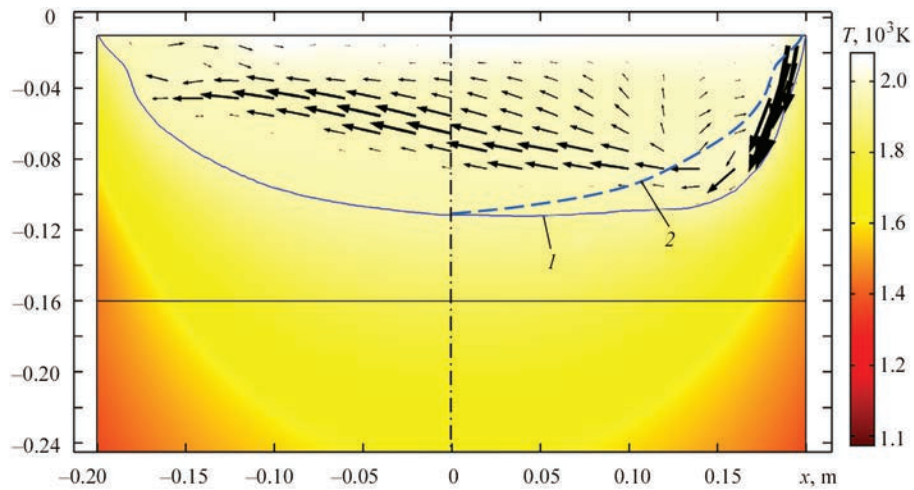


**Figure 6.** Longitudinal section of liquid pool in titanium ingot of 400 mm diameter during EBM; 1 — point of the maximum liquid pool depth; 2 — mirror projection of the left half of isotherm ( $T_m = 1941$  K) relative to the ingot axis for visual evaluation of liquid pool asymmetry

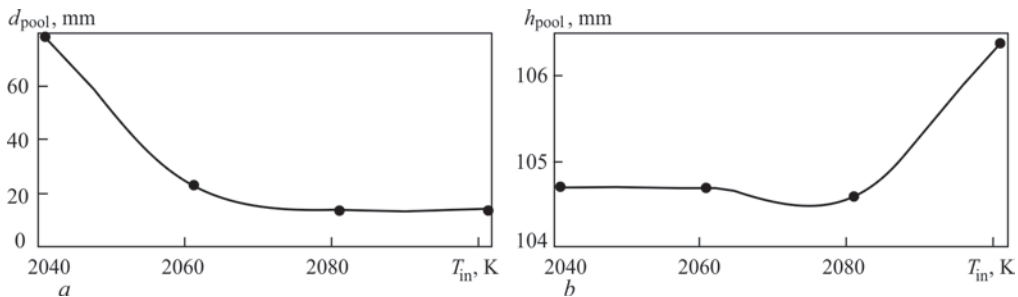


**Figure 7.** Dependences of shifting of the point of maximum depth relative to the ingot axis (a) and liquid pool depth (b) on overheating temperature of liquid metal at the inlet into the mould 8

uid metal at the inlet into the mould, the nature of its movement changes significantly.

While producing ingots by EBM method, one of the important technological parameters is the process efficiency. Therefore, further calculations were aimed at studying the impact of the feed rate of liquid metal from the cold hearth into the mould on the shape and depth of a liquid pool.

While modeling, the overheating temperature of the metal fed into the mould was taken as  $T_{in} = 2061$  K. The position of the isotherms, corresponding to the melting temperature of titanium ( $T_m$ ) for different speeds of ingot drawing in the range of  $u_{cast} - 1.3u_{cast}$  are presented in Figure 8.

As is seen from Figure 8, with an increase in the efficiency of casting, configuration of the crystalli-

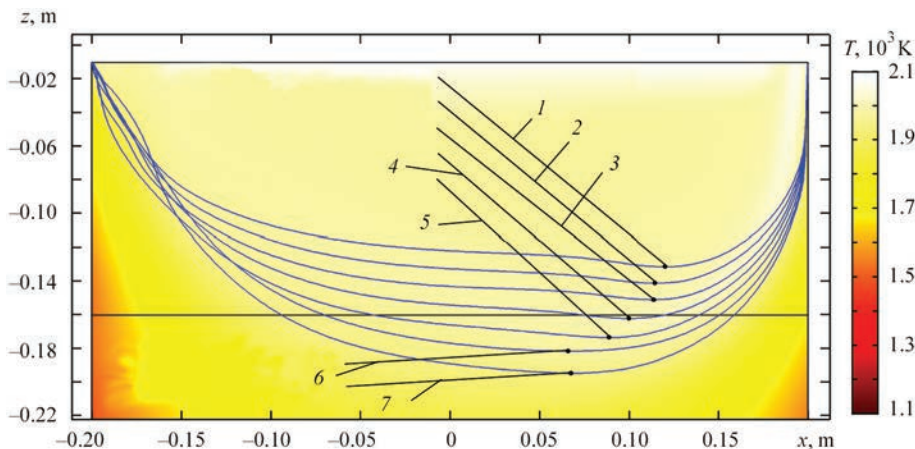


**Figure 8.** Position of isotherms of melting temperature of titanium for different speeds of ingot drawing from the mould (the point marks the place of the maximum liquid pool depth and its parameters are indicated in the format:  $u_{cast}^2; d_{pool}^2; h_{pool}^2$ , m): 1 —  $1.00 u_{cast}^2; 0.120; 0.122$ ; 2 —  $1.05 u_{cast}^2; 0.116; 0.131$ ; 3 —  $1.10 u_{cast}^2; 0.114; 0.141$ ; 4 —  $1.15 u_{cast}^2; 0.100; 0.152$ ; 5 —  $1.20 u_{cast}^2; 0.088; 0.164$ ; 6 —  $1.25 u_{cast}^2; 0.066; 0.172$ ; 7 —  $1.30 u_{cast}^2; 0.068; 0.185$

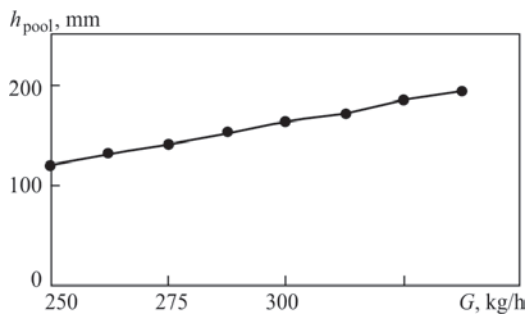


**Figure 9.** Dependence of liquid pool depth on efficiency during EBM of titanium ingot of 400 mm diameter

zation front, despite taking into account thermogravitation forces, is approaching to a cone-shaped one. This indicates that a more plane front of melt crystallization can be provided by reducing the efficiency of ingot casting. It is also clear that with a growth in efficiency, the impact of thermogravitation forces on the thermal state of the ingot will be weakened.

For a more clear demonstration of the results obtained with the help of a mathematical model of the carried out calculations, the dependence of the liquid pool depth on the efficiency of EBM process of titanium ingot was constructed (Figure 9).

As is seen from Figure 9, with an increase in the speed of ingot drawing by 30 %, the liquid pool depth increases by more than 50 % (from 0.122 to 0.185 m).

Analysis of the obtained results showed that a growth in the process efficiency, as in the case of increasing the overheating temperature of the metal getting into the mould, causes shifting of the maximum liquid pool depth point ( $d_{pool}$ ) to the ingot axis. In addition, with a growth in the process efficiency, a significant increase in the liquid pool depth is observed, which is also confirmed by the data of [10].

## Conclusions

1. Applying the methods of mathematical modeling of heat of mass transfer, the features of crystallization and metal pool configuration during EBM of titanium ingots in the mould of 400 mm diameter were established. Three-dimensional fields of speed of liquid metal movement and its temperature were obtained taking into account the action of thermogravitation forces for a laminar nature of melt movement.

2. The necessity of taking into account thermogravitation forces during modeling of hydrodynamic processes in the mould during EBM of titanium ingots was substantiated. It is shown that thermogravitation

is a significant factor in determining the thermal state of the ingot, therefore, its consideration is mandatory. With the growth in EBM efficiency, the contribution of thermogravitation forces to the thermal state of the ingot will be weakened.

3. It was established that the impact of the overheating temperature of the liquid metal fed into the mould from the cold hearth on the configuration and depth of a liquid pool is insignificant. In the studied range of liquid metal temperatures at the inlet into the mould (2041–2101 K) with a change in temperature, the nature of its movement changes only slightly.

4. It was found that the impact of the efficiency of electron beam melting of titanium on the temperature distribution and, accordingly, on the shape and depth of a liquid pool is significant. With an increase in the speed of ingot drawing by 30 %, the depth of a liquid pool increases by 1.5 times (by 63 mm), and the point of the maximum liquid pool depth is approaching the ingot axis.

1. Bellot, J.-P., Flori, E., Ess, E., Ablizer, D. (1996) Mathematical modeling of electron beam melting process with cold hearth and its application for titanium manufacture. *Problemy Spets. Elektrometallurgii*, **4**, 27–37 [in Russian].
2. Paton, B.E., Trigub, N.P., Kozlitsin, D.A. et al. (1997) *Electron beam melting*. Kiev, Naukova Dumka [in Russian].
3. Paton, B.E., Trigub, N.P., Akhonin, S.V., Zhuk, G.V. (2006) *Electron beam melting of titanium*. Kiev, Naukova Dumka [in Russian].
4. Lesnoj, A.B., Demchenko, V.F., Zhadkevich, M.L. (2001) Modeling of hydrodynamics and heat exchange in crystallization of ingots of electron beam remelting. *Problemy Spets. Elektrometallurgii*, **2**, 17–21 [in Russian].
5. Zhuk, G.V., Kalinyuk, A.N., Trigub, N.P. (2002) Modeling of conditions of removal of shrinkage pipe from cylindrical ingots. *Advances in Electrometallurgy*, **1**, 19–21.
6. Zhuk, G.V., Akhonina, L.V., Trigub, N.P. (1998) Mathematical modeling of crystallization processes of Ti–6Al–4V titanium alloy in EBCH. *Problemy Spets. Elektrometallurgii*, **2**, 21–25 [in Russian].
7. Akhonin, S.V., Gorislavets, Yu.M., Glukhenkiy, A.I. et al. (2019) Modeling hydrodynamic and thermal processes in the mould in cold-hearth electron beam melting. *Suchasna Elektrometall.*, **4**, 9–17 [in Russian]. DOI: <https://doi.org/10.15407/sem2019.04.02>
8. Mills, K. (2002) *Recommended values of thermophysical properties for selected commercial alloys*. Woodhead publishing limited.
9. *Physical properties of titanium* [in Russian]. <https://libmetal.ru/titan/phisproptitan.htm>
10. Zhuk, G.V. (2008) On influence of metal heating power distribution in mould in EBCHM process on structure of titanium ingots. *Advances in Electrometallurgy*, **2**, 15–18.

Received 03.02.2021

# EDDY CURRENT MONITORING OF ALUMINIUM ALLOY DEGRADATION DURING LONG-TERM OPERATION OF AIRCRAFT

V.M. Uchanin<sup>1</sup>, O.P. Ostash<sup>1</sup>, S.A. Bychkov<sup>2</sup>, O.I. Semenets<sup>2</sup> and V.Ya. Derecha<sup>2</sup>

<sup>1</sup>G.V. Karpenko Physico-Mechanical Institute of the NAS of Ukraine  
5 Naukova Str., 79060, Lviv, Ukraine. E-mail: vuchanin@gmail.com

<sup>2</sup>Antonov Company

1 Akademika Tupoleva Str., 03062, Kyiv, Ukraine. E-mail: info@antonov.com

Monitoring of aluminium alloy degradation is a very important part in ageing aircraft maintenance strategy. Our approach is based on the possibility of finding correlation between the material parameters measurable using nondestructive methods and cyclic crack growth resistance characteristics of the evaluated material. It was revealed that specific conductivity as a structure-sensitive parameter of aluminium alloys, measured by the eddy current method, can be applied as an effective tool for such evaluation. The main advantage of the eddy current method is the possibility to carry out the measurements without a direct contact with the inspected surface. From the point of view of the eddy current method, an aircraft component can be represented by 3-layer object, which consists of dielectric protective coating, anticorrosive layer of about 0.5 mm thickness of pure aluminium cladding and aluminium alloy skin subjected to operational loading. To measure conductivity in this third layer with a high lift-off suppression (up to 0.5 mm), a new eddy current conductivity measuring device of type VEPR-31 was designed. The correlations between elongation, fatigue limit of degraded D16T and B95T1 alloys for different equivalent stresses were obtained. Eddy current measurements of specific conductivity carried out in AN-12 aircrafts (produced in 1966) in different zones of the wing after a long-term operation in aircraft repair plant condition operation confirmed the efficiency of the proposed methodology. 27 Ref., 8 Figures.

*Key words:* aircraft, aluminium alloys, degradation, eddy current method, conductivity, fatigue crack growth resistance

Nondestructive testing (NDT) of critical structures during operation is mostly performed in order to detect defects of fatigue and corrosion origin [1–3]. At the same time, the problem of timely evaluation of mechanical characteristics of structural materials, changing in the process of degradation changes of the structure under the influence of operational factors, which can include the effect of elevated temperature, static and cyclic loads, corrosive environment, radiation, etc. [4, 5]. The obtained data are necessary for evaluation of structural reliability of and prediction of their service life.

Operational degradation of structural aluminium alloys (AA) is associated with the action of many factors, among which static and cyclic loads, temperature, exposure to aggressive media, etc. have the highest influence [6–9]. The mentioned factors affect the material of structures in different way, which leads to an increase in the amount of dispersed intermetallics and the density of dislocations, diffusion of alloying elements and their segregation along the grain boundaries, microcracking of secondary phase inclusions, etc. [7, 9]. It is particularly important to note

the synergy of operational factors, when each of them separately does not lead to a significant degradation of materials, and their combined action is of crucial importance. Without evaluating the degradation change of mechanical properties of materials it is impossible to reliably evaluate residual life of structures and, in particular, operation of aircraft on the modern principle of admissible damage. Degradation of AA properties can be evaluated by destructive and nondestructive methods [9]. Destructive methods of establishing real life characteristics of materials are based on mechanical tests of witness specimens or specimens cut out from existing structures during the repair and replacement of individual parts of structures. During operation, such an approach is objectively impossible, which stimulates the search for other approaches and makes the need for operational monitoring of degradation changes in the structure of materials by NDT methods relevant.

Our approach is based on the search and use of correlations between physical structure-sensitive parameters of the material, which can be determined by NDT methods and mechanical characteristics of the

V.M. Uchanin — <https://orcid.org/0000-0001-9664-2101>

© V.M. Uchanin, O.P. Ostash, S.A. Bychkov, O.I. Semenets and V.Ya. Derecha, 2021

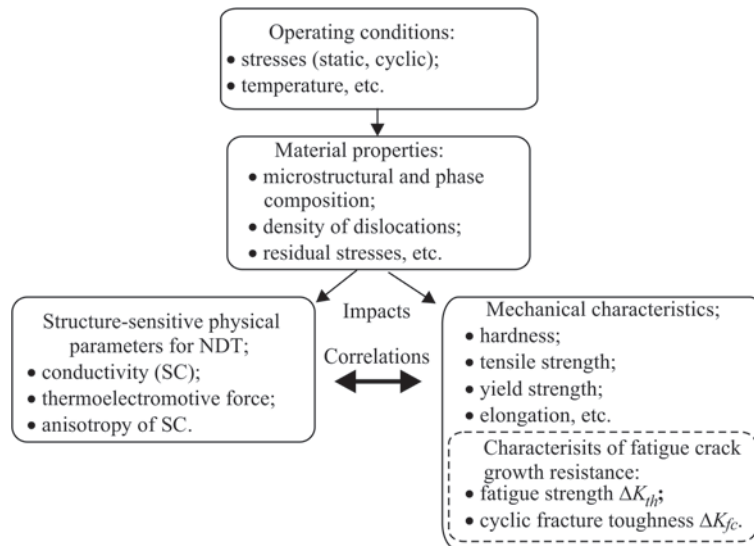


**Figure 1.** Relationships between operating conditions, structure and physical and mechanical characteristics of aluminium alloys

material under static and cyclic loading, which, on the one hand, are sensitive to structural changes and degradation of the material, and on the other are necessary to calculate the residual life of structures [10, 11]. The scheme of relationships that lead to the formation of such correlations for AA is shown in Figure 1.

It is obvious that operating conditions, in particular nature of mechanical stresses, temperature, corrosive environment, affect the change of material properties, including microstructural and phase composition, dislocation density and residual stresses, which can be considered to be the most decisive (Figure 1). In turn, the properties of the material simultaneously affect the structure-sensitive physical parameters of the material, which can be determined by means of NDT, and the mechanical characteristics of the material. A similar approach was used by us to test the degradation changes of ferromagnetic steels of steam conductor heat power plants on the basis of measuring the coercive force of the material [12]. Obviously, this approach requires a combination of modern approaches to fracture mechanics with the development of NDT capabilities.

For AA, the structure-sensitive parameters of NDT can be specific conductivity (SC) and thermoelectromotive force (TEMF) [5, 6, 11]. Our previous studies showed that the choice of SC as a structure-sensitive parameter has significant advantages due to the possibility of its contactless measurement by the eddy current method through a layer of paint-and-lacquer coating [13]. SC anisotropy indicated in Figure 1 can also be a promising direction for development of methods for monitoring AA degradation, provided that the means of its determination are created, which are still at the initial stage [14].

The novelty of our approach consists in the search for correlations between SC and fatigue crack growth

resistance (FCGR) characteristics, which are needed to calculate the residual life of aircraft structures in contrast to previous works [15, 16], which investigated the correlations of SC with such characteristics of AA as hardness, tensile strength, yield strength and elongation. In Figure 1 FCGR is marked in a dotted line.

It should be noted that characteristics of the existing eddy current structurescopes based on SC measurement do not allow determining SC changes during testing of degradation changes in the material of aircraft structures because of the limited range of tuning out from changes in the thickness of protective dielectric coatings (DC) and a gap, as well as a low depth of testing [15, 18]. The known foreign devices, in particular Sigmatest and Sigmachek, have an insufficient locality of testing due to a large (more than 7 mm) diameter of the working platform of the eddy current converter (ECC) and are used mainly at metallurgical enterprises for quality testing of heat treatment. Therefore, it is necessary to optimize the parameters of eddy current control and develop a new eddy current structurescope with a local ECC and improved metrological characteristics in terms of testing depth and tuning out range from DC thickness and a gap.

**Development of means for contactless measurement of specific conductivity of aluminium alloys in the conditions of aircraft operation.** To provide NDT of aircraft structures during operation, the eddy current structurescope should meet the following general requirements:

- provide a high locality of testing aircraft structures, characterized by the curvature of the surface with a large number of rivet holes;
- provide testing through the protective DC layer without its removal;

- provide testing of changes of the structure in the inner layers of structural material.

The first requirement can be solved by choosing the working diameter of ECC, which should not exceed 1.2 mm. The second requirement to structurescopes requires realization of the methods that can expand the range of tuning out from the effects of changes in the gap between the working surface of ECC and the surface of the testing object (TO) or DC thickness in the range of up to 0.5 mm. We should note that at the used operating frequencies, the gap (air gap) between ECC and TO surface and the DC layer of the corresponding thickness affect the ECC signal equally. Therefore, we will further use the term «tuning out from the gap», meaning also tuning out from the change in the thickness of the protective DC.

To perform the third requirement, it is necessary to reduce the working testing frequency in such a way that output ECC signal was influenced by SC changes in the lower layers of TO.

In terms of the eddy current method, each element of the surface of the aircraft structure can be presented in the form of a three-layer structure (Figure 2) [19]. The upper layer represents a protective DC. The second layer is an anticorrosion cladded layer of pure aluminium. And the third layer is the base aluminium material that bears operating loads and structural degradation changes of the material, which should be tested with tuning out from variable parameters that may affect the testing results.

It is obvious that the problem specified in the complete statement is quite complex and therefore for its solution it is rational to apply methods of mathematical modeling along with experimental means. In particular, in [19] the optimal choice of the operating testing frequency depending on the thickness of DC was analyzed. The dependence of sensitivity of the eddy current method to the change of SC on the operating testing frequency for different values of the gap (DC thickness) was investigated. The existence of an optimal operating frequency depending on DC thickness is shown, which drops with an increase in DC thickness. To obtain the maximum sensitivity to SC change during testing through the DC layer of 0.5 mm thickness, the optimal frequency should be 30 kHz, which is three times lower than the operating frequencies of previously developed devices for measuring SC in AA.

To reduce the SC measurement error associated with a possible change in the gap (or DC thickness), it is promising to use the phase method for ECC signal processing [20]. The phase structurescope (SC measuring device) consists of two channels: a measuring and a reference one. To increase the range of tuning

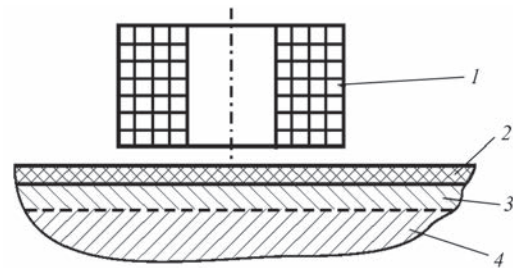


**Figure 2.** ECC over the element of aircraft structure in the form of a 3-layer electric conductive TO: 1 — ECC; 2 — DC; 3 — cladding layer of aluminium; 4 — aluminium alloy

out from the impact of changes in the gap, the output ECC signal is summed up with a compensation signal, which actually leads to a displacement of the reference point in the complex plane of the signal. We used the method of dynamic compensation, when the compensation signal changes only on one component depending on the SC value, which simplifies the realization of the phase method and expands the range of tuning out from the change in the gap [21]. In the reference channel from the signal of the generator, a reference signal for the operation of the phase detector is formed. In order to set a zero signal at the output of the phase detector when setting ECC on the specimen with SC, which corresponds to the lower values of the measured range, the phase shifter of a reference channel was introduced in the circuit. The characteristics of the phase detector have a key importance to achieving a high accuracy of the SC measuring device as a whole and its development requires a special attention. In the device an updated circuit is used, that reduces the errors associated with the conversion of the signal phase into a time interval, which is used as an indication parameter [22]. At the output of the phase detector a signal is extracted, proportional to the phase shift between the measuring and reference signals. For digital indication of the measured value directly in SC units (MSm/m), into the SC measuring circuit, a scaling and linearization unit was introduced according to our invention [23]. Figure 3 shows the dependences of the signal at the output of the phase detector from the gap, which were obtained without tuning out from it and with realization of the proposed method of eddy current testing with tuning out from the impact of the gap [21]. The results are given for the beginning, middle and end of the SC measurement range (14.0; 24.7 and 37.1 MSm/m, respectively). These dependences show that the signal at the output of the phase detector does not depend on the size of the gap in the range of up to 0.5 mm, which provides the possibility of testing through the DC layer of appropriate thickness.

The set of technical solutions presented above is used to create an eddy current structurescope-SC

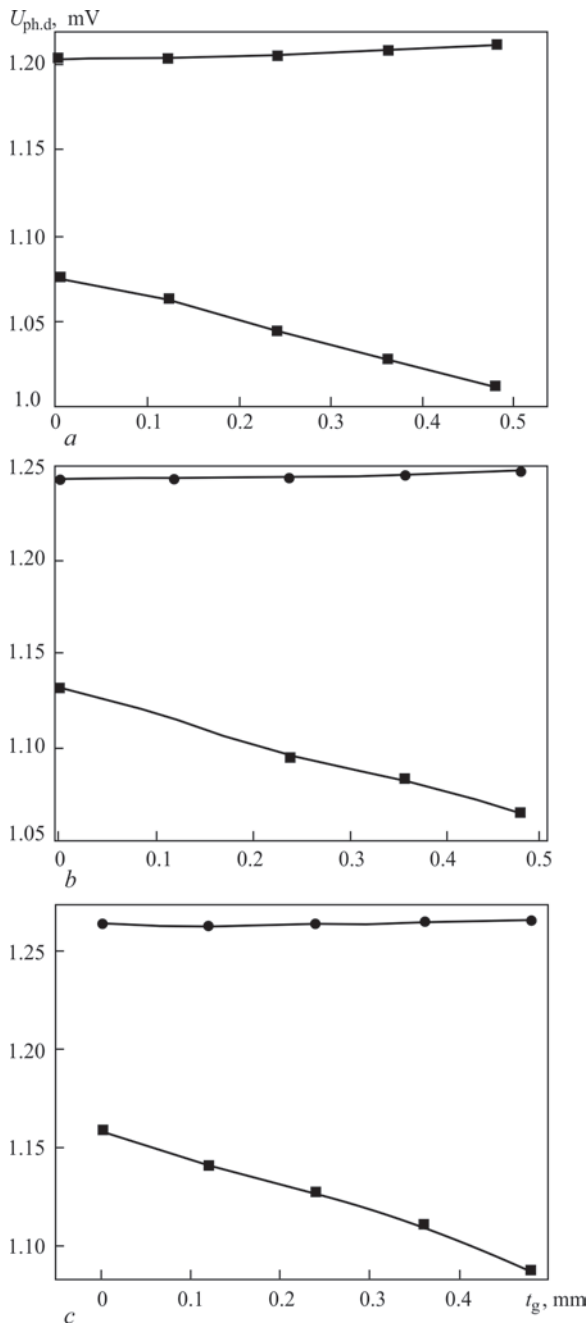


**Figure 3.** Dependence of stress at the output of phase detector  $U_{\text{phD}}$  on the gap  $t_g$  without tuning out (●) and with tuning out (■) for ECC mounted on the specimens of the material with SC of 14.0 MSm/m (a), 24.7 (b) and 37.1 (c)

meter (Figure 4), which solves the problem of local measurement of the specific SC of aluminium alloys in the range of 14.0–37 MSm/m with an error of up to 2 % with tuning out from the impact of change of a gap to 0.5 mm.

The eddy current structurescope of type VEPR-31 (Figure 4), unlike previously created devices of type VEP-21 and VEP-22 [6, 9], has a larger range of tuning out from the value (change) of the gap or thickness of paint and varnish coating and an autonomous power supply. In addition, in the device a reduced operating frequency of 60 kHz was used,



**Figure 4.** Eddy current structurescope of type VEPR-31

which allows testing the change in the structure of AA through the DC layer and cladding. We should note that during the final choice of operating frequency, it is also necessary to have a sufficient sensitivity of measuring the phase of the output signal of ECC, which drops with a decrease in the operating frequency. The device uses a local ECC, the windings of which are mounted on a ferrite core with a diameter of 1.1 mm, which allows testing aircraft structures with a large number of holes.

**Basic technical characteristics of the structurescope of type VEPR-31**

- SC measurement range, MSm/m ..... 14.0–37.1
- Main measurement error in normal conditions, % ..... not more than  $\pm 2$
- Admissible gap between ECC and testing surface, mm ..... not more than 0.5
- Device power supply:
  - from the mains of 50–60 Hz, voltage 220 V
  - from a built-in battery
- Power consumption, W ..... not more than 1.0
- Overall dimensions, mm ..... not more than 60×160×14
- Mass of device, kg ..... not more than 1.5

Metrological and operational characteristics of the structurescope of type VEPR-31 allow monitoring degradation changes of AA structure under operating conditions, which is confirmed by the experience of its use at the SE «Antonov».

**Correlation dependencies between mechanical characteristics and SC of degraded aluminium alloys.** It is shown [24] that the processes of degradation of AA depend on the load of structural elements and are displayed in the change of SC value. It was found that a compatible long-term effect of mechanical stresses and elevated temperatures causes changes in the fine structure, significant local inner stresses and determines the special mechanical behavior of structural AA of type D16 and B95. At the same time, their tendency to brittle fracture grows (plasticity  $\Delta$  drops) and FCGR ( $\Delta K_{th}$ ,  $\Delta K_{fc}$ ) decrease, which determine fatigue life ( $N_f$ ) of structural elements [9], and SC  $\sigma$

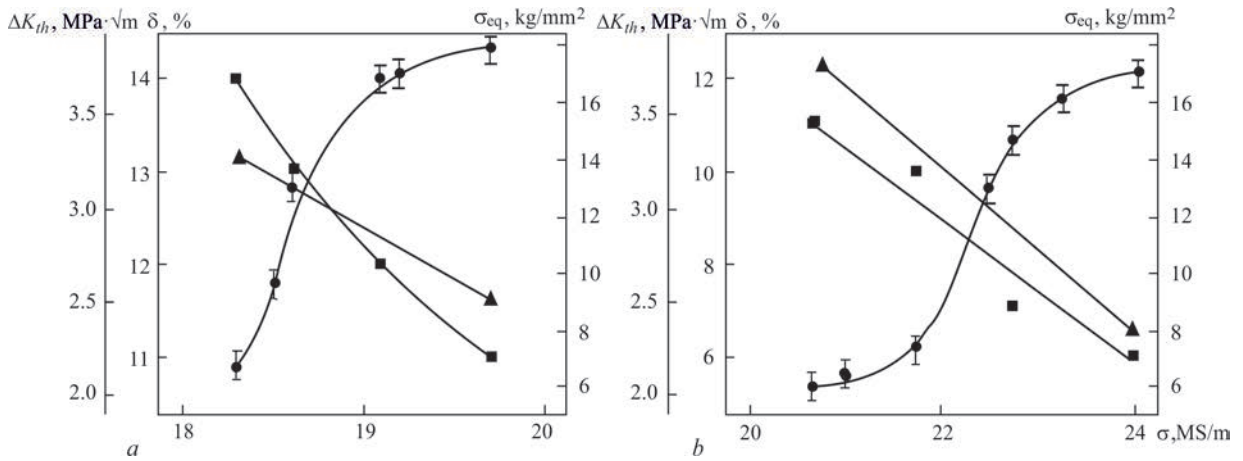


**Figure 5.** Dependencies between elongation  $\delta$  (■), fatigue threshold  $\Delta K_{th}$  (▲), level of operating equivalent stresses  $\sigma_{eq}$  (●) and SC ( $\sigma$ ) of degraded D16ATNV (a) and B95T1 (b) alloys

increases. It was found that to a 1.5–2 times drop of fatigue threshold  $\Delta K_{th}$  and fatigue strength  $N_f$  of the specimens of degraded alloys of type D16 and B95, a 20–30 % growth of SC  $\sigma$  (3–4 MSm/m with a measurement error of 2 %) corresponds [10].

The results of investigations on the specimens cut out from the skin zones with different operating equivalent stresses showed that based on SC values, the change in mechanical properties of the material, the degree of its degradation can be evaluated, comparing them with the data obtained by destruction methods (Figure 5). It is obvious that an increase in SC values indicates the degradation of the material in the local areas of the skin, which is manifested in depletion of ductility in the material (reduction of its elongation) and a drop of resistance to fatigue crack propagation (fatigue threshold).

The obtained results create a basis for monitoring the degradation of structural aluminium alloys during long-term operation [25–27]. It is important that realization of these approaches by means of eddy current structuroscopy allows carrying out measurement of SC of materials of aircraft structures without removal of lacquer coatings.

**Monitoring of degradation of aluminium alloys during long-term operation of aircraft.** The developed approaches were tested during the measurement of SC distribution in different zones of the upper (B95T1 alloy) and lower (D16ATNV alloy) wing skin of AN-12 aircraft, which has been in operation since 1966 [10, 11]. Measurements were carried out using the eddy current structurescope of type VEPR-31 (Figure 4). The distribution of SC values ( $\sigma$ ) of the material of the upper and lower wing skin of AN-12 aircraft in the area between the 4 and 5 stringer along the wing from the root of the wing to its end by the numbers of ribs is shown in Figure 6. The values of  $\sigma_k$  (▲) on the end element of the wing are also indi-

cated. The values of SC gradually drop from the wing root with an increase in the number of a rib, which is associated with a decrease in the level of equivalent stresses [9, 10]. It is seen that SC on the end element of the wing has the lowest value, which is easily explained by the absence of loads in this area required for degradation process. AA in this zone can be conditionally considered to be one that has not undergone degradation. This allows using the value of SC in the end zones in the cases when information about SC of the material in the state of delivery is absent, which is typical for aircrafts of a long-term operation. Therefore, the value  $\sigma_k$  on the end element of the wing is proposed to be used as a comparative value to determine the level of degradation of the material [27].

As a criterion of local degradation of the material, it is proposed to use three different parameters, which is confirmed by their distribution by the numbers of

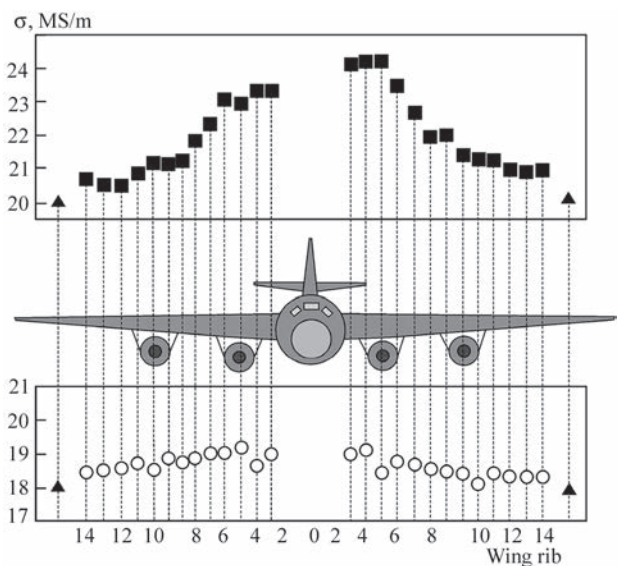


**Figure 6.** Distribution of SC ( $\sigma$ ) of the upper (■) and lower (○) skin of the wing of AN-12 aircraft after many years of operation along the wing by the number of ribs (▲ is the value of SC  $\sigma_k$  on the end element of the wing)

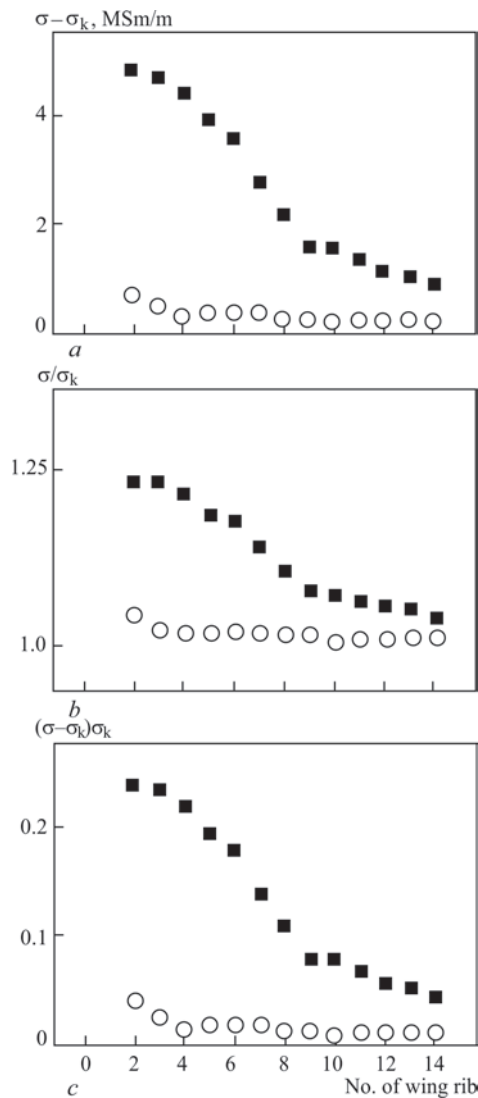


**Figure 7.** Distribution of parameters of local degradation of AA on the upper (■) and lower (○) skins of the wing depending on the number of a rib: *a* — for the parameter  $\sigma - \sigma_k$ ; *b* — for the parameter  $\sigma/\sigma_k$ ; *c* — for the parameter  $(\sigma - \sigma_k)/\sigma_k$

ribs in Figure 7 [27]. The difference  $\sigma - \sigma_k$  between SC of the material in the tested zone and SC of the material of the end element of the wing, respectively, can be used (Figure 7, *a*). The value of this parameter for the nondegraded material corresponds to  $\sigma - \sigma_k = 0$ . Also the ratio  $\sigma/\sigma_k$  (Figure 7, *b*) can be used, which for nondegraded material will correspond to  $\sigma/\sigma_k = 1$ . The ratio  $(\sigma - \sigma_k)/\sigma_k$  can also be used, which for nondegraded material will correspond to  $(\sigma - \sigma_k)/\sigma_k = 0$  (Figure 7, *c*).

The proposed methodology was used to test the technical condition (including the degree of degradation of the material) of aluminium longerons of helicopter blades. Investigation of blades after different operation time (till 1100 h) in assembled and disassembled states was carried out at the JSC «Motor-Sich». SC measurements performed on «open» longerons revealed critical places of damage in the longerons, which correspond to the areas of the maximum operating load.

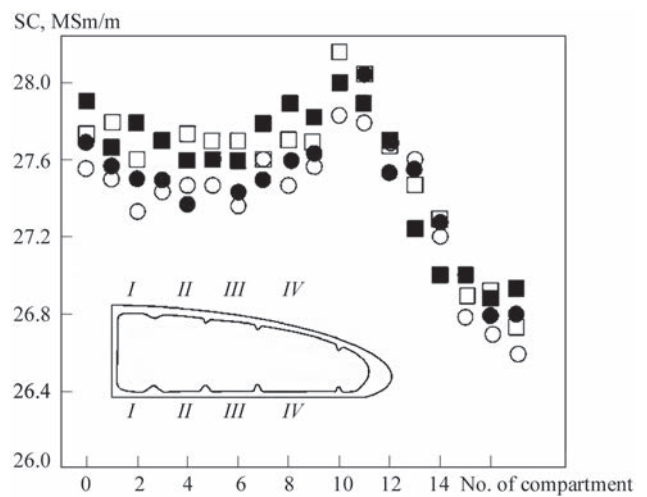


**Figure 8.** SC distribution on the upper (□ and ○) and lower (■ and ●) sides of the helicopter blade longeron in the zones I (□ and ■) and II (○ and ●)

Figure 8 shows, that SC has a maximum value near the root of the blade, and a minimum one at its end, similarly to the distribution of SC along the wing of the aircraft in Figure 6. In the zone of compartments Nos 10, 11 the area of growing SC is observed, which corresponds to the zone of maximum action of tensile, bending and torsional stresses. Thus, according to SC distribution, it is possible to find critical zones of a maximum damage of the helicopter blade longerons.

The presented methodology for evaluation of the level of local degradation of aircraft structures during long-term operation will increase the reliability of prediction of their residual life, and may also become an important component in realizing the concept of safe damage.

### Conclusions

1. The problem of degradation of aluminium alloys during a long-term operation of aircraft is considered. The significance of correlation dependencies between the physical structure-sensitive parameters of the material (which can be determined by NDT methods), and mechanical characteristics of the material during cyclic loading are shown.

2. Peculiarities of monitoring aircraft alloy degradation based on contactless measurement of specific conductivity are analyzed. The eddy current structure-scope for measuring specific conductivity is presented to test damage of materials of aircraft in the operation conditions.

3. It is shown that an increase in the values of specific conductivity indicates degradation of the material in the local areas of the structure, which is manifested in depletion of ductility of the material (reduction of its elongation) and drop in resistance to fatigue crack propagation (fatigue threshold).

4. The methodology of eddy current monitoring of degradation of aircraft aluminium alloys in the conditions of a long-term operation of aircraft structures is offered. The results of effective use of the developed methods and means for determination of critical zones in skins of aircraft and longerons of helicopter blades of aluminium alloys are given.

1. McMaster, R.C., McIntire, P. (1986) *Nondestructive Testing Handbook. Vol. 4: Electromagnetic testing (Eddy current, flux leakage and microwave nondestructive testing)*. USA, American Society for NDT.
2. Dorofeev, A.L., Kazamanov, Yu.G. (1980) *Electromagnetic testing*. Moscow, Mashinostroenie [in Russian].
3. Uchanin, V.M. (2006) Eddy current testing of structure elements. *Fiz.-Khim. Mekhanika Materialiv*, **4**, 66–73 [in Ukrainian].
4. Dobmann, G., Boller, Ch., Herrmann, H.-G. Altpeter, I. (2014) Micromagnetic and electromagnetic NDT for lifetime management by monitoring ageing of structural materials. *Int. J. Microstructure and Materials Properties*, **9(3–5)**, 348–359.
5. Estorff, U., Davies, L., Trampus, P. Eds. (1999) In: *Proc. of the Joint EC-IAEA Meeting on NDT Methods for Monitoring Degradation*. Petten, European Commission, JRC Institute of Advanced Materials.
6. Ostash, O.P., Fedirko, V.M., Uchanin, V.M. et al. (2007) *Fracture mechanics and strength of materials*. Vol. 9: Strength and fatigue life of aircraft materials and structure elements. Lviv, Spolom [in Ukrainian].
7. Ostash, O.P., Andrejko, I.M., Golovatyuk, Yu.V. (2006) Degradation of materials and fatigue strength of aircraft structures in long-term operation. *Fiz.-Khim. Mekhanika Materialiv*, **4**, 5–16 [in Ukrainian].
8. Nesterenko, G.I., Basov, V.N., Nesterenko, B.G., Petrusenko, V.G. (2006) Influence of long-term service of aircraft on properties of materials of their structures. *Problemy Mashinostroeniya i Nadyozhnost Mashin*, **4**, 41–50 [in Russian].
9. Ostash, O.P., Kiva, D.S., Uchanin, V.M. et al. (2012) Diagnostics of technical condition of aircraft structures after long-term operation. *Tekh. Diagnost. i Nerazrush. Kontrol*, **2**, 15–22 [in Russian].
10. Ostash, O., Uchanin, V., Semenets, O., Holovatyuk, Y., Kovachuk, L., Derecha, V. (2018) Evaluation of aluminium alloys degradation in aging aircraft. *Reseach in Nondestructive Evaluation*, **29(3)**, 156–166. <http://dx.doi.org/10.1080/09349847.2017.1302622>.
11. Uchanin, V., Ostash, O. (2019) Development of electromagnetic NDT methods for structural integrity assessment. *Procedia Structural Integrity*, **16**, 192–197.
12. Uchanin, V., Ostash, O., Nardoni, G., Solomakha, R. (2020) Coercive force measurements for structural health monitoring. In: *The Fundamentals of Structural Integrity and Failure*. Ed. by Richard M. Wilcox. New York, Nova Science Publishers.
13. Uchanin, V.M., Ostash, O.P. (2019) Evaluation of operational degradation of structural materials by electromagnetic methods of nondestructive testing. In: *Proc. of 9<sup>th</sup> Nat. Sci.-Techn. Conf. on Nondestructive Testing and Technical Diagnostics (Kyiv, 21.11.2019)*, 35–40 [in Ukrainian].
14. Uchanin, V.M., Rybachuk, V.G., Kulynych, Ya.P. *Eddy current method for measurement of parameters of electrical conductivity anisotropy of nonferromagnetic materials*. Pat. 138680, Ukraine, Int. Cl. G01 N27/90. Publ. 10.12.2019
15. Dorofeev, A.L., Ershov, P.E. (1985) *Physical fundamentals of electromagnetic structuroscopy*. Novosibirsk, Nauka [in Russian].
16. Naumov, N.M., Miklyaev, P.G. (1974) *Resistometric nondestructive testing of aluminium wrought alloys*. Moscow, Metallurgiya [in Russian].
17. Rummel, W.D. (1966) Characterization and evaluation of 2014 aluminium alloy by eddy current conductivity techniques. *Materials Evaluation*, **14(6)**, 322–326.
18. Bakunov, A.S. (2004) Evolution of equipment for eddy current structuroscopy of nonferrous metals in Russia. *Kontrol. Diagnostika*, **4**, 63–64 [in Russian].
19. Nazarchuk, Z.T., Uchanin, V.M., Kulynych, Ya.P. (2019) Optimization of eddy current testing parameters of degradation changes in specific conductivity of aluminium alloys of aging aircraft. *Vidbir i Obrobka Informatsii*, **47**, 5–11 [in Ukrainian]. doi.org/10.15407/vidbir2019.47.005
20. Uchanin, V.N., Makarov, G.N. (1996) Suppression of influence of gap in contactless measurement of specific conductivity by eddy current method. *Tekh. Diagnost. i Nerazrush. Kontrol*, **4**, 41–45 [in Russian].
21. Uchanin, V.M. (2012) *Method for measurement of electrical conductivity of nonmagnetic materials*. Pat. 98206, Ukraine. Publ. 25.04.2012 [in Ukrainian].
22. Uchanin, V.M., Cherlenskyi, V.V. (2011) *Device for eddy current testing of parameters of products*. Pat. 58670, Ukraine. Publ. 26.04.2011 [in Ukrainian].
23. Uchanin, V.M., Makarov, G.M., Cherlenskyi, V.V. (2012) *Eddy current specific conductivity meter of nonferromagnetic materials*. Pat. 97304, Ukraine. Publ. 10.01.2012 [in Ukrainian].
24. Ostash, O.P., Andrejko, I.M., Markashova, L.I. et al. (2013) Influence of long-term operation on structure and physico-mechanical properties of aluminium alloys of D16 and B95 type. *Fiz.-Khim. Mekhanika Materialiv*, **49(1)**, 18–27 [in Ukrainian].
25. Ostash, O.P., Uchanin, V.M., Andrejko, I.M., Golovatyuk, Yu.V. (2013) *Eddy current method for determination of operation degradation degree of structural materials*. Pat. 101424, Int. Cl. G01N27/90. Publ. 25.03.2013 [in Ukrainian].
26. Ostash, O.P., Uchanin, V.M., Andrejko, I.M. et al. *Eddy current method of determination of local degradation degree of structural materials during long-term operation*. Pat. 106168, Ukraine, Int. Cl. G01N27/90. Publ. 12.05.2014 [in Ukrainian].
27. Ostash, O.P., Uchanin, V.M., Semenets, O.I. et al. (2017) *Method of monitoring of local degradation degree of materials of aircraft structures in long-term operation*. Pat. 113736, Ukraine, Int. Cl. G01N27/90. Publ. 10.02.2017 [in Ukrainian].

Received 22.01.2021

**SEPTEMBER 30, 1964** American engineer Gaspar Kazlauskas, a staff member of North American Aviation Company got a task to develop a welding apparatus for pipe welding. As a result he patented his own invention — orbital welding head. Application of this device is related with wide use of tubular structures in modern industry.



# SUBSCRIPTION-2021



«The Paton Welding Journal» is Published Monthly Since 2000 in English, ISSN 0957-798X, doi.org/10.37434/tpwj.

«The Paton Welding Journal» can be also subscribed worldwide from catalogues subscription agency EBSCO.

If You are interested in making subscription directly via Editorial Board, fill, please, the coupon and send application by Fax or E-mail.

12 issues per year, back issues available.

\$384, subscriptions for the printed (hard copy) version, air postage and packaging included.

\$312, subscriptions for the electronic version (sending issues of Journal in pdf format or providing access to IP addresses).

Institutions with current subscriptions on printed version can purchase online access to the electronic versions of any back issues that they have not subscribed to. Issues of the Journal (more than two years old) are available at a substantially reduced price.

<b>SUBSCRIPTION COUPON</b>			
Address for journal delivery _____			
Term of subscription since	_____ 20	till	_____ 20
Name, initials	_____		
Affiliation	_____		
Position	_____		
Tel., Fax, E-mail	_____		

The archives for 2009–2019 are free of charge on [www://patonpublishinghouse.com/eng/journals/tpwj](http://www://patonpublishinghouse.com/eng/journals/tpwj)



## ADVERTISING

### in «The Paton Welding Journal»

#### External cover, fully-colored:

- First page of cover (200×200 mm) — \$700
- Second page of cover (200×290 mm) — \$550
- Third page of cover (200×290 mm) — \$500
- Fourth page of cover (200×290 mm) — \$600

#### Internal cover, fully-colored:

- First/second/third/fourth page (200×290 mm) — \$400

#### Internal insert:

- (200×290 mm) — \$340
- (400×290 mm) — \$500

- Article in the form of advertising is 50 % of the cost of advertising area
- When the sum of advertising contracts exceeds \$1001, a flexible system of discounts is envisaged
- Size of Journal after cutting is 200×290 mm

#### Address

11 Kazymyr Malevych Str. (former Bozhenko Str.), 03150, Kyiv, Ukraine

Tel.: (38044) 200 82 77

Fax: (38044) 200 82 77

E-mail: [journal@paton.kiev.ua](mailto:journal@paton.kiev.ua)

[www://patonpublishinghouse.com/eng/journals/tpwj](http://www://patonpublishinghouse.com/eng/journals/tpwj)